Neutrino astronomy with KM3NeT/ARCA

van Eeden, T.J.

Publication date
2024
Document Version
Final published version

THIJS JUAN VAN EEDEN

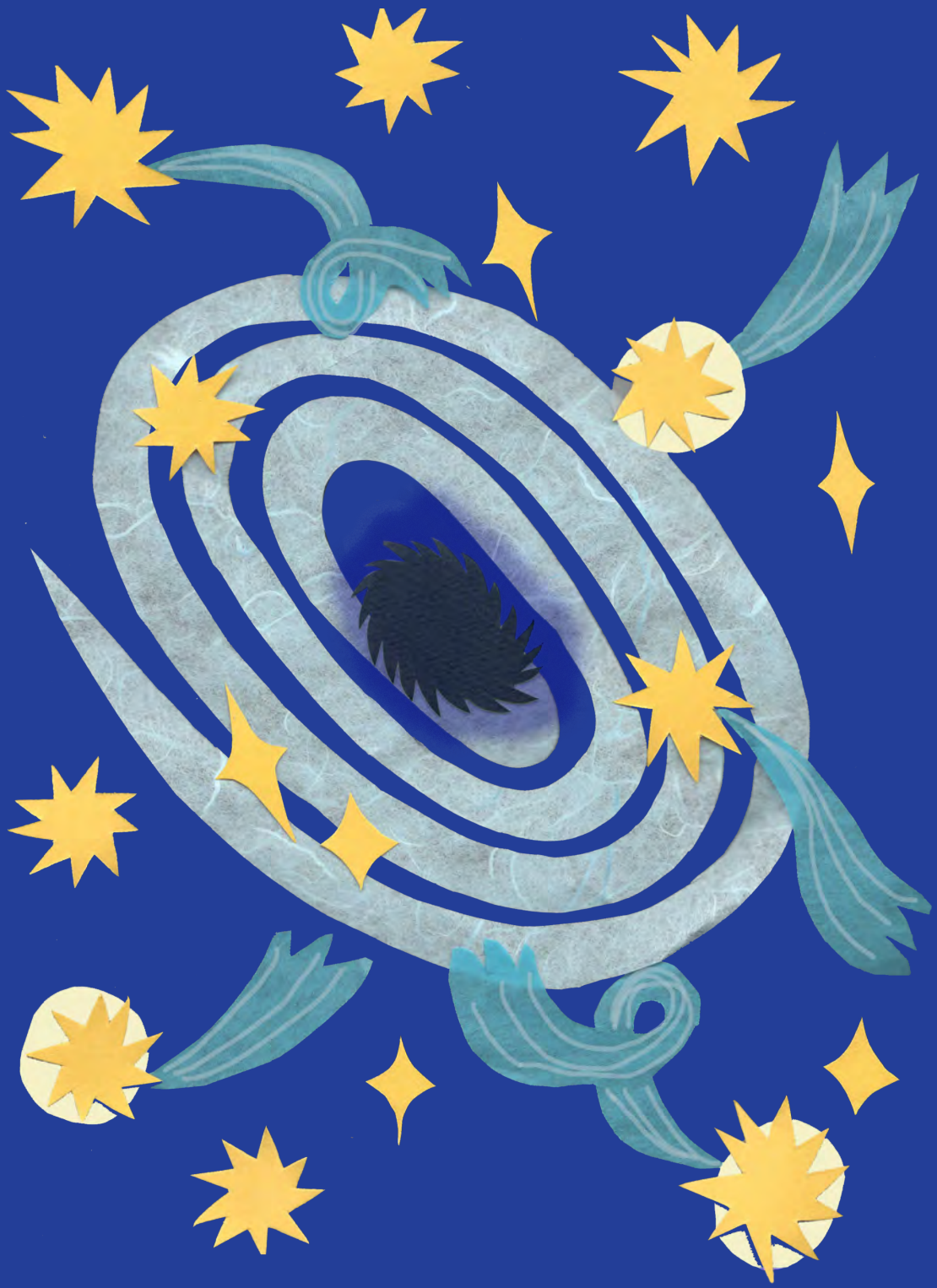

NEUTRINO ASTRONOMY with KM3NeT/ARCA

Neutrino astronomy with KM3NeT/ARCA

Thijs Juan van Eeden

The wonderful cover was designed by Pien Kars.

The research for and publication of this doctoral thesis received financial assistance from NWO through the NWO-VICI grant 680-47-627. The research was carried out at Nikhef in Amsterdam, The Netherlands, and was done in cooperation with the KM3NeT Collaboration.

ISBN 978-94-6510-197-2

thijsvaneeden@gmail.com

Neutrino astronomy with KM3NeT/ARCA

ACADEMISCH PROEFSCHRIFT

ter verkrijging van de graad van doctor
aan de Universiteit van Amsterdam
op gezag van de Rector Magnificus
prof. dr. ir. P.P.C.C. Verbeek
ten overstaan van een door het College voor Promoties ingestelde commissie,
in het openbaar te verdedigen in de Aula der Universiteit
op vrijdag 11 oktober 2024, te 14.00 uur

door Thijs Juan van Eeden
geboren te Amsterdam

Promotiecommissie

Promotores:	prof. dr. ir. P.J. de Jong	Universiteit van Amsterdam
	prof. dr. A.J. Heijboer	NWO-I Nikhef
Overige leden:	prof. dr. C. Finley	Stockholm University
	dr. M.C. Bouwhuis	NWO-I Nikhef
	prof. dr. J. Rojo	Vrije Universiteit Amsterdam
	prof. dr. A.P. Colijn	Universiteit van Amsterdam
	dr. S. Ando	Universiteit van Amsterdam
	dr. C.J.M. Nellist	Universiteit van Amsterdam

Faculteit der Natuurwetenschappen, Wiskunde en Informatica

Contents

Introduction

In the beginning of the twentieth century, scientists were debating the origin of ionisation in the air [1]. They used electroscopes to measure the charge of an object, but these devices would spontaneously discharge even after careful insulation. The dominant hypothesis explained the ionisation through radioactive decays in the crust of the Earth. This was until Victor Hess performed a series of balloon flights in 1912. Hess measured the ionisation as a function of altitude using an insulated electroscope. The measurement of the spontaneous discharge of the electroscope showed a significant increase of radiation for increasing heights, excluding a terrestrial origin. This phenomenon was named cosmic rays, and after a century it still continues to be a rich area of study for physicists.

Figure 1: Victor Hess departing on one of his balloon flights. Adapted from [2].

The main questions regarding cosmic rays are still not answered. Where do they come from and how are these particles accelerated? This has been complicated by several factors that are explained in Chapter 1. These mysteries could be resolved through the detection of astrophysical neutrinos. Neutrinos are elementary particles that are described by the Standard Model of particle physics [3]. Neutrinos are chargeless particles with an infamously small interaction cross section with matter. It is believed that they are produced in the vicinity of cosmic ray accelerators through interactions of protons with matter and radiation. They travel through our universe in straight lines and they can escape dense

regions. This makes them ideal messengers from distant astrophysical objects. The small interaction cross section has a downside as well. It complicates the detection and requires very large detectors in order to obtain statistically significant neutrino datasets.

This thesis is centered on neutrino astronomy using the KM3NeT/ARCA detector, which is a very large neutrino observatory that is currently under construction. The detector operates in water and Chapter 2 discusses the detection of neutrinos in this medium. The primary purpose of KM3NeT/ARCA is to detect neutrinos with energies beyond a TeV with the aim of doing neutrino astronomy. A description of the KM3NeT detector is presented in Chapter 3, followed by an overview of the event simulation and reconstruction procedures in Chapter 4.

The work of the author includes neutrino astronomy prospects using simulated data of the complete detector in Chapter 5, alongside results using recently collected data in Chapter 6. Chapter 7 provides the description of a new reconstruction algorithm tailored to the least studied particle of the standard model: the tau neutrino. This novel reconstruction procedure, in conjunction with existing algorithms, is used in Chapter 8 to estimate the capability of KM3NeT/ARCA to determine the flavour ratio of astrophysical neutrinos.

Chapter 1

Neutrino astronomy

The field of neutrino astronomy utilises neutrinos as messengers to learn about astrophysical processes. Neutrino astronomy seamlessly integrates into the emerging field of multi-messenger astronomy. Multi-messenger astronomy covers the use of various messengers to learn about the universe around us. Optical observations were extended over a wider part of the electromagnetic spectrum and the detection of cosmic rays, neutrinos and gravitational waves are enhancing our understanding of cosmic phenomena. This chapter will cover neutrino astronomy and its connections to high-energy cosmic rays. Neutrino production and candidate sources are covered, alongside an overview of recent findings relevant to the research presented in this thesis.

1.1 Cosmic rays

The Earth is constantly bombarded with energetic particles coming from outer space [4]. They are charged nuclei that consist mainly of protons (90%), alpha particles (9%) and heavier nuclei. This form of radiation is referred to as cosmic rays and the particles can reach energies up to 10^{20} eV. This is more than a million times more energetic than the accelerated protons at the Large Hadron Collider at CERN in Geneva, which is the most powerful particle accelerator on Earth.

The flux covers a large energy range and decreases dramatically with energy as shown in Figure 1.1. The cosmic ray flux below a GeV primarily emanates from the Sun, while rays with energies up to 10^{11} GeV originate from sources that remain unidentified. The flux is characterised by a power law ($\sim E^{-\gamma}$) with spectral index $\gamma = 2.7$ which increases for energies above 10^6 GeV to 3.1. This discontinuity in the spectrum is called the *knee*. Another discontinuity is at approximately 10^9 GeV and this is called the *ankle*, after which the spectral index hardens to $\gamma = 2.6$.

The Earth's atmosphere is hit with approximately 1000 cosmic rays per square meter per second. Particles with the highest energies are encountered at a rate of about 1 particle per square kilometer per year. Since their discovery more than a century ago, scientists have been attempting to resolve two key questions:

1. Where do they come from?
2. How are they accelerated?

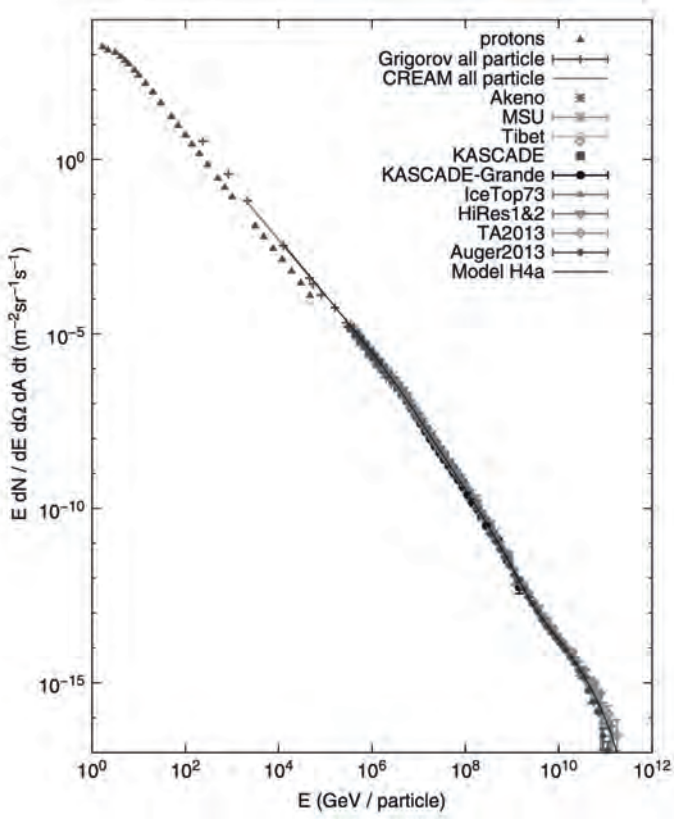

Figure 1.1: The cosmic ray flux as a function of energy. The triangles give the measured flux of protons. All other data points and model lines depict the sum of all particles as a function of the total energy per particle. Adapted from [4].

The answers to these questions are still to be found. The origin of cosmic rays is still largely unknown due to their charged nature. The magnetic fields in our universe deflect the paths of cosmic rays via the Lorentz force which poses significant challenges to trace their origin. The curvature decreases as energy increases, but higher energies present a different challenge. Greisen, Zatsepin and Kuz'min realised soon after the discovery of the cosmic microwave background that this has implications for high-energy cosmic rays [5, 6]. Protons with energies exceeding the threshold of 7×10^{19} eV colliding with the cosmic microwave background produce pions through the Δ resonance:

$$p + \gamma \to \Delta^+ \to \pi^0 + p, \tag{1.1}$$

$$\to \pi^+ + n. \tag{1.2}$$

The Δ baryons contain three quarks like protons and neutrons, but they decay swiftly via the strong interaction. The Δ production results in energy loss and this limits the distances that high-energy cosmic rays can travel before we detect them in the vicinity of Earth. This might account for the sharp decline at the highest energies of the cosmic ray spectrum, but the decline could also suggest a maximum energy of cosmic accelerators.

The question on the acceleration mechanism can partly be answered by several models described in the next section, but clear confirmation of these models is still missing.

1.1.1 Acceleration

The main acceleration mechanism of cosmic rays is believed to be explained by the theory of shock acceleration [4]. This acceleration mechanism is powered by moving clouds or shock waves of matter. These could originate from the death of stars in supernova explosions or in the vicinity of relativistic jets emitted by black holes that are accreting matter. The blast waves transfer kinetic energy to individual charged particles that are trapped in an acceleration region by magnetic fields. Each encounter of a particle with the blast wave yields an energy increase of $\Delta E = \xi E$ reaching

$$E_n = E_0(1+\xi)^n, \tag{1.3}$$

after n encounters for starting energy E_0. The probability to escape the acceleration region during a cycle is P_{esc} which results in

$$(1-P_{\text{esc}})^n \tag{1.4}$$

as the probability to remain after n encounters. The number of encounters to reach energy E_n is obtained by solving Equation 1.3 for n:

$$n = \ln\left(\frac{E}{E_0}\right) / \ln(1+\xi). \tag{1.5}$$

The proportion of particles with energies greater than or equal to E_n is given by summing over the probabilities to remain in the acceleration region:

$$N(\geq E_n) \propto \sum_{m=n}^{\infty}(1-P_{\text{esc}})^m = \frac{(1-P_{\text{esc}})^n}{P_{\text{esc}}}, \tag{1.6}$$

using the geometric series of $\sum_n^{\infty}(1-a)^n = \frac{(1-a)^n}{a}$. Substituting Equation 1.5 into 1.6 yields

$$N(\geq E_n) \propto \frac{1}{P_{\text{esc}}}(1-P_{\text{esc}})^{\ln\left(\frac{E}{E_0}\right)/\ln(1+\xi)} = \frac{1}{P_{\text{esc}}}\left(\frac{E}{E_0}\right)^{-\ln\left(\frac{1}{1-P_{\text{esc}}}\right)/\ln(1+\xi)}. \tag{1.7}$$

The energy spectrum is found by differentiating with respect to energy and is proportional to

$$\frac{dN}{dE} \propto E^{-\gamma}, \tag{1.8}$$

where the spectral index is defined as

$$\gamma = \ln\left(\frac{1}{1-P_{\text{esc}}}\right) / \ln(1+\xi) + 1. \tag{1.9}$$

Both the numerator and denominator of the first term can be expanded in order to obtain

$$\gamma \approx \frac{P_{\text{esc}}}{\xi} + 1. \tag{1.10}$$

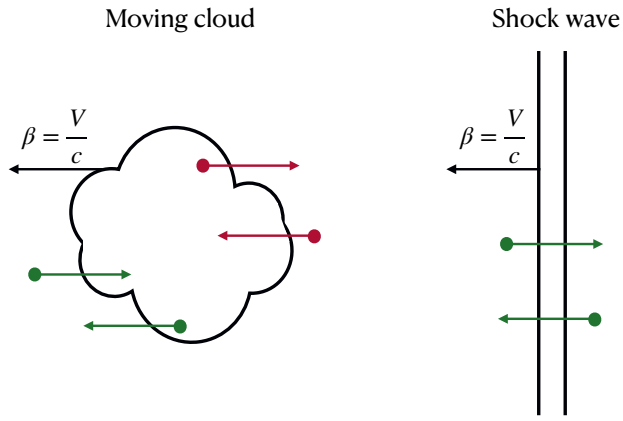

Figure 1.2: Shock acceleration using a moving cloud of plasma (left) and a shock wave (right). Charged particles scatter without collision on the magnetic fields and gain or lose energy dependent on their relative direction with the cloud of shock wave. Energy gain is indicated with green and energy loss with red. See the text for an explanation.

The derived energy spectrum of cosmic ray particles reproduces the characteristic power law spectrum, but an estimate for the spectral index γ is still missing. A prediction for γ can be obtained by estimating ξ and P_{esc}.

The original acceleration mechanism proposed by Fermi considered a particle that is accelerated by a moving plasma cloud of ionised gas [7]. A cosmic ray particle enters the gas cloud and scatters without collision on the irregularities in the magnetic field. The interaction with the cloud concludes once the particle exits, leading to either an energy gain or loss. As is shown in Figure 1.2, this outcome depends on the relative direction of the entering and departing particle with respect to the direction of the cloud's motion. The surrounding magnetic fields cause the particle to traverse the cloud several times which leads to an average increase of energy. This is explained by the velocity V of the cloud which results in slightly more particles entering the cloud head-on, yielding an energy increase. The average energy increase of an encounter is approximated by

$$\xi \sim \frac{4}{3}\left(\frac{V}{c}\right)^2 = \frac{4}{3}\beta^2, \tag{1.11}$$

where c is the speed of light. This process is second order in the cloud velocity β and is called second order Fermi acceleration. This is an inefficient way to accelerate cosmic rays due to small values of β. The estimated shock velocity of galactic shock waves around the structures that result from supernovae, called supernova remnants (SNRs), is believed to be $\sim 10^4$ km s^{-1} which results in $\beta \approx 3 \times 10^{-2}$ [8].

First order fermi acceleration considers a particle moving back and forth across a moving shock front as shown in Figure 1.2. The crucial difference with second order acceleration is that we now consider a moving plane instead of a cloud. An encounter is defined as a

particle crossing the shock front twice. Both movements lead to an energy increase of the particle with an average of

$$\xi \sim \frac{4}{3}\beta, \tag{1.12}$$

which is first order in β.

The determination of the escape probability for an astrophysical shock is complex and highly dependent on the specifics of the shock wave. It is estimated using hydrodynamics for an ideal scenario [9] to be

$$P_{\text{esc}} \approx \frac{4}{3}\beta. \tag{1.13}$$

The resulting spectral index using first order acceleration is

$$\gamma \approx \frac{P_{\text{esc}}}{\xi} + 1 \approx 1 + 1 = 2, \tag{1.14}$$

which is close to the observed spectrum. This calculation does not include energy losses through interactions with surrounding matter and radiation, which increases the expected spectral index.

Another reason for the deviating spectral index is found in the propagation of cosmic rays through our universe. The Larmor radius of a cosmic ray is defined as the radius of the circular path that a charged particle follows as it spirals around magnetic field lines. It is calculated using

$$r_L = \frac{pc}{qB} \tag{1.15}$$

where p is the momentum of the particle, q the charge and B the magnetic field strength. If the Larmor radius is smaller than the size of our Galaxy, cosmic rays can be confined within it, resulting in a higher detection rate of these energies.

1.1.2 Cosmic ray sources

The Larmor radius can also be used to calculate a maximum cosmic ray energy for a given source. This upper limit is calculated using

$$r_L < R, \tag{1.16}$$

where R is the size of the astrophysical object. At relativistic energies where $E \approx pc$ one obtains a maximum energy of

$$E_{\text{max}} = qBR, \tag{1.17}$$

which is known as the Hillas criterion [10]. The magnetic field strength and cosmological object sizes are shown in Figure 1.3 where the diagonal lines depict limits on the maximum energy per charge.

The Hillas criterion helps to understand the measured cosmic ray spectrum and provides us with a number of potential objects that can produce high-energy cosmic rays. Important sources and their place in the spectrum are listed below:

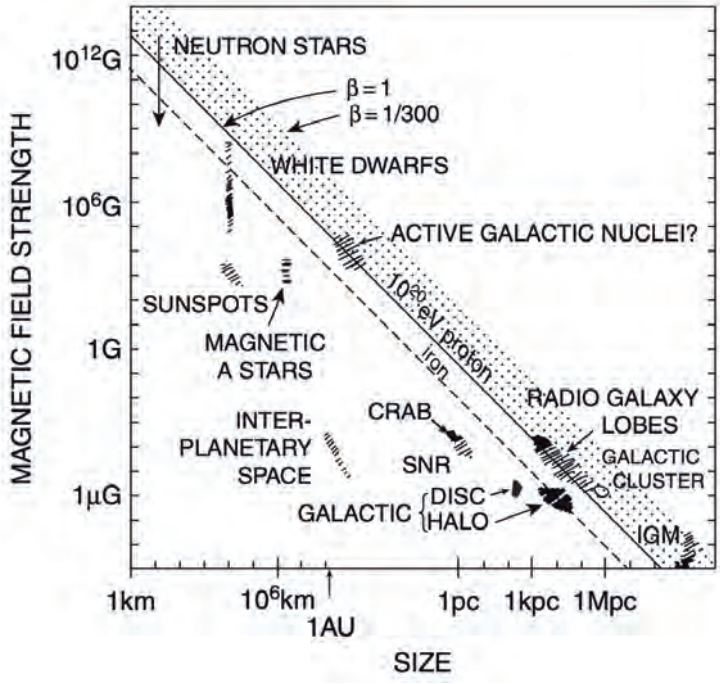

Figure 1.3: The Hillas plot of potential cosmic ray sources. The magnetic field strength and size of various accelerators is shown. The area to the left of the diagonals represent sources that can't accelerate particles up to 10^{20} eV where the solid line depicts protons and the broken line iron. The dots represent different shock velocities for the acceleration of a proton. Adapted from [4].

- **Supernova remnant** (SNR). The explosion due to the collapse of the core of a massive star is called a supernova. The resulting supernova remnant has a shock wave that can accelerate matter. They can not be responsible for the highest-energy cosmic rays due to the magnetic field strength and size of the shock front, but they can produce cosmic rays with an energy up to 10^6 GeV. It is believed that this upper limit causes the knee in the cosmic ray spectrum, and that Galactic SNRs dominate the spectrum up to that energy [4]. Reference [11] underlines Galactic SNRs as the main cosmic ray accelerators up to the knee but states that SNRs can accelerate cosmic rays up to 10^8 GeV. The knee in the cosmic ray spectrum is attributed to the shift from proton acceleration to the acceleration of heavier nuclei.

- **Active galactic nucleus** (AGN) is a black hole in the center of a galaxy. The accretion of matter results in two jets at opposite sides of the accretion disk. These jets can accelerate particles up to an energy of 10^{11} GeV [4]. AGNs are considered as prime candidates for the main source of extragalactic cosmic rays [12].

- **γ-ray bursts** (GRBs) are extremely bright electromagnetic events. It is believed that the bursts are produced by the collapse of massive stars or in relativistic jets of AGNs. At the time when Hillas produced his famous graph, GRBs were not fully

understood but they can accelerate protons up to 10^{11} GeV energies [4].

These sources among others will be explored in greater detail in the subsequent sections focusing on neutrino production.

1.2 Neutrino production

A promising solution in finding the sources of cosmic rays is the detection of galactic and extra galactic neutrinos [4]. Neutrinos are elementary particles that are described by the Standard Model of particle physics. Neutrinos are chargeless particles with an infamously small interaction cross section with matter. They travel through our universe in straight lines and they can escape dense regions. This makes them ideal messengers from distant astrophysical objects. The interaction of cosmic rays near their source produces pions via hadronuclear reactions described by

$$p + p \rightarrow p + n + \pi^+, \tag{1.18}$$
$$\rightarrow p + p + \pi^0, \tag{1.19}$$

and

$$p + n \rightarrow p + n + \pi^0, \tag{1.20}$$
$$\rightarrow p + p + \pi^-. \tag{1.21}$$

Hadronuclear reactions generate an approximate equal portion of charged and neutral pions.

Photohadronic interactions of cosmic ray protons with photons occur via

$$p + \gamma \rightarrow \Delta^+ \rightarrow \pi^0 + p, \tag{1.22}$$
$$\rightarrow \pi^+ + n, \tag{1.23}$$

which is the same process as the interaction of protons with the cosmic microwave background photons in Equation 1.1. The virtual Δ^+ resonance undergoes decay to a neutral pion $\sim 67\%$ of the time and to a positive pion $\sim 33\%$ of the time [13].

The neutral pions decay to two photons via

$$\pi^0 \rightarrow \gamma + \gamma. \tag{1.24}$$

The distant universe is opaque to high-energy γ-rays due to interactions with low-energy photons. They are absorbed through pair-production with extragalactic background light and the cosmic microwave background. This limits the distance in which γ-rays can aid in the finding of cosmic ray sources.

The charged pions decay into muons and neutrinos via

$$\pi^+ \rightarrow \nu_\mu + \mu^+ \tag{1.25}$$
$$\mu^+ \rightarrow e^+ + \bar{\nu}_\mu + \nu_e, \tag{1.26}$$
$$\pi^- \rightarrow \bar{\nu}_\mu + \mu^- \tag{1.27}$$
$$\mu^- \rightarrow \bar{\nu}_\mu + e^- + \nu_\mu + \bar{\nu}_e, \tag{1.28}$$

after the decay of the muon. Neutrinos are also produced via the decay of kaons according to

$$K^+ \rightarrow \mu^+ + \nu_\mu, \tag{1.29}$$
$$K^- \rightarrow \mu^- + \bar{\nu}_\mu, \tag{1.30}$$

or through the decay of a kaon to pions, that subsequently decay into neutrinos.

The pions carry approximately 20% of the energy of the initial proton. The four leptons after the decay of a charged pion carry approximately equal energy. Therefore, the neutrinos from pion decays carry approximately 5% of the initial proton energy.

1.2.1 Neutrino oscillations

For many years the neutrino mass was believed to be zero until the Super-Kamiokande Collaboration provided compelling evidence of neutrino oscillations in atmospheric neutrinos [14]. Their analysis showed that atmospheric ν_μ disappeared when travelling to the detector, which suggested that they transformed in another type of neutrino that was not detectable by the instrument. This phenomenon was confirmed by the Super-Kamiokande Collaboration and the Sudbury Neutrino Observatory when they published their results on solar neutrinos [15, 16]. They showed that the deficit of solar ν_e is found in ν_μ and ν_τ. The fusion processes in the Sun can not produce ν_μ and ν_τ and therefore evidence for neutrino flavour oscillations was found, which implies a non-zero mass for neutrinos.

The oscillation of neutrinos originates from the difference between the neutrino mass and weak eigenstates. The weak eigenstates ν_e, ν_μ and ν_τ are produced in the weak interaction along with a lepton of corresponding flavour:

$$\begin{pmatrix} \nu_e \\ e^- \end{pmatrix}, \begin{pmatrix} \nu_\mu \\ \mu^- \end{pmatrix}, \begin{pmatrix} \nu_\tau \\ \tau^- \end{pmatrix}. \tag{1.31}$$

The weak eigenstates are not the same as the mass eigenstates ν_1, ν_2 and ν_3 in which they propagate. Each weak eigenstate is a mixture of all three mass eigenstates and the mixing is described by

$$\begin{pmatrix} \nu_e \\ \nu_\mu \\ \nu_\tau \end{pmatrix} = \begin{pmatrix} U_{e1} & U_{e2} & U_{e3} \\ U_{\mu 1} & U_{\mu 2} & U_{\mu 3} \\ U_{\tau 1} & U_{\tau 2} & U_{\tau 3} \end{pmatrix} \begin{pmatrix} \nu_1 \\ \nu_2 \\ \nu_3 \end{pmatrix}, \tag{1.32}$$

where U is the unitary Pontecorvo-Maki-Nakagawa-Sakata matrix. A muon neutrino propagates as a linear combination of the mass eigenstates according to

$$|\psi(\mathbf{x}, t)\rangle = U^*_{\mu 1} |\nu_1\rangle e^{-\phi_1} + U^*_{\mu 2} |\nu_2\rangle e^{-\phi_2} + U^*_{\mu 3} |\nu_3\rangle e^{-\phi_3}, \tag{1.33}$$

where $\phi_i = E_i t - \mathbf{p_i} \cdot \mathbf{x}$ is the phase of the plane wave that represents each mass eigenstate. The mass differences between the neutrino mass eigenstates ν_1, ν_2 and ν_3 result in phase differences within the wavefunction, causing a neutrino of one flavour to oscillate into another flavour. This can be understood when expressing the wave function in terms of the weak eigenstates. The oscillation probabilities for neutrinos in vacuum can be calculated by projection of the initial neutrino flavour eigenstate $|\nu_\alpha\rangle$ onto $|\nu_\beta\rangle$ using

$$P(\nu_\alpha \rightarrow \nu_\beta) = |\langle \nu_\beta | \nu_\alpha \rangle|^2 = |\sum_i U^*_{\alpha i} U_{\beta i} e^{-i \frac{m_i^2 L}{2E}}|^2, \tag{1.34}$$

where m_i is the mass of eigenstate i and L is the distance travelled. This can be rewritten to

$$P(\nu_\alpha \to \nu_\beta) = \delta_{\alpha\beta} - 4\sum_{i>j} \mathrm{Re}(U^*_{\alpha i}U_{\beta i}U_{\alpha j}U^*_{\beta j}) \sin^2(\frac{\Delta m^2_{ji}L}{4E}) \tag{1.35}$$

$$+ 2\sum_{i>j} \mathrm{Im}(U^*_{\alpha i}U_{\beta i}U_{\alpha j}U^*_{\beta j}) \sin^2(\frac{\Delta m^2_{ji}L}{2E}), \tag{1.36}$$

where the oscillation probabilities depend on the mass splitting Δm_{ji} between the mass eigenstates, the matrix U, the neutrino energy and distance travelled. The mass splitting is defined as $\Delta m_{ji} = m^2_j - m^2_i$.

The oscillation probability simplifies when considering a hypothetical scenario with two neutrino flavours. This results in an oscillation probability of

$$P(\nu_\alpha \to \nu_\beta) = |\langle \nu_\beta | \nu_\alpha \rangle|^2 = \sin^2(2\theta)\sin^2(\frac{\Delta m^2_{ji}L}{4E}), \tag{1.37}$$

with a single mass difference Δm and a single mixing angle θ.

1.2.2 Flavour ratio

The expected neutrino flavour ratio for $\nu + \bar{\nu}$ at a source is approximated by

$$\nu_e : \nu_\mu : \nu_\tau = 1 : 2 : 0, \tag{1.38}$$

when considering the dominant neutrino production channels via the decay of pions and kaons [4]. Hadronic interactions can also generate charm quark pairs leading to the creation of heavier mesons [17]. This can lead to the production of D mesons, which are the lightest mesons containing a charm quark. The D_s ($c\bar{s}$) meson has a decay channel of

$$D_s \to \tau + \nu_\tau, \tag{1.39}$$

producing a ν_τ with a branching ratio of a few percent. There are heavier mesons contributing to the production of ν_τ, but their contribution is minor compared to that of the D_s meson.

The 1:2:0 scenario assumes that the muon decays before it loses its energy, but strong magnetic fields can cause energy losses via synchrotron radiation. This results in the muon-damped flavour ratio of 0:1:0 for high-energy neutrinos due to the low energy of the produced ν_e. The ratio of 1:2:0 oscillates to 1:1:1 over large distances as described in Reference [18], while the muon-damped flavour ratio scenario leads to deviations from equal flavour contributions. Therefore, a measurement of the neutrino flavour ratio at Earth can shed light on the environment of cosmic ray acceleration and neutrino production.

1.2.3 Flux

The expected neutrino flux from sources like gamma-ray bursts and AGNs can be obtained by an approximation from Waxman and Bahcall [19]. Their work assumes that most cosmic rays are protons and that a fraction of their energy is transferred to neutrinos. The energy injection rate $\dot{\epsilon}$ in protons per unit volume of high-energy cosmic rays is constrained

using the measured flux on Earth. The rate is estimated at $\dot{\epsilon} = 0.5 \times 10^{44}$ ergs Mpc^{-3} yr^{-1} when assuming that cosmic rays above 10^{19} eV are of extragalactic origin and made up of protons [20]. The upper bound on the neutrino flux can be obtained using the Waxman-Bahcall bound [19] which states that cosmic ray protons interact with ambient radiation via

$$p + \gamma \rightarrow \Delta^+ \rightarrow n + \pi^+. \tag{1.40}$$

The essential point is that the high-energy protons engage in this interaction not more than once. The proton converts to a neutron and loses it charge, which results in the escape of the cosmic ray from the magnetic fields around the source. The neutron decays back to a proton that can be detected at Earth. The neutrino energy density is directly tied to the energy injection rate and leads to an upper bound of

$$E_\nu^{-2}\phi_{\mathrm{WB}} \approx 3 \times 10^{-8} \text{ GeV cm}^{-2} \text{ s}^{-1} \text{ sr}^{-1} \tag{1.41}$$

where ϕ_{WB} is the all-flavour astrophysical neutrino flux.

1.3 Neutrino source candidates

The potential sources for high-energy cosmic rays are also source candidates for astrophysical neutrinos [4]. Any object that accelerates protons should also be able to produce neutrinos. The following sections will extend upon the discussed cosmic rays source candidates and elaborate on their possible mechanisms for neutrino production.

1.3.1 Active galactic nuclei

Certain galaxies have a core that outshines the rest of the galaxy [21]. These cores are known as AGNs and they are defined by their broad spectrum emissions ranging from radio to γ-rays which varies significantly over time. AGNs are powered by a supermassive black hole that attracts matter from the surrounding accretion disc and dust torus. The released gravitational energy powers two jets perpendicular to the accretion disc.

Classification of AGNs is done depending on the intensity of emission lines at different wavelengths. The presence of radio emission from the jets characterises radio-loud AGNs (10-15%), while the absence covers radio-quiet AGNs. AGNs are also classified based on the optical part of their spectrum. Type 1 AGNs display a bright continuum with emission lines, while type 2 AGNs exhibit a weak continuum and narrow emission lines.

The radio-loudness of an AGN is associated with the presence of relativistic jets. This is thought to be influenced by the surrounding matter and the black hole's spin. Specific conditions may activate relativistic jets, leading to radio emissions. The presence of jets in AGNs means that our observations of these objects are significantly influenced by the viewing angle. The galaxies surrounding AGNs are classified as Seyfert type I and II depending on their orientation with respect to the line of sight from Earth. In Seyfert Type I galaxies, the region surrounding the supermassive black hole is visible, whereas in Type II galaxies, this central area is hidden behind a torus of dust and gas. The classification of AGNs using the viewing angle from Earth is shown in Figure 1.4.

Blazars represent a relatively rare but important subclass of AGNs, characterised by having their jets directed towards Earth. Astronomers have identified over 3500 blazars

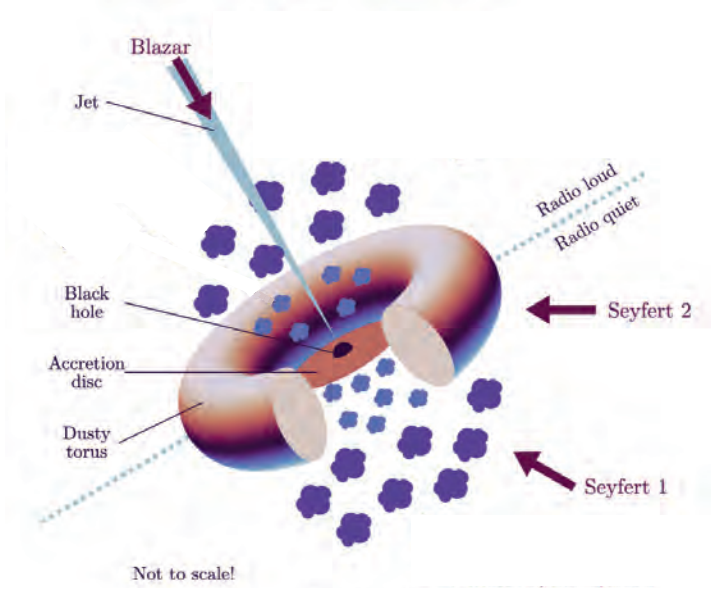

Figure 1.4: The naming of active galactic nuclei with respect to the viewing angle from Earth. Adapted from [22].

which are classified using the emission spectrum [23]. The spectral energy distributions of light from blazars have two typical peaks between infrared and x-ray wavelengths and at high-energy via γ-rays [24]. The low-energy peak is attributed to synchrotron emission of electrons and can be used to classify blazars in low, intermediate and high synchrotron peak objects. Optical emission lines are characteristic of flat-spectrum radio quasars (FSRQs). The emission lines are hidden under a strong continuum emission for BL Lac objects.

Blazars are extensively studied using γ-rays and they are potential sources for ultra-high-energy cosmic rays. The γ-ray emission can be caused by the decay of neutral pions, which are typically accompanied by charged pions that decay into neutrinos. Neutrinos from blazars could be produced in the surrounding accretion disc or from the relativistic jets [25].

1.3.2 Supernovae

The gravitational force of a star is balanced by the radiation pressure from nuclear reactions in the core [4]. This equilibrium disappears when the star runs out of fuel, leading to the collapse of its core. This phenomenon is known as a core-collapse supernova, which results in the formation of either a neutron star or a black hole. The vast majority of the gravitational potential is emitted in the form of neutrinos with MeV energies. The first and sole observation of neutrinos from a supernova occurred with SN 1987A in the Large Magellanic Cloud. Three detectors simultaneously measured several neutrinos hours prior to the optical explosion [26–28], while the Mont Blanc Underground Neutrino Observatory detected an additional five events approximately 5 hours before the rest [29].

Core-collapse supernovae also serve as promising sources of high-energy neutrinos [30]. GeV to TeV neutrinos could be produced if the star is surrounded by a dense circumstellar material, which serves as target material for the ejecta from the supernova. The resulting shocks accelerate protons and produce neutrinos via hadronuclear or photohadronic interactions. The faint signals from MeV neutrinos provide challenges in detection and limit the detection horizon of current detectors. The number of observable supernovae could be increased when studying high-energy neutrinos. The combined detection of MeV and high-energy neutrinos from a Galactic supernova will provide valuable insights on cosmic ray acceleration and neutrino production. The frequency of supernovae occurring within our Galaxy is estimated to be several times per century, with high-energy neutrinos anticipated to arrive up to 10 days to a year following the initial MeV neutrino signal depending on the type of supernova [31, 32]. Some core-collapse supernovae produce very bright bursts of γ-rays, which are discussed in the following section.

1.3.3 Gamma-ray bursts

Gamma-ray bursts (GRBs) were accidentally discovered by the Vela satellites when searching for fast flashes of gamma-rays induced by the testing of nuclear weapons [21, 33]. They are the most energetic phenomena in our universe and they typically last a few seconds. Long bursts ($t > 2$ s) are believed to be caused by the emergence of a black hole after the death of a massive star, while short bursts ($t < 2$ s) correspond to the merger of two compact objects. It remains uncertain whether a GRB primarily expels matter or electromagnetic radiation, and whether the dissipation of energy occurs through internal or external shocks. The possible production of ultra-high-energy cosmic rays and high-energy neutrinos depends on the presence of baryons which are accelerated inside the jets. The short rise time of the burst requires a compact fireball which expands relativistically due to radiation pressure. Shocks are produced that can accelerate particles and high-energy neutrinos could be produced from interactions of protons with photons, which leads to a burst of neutrinos [34].

1.3.4 The Galactic plane

The dominant γ-ray source above 1 GeV is the plane of the Milky Way [4, 35]. These photons can be produced by interactions of high-energy electrons with interstellar photon fields or through high-energy cosmic rays that collide with the interstellar medium to produce neutral pions that decay into two photons. In addition to neutral pions, charged pions are also produced which decay into neutrinos. These processes predict a diffuse neutrino flux from the Galactic plane, alongside point-like neutrino emission from high-energy γ-ray sources.

1.3.5 Background neutrino sources

The detection and identification of astrophysical neutrinos from any Galactic or extragalactic candidate source is complicated by background sources. The following neutrino sources are considered as background for neutrino astronomy, but they are regarded as valuable subjects of study in other research areas. The neutrinos from the Sun and fusion reactors do not impact the analyses in this work, as the astrophysical neutrino candidates investigated here span energies from several hundred GeV to PeV.

Solar neutrinos

The nuclear fusion processes in the Sun produce an immense neutrino flux [3]. The flux of 2×10^{38} ν_e s^{-1} yields approximately 7×10^{10} ν_e s^{-1} cm^{-2} at the Earth's surface. The main hydrogen burning process produces neutrinos via

$$p + p \rightarrow D + e^{+} + \nu_e. \tag{1.42}$$

These neutrinos have energies below 0.5 MeV and are difficult to detect. The highest-energy neutrinos from the Sun are produced from the β-decay of ^{8}B which is produced from the fusion of two helium nuclei, resulting in neutrinos that reach energies of 15 MeV.

Reactor neutrinos

Nuclear reactors produce a large flux of $\bar{\nu}_e$ through nuclear fission [3]. Fission products like ^{235}U, ^{238}U, ^{239}Pu and ^{241}Pu undergo β-decay which yields neutrinos of approximately 3 MeV. The neutrino flux can be calculated from the produced power of the reactor. The power is monitored closely, allowing for precise estimations of the neutrino flux.

Atmospheric neutrinos

Cosmic rays impacting the Earth's atmosphere generate neutrinos in a similar way compared to the processes near cosmic ray accelerators. The atmospheric neutrino flux is categorised in a conventional and prompt component [36]. The conventional neutrino flux originates from the decay chain of pions and kaons. The prompt component emerges from the decay of heavier mesons containing a charm quark. The conventional neutrino flux dominates up to approximately 100 TeV due to the higher pion and kaon production cross section. The conventional neutrino energy spectrum follows the cosmic ray spectrum of $\gamma = 2.7$, but with slightly higher γ due to energy losses of the pions and kaons in the atmosphere. The decay length of secondary hadrons increases with the initial interaction energy, which transitions the dominant neutrino production to the decay of charmed mesons. The rapid decay of these particles causes the neutrinos to more closely mimic the cosmic ray spectrum.

The conventional and prompt neutrino flux can be further distinguished by their angular distribution. The prompt contribution is isotropically distributed due to the rapid decay of the heavy mesons. The conventional flux is maximal for horizontal directions due to the density of the atmosphere. The cosmic ray interaction products have more time to decay before reaching denser regions of the atmosphere, compared to vertical downgoing cosmic rays. For energies above 10 TeV, the upgoing neutrino flux is attenuated through interactions in the Earth.

Similar to neutrinos from cosmic accelerators, atmospheric neutrinos undergo oscillations as they travel through the atmosphere and the Earth. These oscillations are neglected at the energies considered in this work, because the oscillation length of TeV neutrinos exceeds the diameter of the Earth.

The prompt ν_τ flux is over ten times lower than the prompt ν_μ flux due to the single production channel via the D_s meson [37]. Other D mesons typically decay to pions and kaons, producing more ν_e and ν_μ. The estimated number of prompt ν_τ interactions per year per km^3 water equivalents is of the order of 20 events for energies above 1 TeV [17], reducing further for higher energy thresholds.

1.4 Discoveries

The field of neutrino astronomy has gained significant attention in the last decade thanks to discoveries of the IceCube Collaboration. The IceCube detector is a neutrino observatory buried in the ice of Antarctica [38]. It is designed to detect astrophysical neutrinos through the detection of Cherenkov radiation from neutrino interaction products. It has been taking data using the complete detector since May 2011 and has had a leading role in neutrino astronomy discoveries.

The ANTARES detector, the predecessor of the KM3NeT detector which is the subject of this thesis, utilises a similar detection principle in seawater instead of ice [39]. The detector was decommissioned after 15 years of data taking and showed compatible results with IceCube, but lacks statistical significance due to the limited instrumented volume.

The following sections cover recent developments in the field of neutrino astronomy and open points to be answered.

1.4.1 The discovery of astrophysical neutrinos

In 2013, the IceCube Collaboration found evidence for neutrinos of extraterrestrial origin [40]. They observed 28 candidate events over an expected background of 10 events, resulting in a significance of 4σ that the observed dataset is produced by atmospheric neutrinos. The energies ranged from 30 TeV to 1.2 PeV and the energy spectrum was harder than expected from cosmic ray acceleration ($\gamma = 2$).

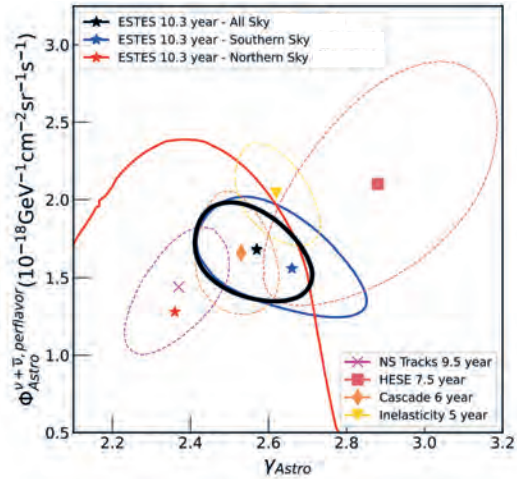

Figure 1.5: Summary of the astrophysical diffuse neutrino flux using a single power law. The contours represent 68% confidence level intervals for the flux normalisation (y-axis) and spectral index γ (x-axis) using different event samples of the IceCube neutrino observatory. Obtained from [41].

This analysis has been extended with additional data and improved event selections [42]. A 9.5 year sample of muons from ν_μ interactions was used to characterise the ν_μ flux using a single power-law:

$$\Phi^{\nu_\mu+\bar{\nu_\mu}} = \phi^{\nu_\mu+\bar{\nu_\mu}}_{@100\mathrm{TeV}} \left(\frac{E_\nu}{100\mathrm{TeV}}\right)^{-\gamma}, \tag{1.43}$$

$$\phi^{\nu_\mu+\bar{\nu_\mu}}_{@100\mathrm{TeV}} = 1.44^{+0.25}_{-0.26} \times 10^{-18}\ \mathrm{GeV}^{-1}\ \mathrm{cm}^{-2}\ \mathrm{s}^{-1}\ \mathrm{sr}^{-1}, \tag{1.44}$$

$$\gamma = 2.37^{+0.09}_{-0.09}, \tag{1.45}$$

for energies between 15 TeV to 5 PeV. The results are shown in Figure 1.5 labelled as NS tracks 9.5 year. Other analyses used events from ν_μ with an interaction vertex inside the detector (ESTES 10.3 year) [41] and particle cascades from ν_e and ν_τ interactions (Cascade 6 year) [43]. The varying event selections and analyses cover different energy ranges and neutrino flavour compositions. It is believed that they probe different neutrino sources and cosmic ray acceleration mechanisms, but they are considered to be in agreement. The largest contour is using the high-energy starting events (HESE) with a minimum energy of 60 TeV, which limits the flux measurement to higher energies and results in limited statistics.

The isotropic nature of the astrophysical neutrino flux detected by the IceCube Collaboration suggests that a significant fraction of the neutrinos is of extragalactic origin [24]. As shown in the conclusion of this chapter, neutrino production in the Galactic plane amounts to 6-13% of the astrophysical neutrino flux at 30 TeV [44].

1.4.2 TXS 0506+056

On 22 September 2017, The IceCube Collaboration reported a high-energy ν_μ event which triggered an automatic alert that was sent to other neutrino telescopes and various multi-wavelength observatories [45]. The neutrino energy was estimated at 290 TeV and the direction is in spatial coincidence with the γ-ray blazar TXS 0505+056. Due to the presence of a neutrino flux of atmospheric origin at these energies, there is a 56.6% chance that the neutrino originates from an astrophysical source. The IceCube Collaboration found an independent excess of neutrinos from this direction with 3.5σ significance between September 2014 and March 2015 [46].

The Fermi Large Area γ-ray Telescope established that the γ-ray source was in an enhanced state of emission [47]. Initial follow-up searches by the Major Atmospheric Gamma Imaging Cherenkov (MAGIC) Telescope [48] did not detect γ-ray emission, but a significant high-energy γ-ray signal was found on 28 September 2017 with energies up to 400 GeV with a statistical significance of 6.2σ [45]. Other very-high-energy γ-ray telescopes like H.E.S.S. and Veritas did not make significant detections, but their upper limits are consistent with the observed flux from the MAGIC Telescope [45].

Observations in radio, optical and x-ray wavelengths were performed and showed strong variabilities as expected for a flaring blazar. A gradual increase of radio emission was detected in the 18 months prior to the neutrino alert. Optical observations established that the visible band of the source was at the highest level observed in recent years. An increase of x-ray emission was detected in the 4 weeks after the alert.

The ANTARES detector performed a follow-up search and found no neutrino candidate in $\pm$ 1 day around the IceCube alert [49].

The multi-messenger observation of TXS 0506+056 presents evidence for neutrino production in the vicinity of blazars, but further observations are needed to establish the correlation between blazars and high-energy neutrinos. An analysis presented in Reference [24] used the Fermi-LAT 2LAC catalog which covers 70% of the total γ-ray flux from all GeV blazars in the observable universe. No significant cumulative excess of neutrinos was observed in the IceCube dataset from the 862 sources. The upper limits constrain the contribution of 2LAC blazars to the astrophysical neutrino flux to 27% or less between neutrino energies of 10 TeV and 2 PeV.

1.4.3 NGC 1068

The IceCube Collaboration found an excess of neutrinos coming from nearby active galaxy NGC 1068 with 4.2σ statistical significance [50]. The galaxy has a supermassive black hole at its center and has significant starburst activity, which entails a high rate of star formation. The central region of the galaxy is hidden behind a torus of dust and gas, which classifies NGC 1068 as a Seyfert Type II galaxy. The neutrino emission from NGC 1068 hints that AGNs could be a significant fraction of the neutrino sources that produce the astrophysical neutrino flux. The combined neutrino flux from TXS 0506+056 and NGC 1068 accounts for approximately 1% of the overall astrophysical neutrino flux within the observed energy spectra.

1.4.4 Galactic plane

Initial searches of the IceCube Collaboration have not made a statistical significant observation until 2023 [44]. Improvements in selection and reconstruction using machine learning increased the neutrino cascade sample and improved the reconstruction performance. These efforts led to the detection of a diffuse neutrino flux from the Galactic plane, achieving a statistical significance of 4.5σ. The signal can also be explained by a group of unresolved point sources, which highlights the need for new detectors with improved angular resolution.

1.4.5 Flavour ratio

The HESE neutrino sample of IceCube contained two candidate tau neutrinos among 60 collected in 7.5 years of operation [51]. The first event was recorded in 2012 and the energy was estimated at 1.8 PeV. The second event dated from 2014 with an energy of 88 TeV. This data sample was used to constrain the flavour ratio of astrophysical neutrinos. The best-fit flavour composition was found at 0.20:0.39:0.42 and is shown with a star in Figure 1.6. The three axes represent the fraction of ν_e, ν_μ and ν_τ of the neutrino flux, with their total sum always adding up to 1. The 68% and 95% confidence level contours are shown with the solid and dashed lines. Several flavour ratios after propagation to Earth are depicted, and all are contained inside the 95% confidence level contour. These results are expected to improve after finding another 5 candidates [52]. The absence of an astrophysical ν_τ flux is ruled out with 5σ significance.

1.5 Outlook

The observations by the IceCube and ANTARES collaborations paved the way for the field of neutrino astronomy. Numerous ideas for new detectors are under discussion and several detectors are currently under construction. The IceCube Collaboration will carry out an upgrade of the detector to improve the sensitivity to neutrino oscillations [54]. Additionally, this upgrade will provide new calibration devices that will reduce the systematic uncertainties of the detector and improve the resolutions of the astrophysical neutrino dataset. This upgrade is planned for the end of 2025 and more ambitious ideas are currently under discussion. The IceCube-Gen2 proposal aims to extend the instrumented volume of 1 km^3 to 10 km^3 which improves the sensitivity to high-energy neutrinos. This detector could significantly extend the PeV neutrino sample and reach EeV energies.

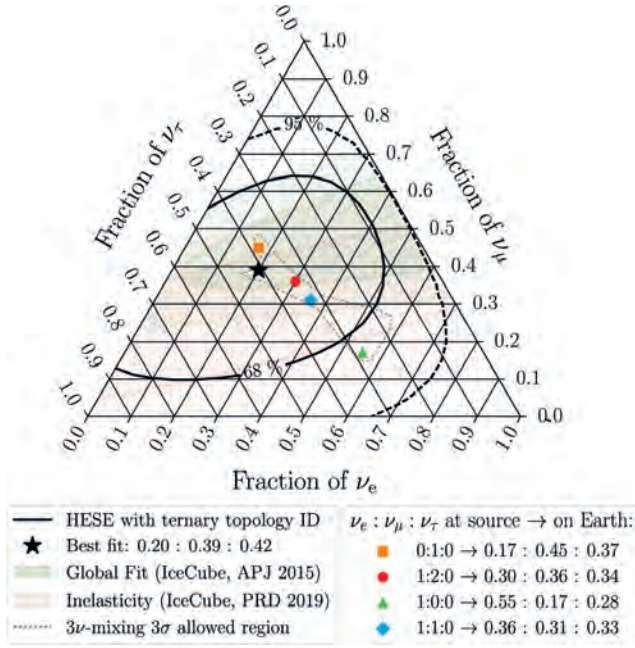

Figure 1.6: Measured flavour ratio of the HESE sample of the IceCube Collaboration. The contours show the 1σ and 2σ confidence level contours assuming Wilks' theorem [53]. The shaded regions show older results that did not have sensitivity to the tau neutrino component. The coloured dots represent flavour ratios at a given source after propagation to Earth. Obtained from [51].

A new neutrino detector is under construction at the bottom of Lake Baikal in Siberia, Russia [55]. The winter deployment of 2023 increased the number of optical modules to 3456 on 96 vertical strings [56] and the latest analysis rejects a zero diffuse astrophysical neutrino flux with 3σ significance. New detectors are proposed in the Pacific Ocean (P-ONE) and in the South China Sea (TRIDENT, HUNT) [57–59].

The ANTARES detector took data between 2006 and 2022 in the Mediterranean Sea and its successor, the Cubic Kilometre Neutrino Telescope (KM3NeT), is currently under construction. This detector is the topic of this thesis.

Chapter 2

Neutrino detection

The insights that cosmic neutrinos offer are unveiled through neutrino detection. Their lack of electric charge and notoriously small interaction cross section with matter present significant challenges in their detection. Typical sources produce as many neutrinos as gamma-rays, but the small neutrino interaction cross section requires the use of very large detectors in order to observe a significant number of cosmic neutrinos above the background rate. This thesis covers research that was carried out using the KM3NeT/ARCA detector, which is a km^3 neutrino observatory that detects neutrinos via Cherenkov radiation in the Mediterranean Sea. This chapter covers the concepts of neutrino detection in water, while the next chapter focuses on the KM3NeT/ARCA neutrino detector.

2.1 Neutrino interactions with matter

Neutrinos interact with matter via the weak interaction [3]. This process is mediated by either a $W^{\pm}$ boson in charged current (CC) interactions or a Z^0 boson in neutral current (NC) interactions. The dominant process depends on the energy of the neutrino [60]. At GeV energies and below, the dominant processes are charged current quasielastic scattering and resonant scattering. At the TeV energies considered in this work, the dominant process is deep-inelastic scattering with a nucleon. The neutrino probes the quarks inside the nucleon and fragments the nucleon producing new hadronic particles. The scattering process with a nucleon is defined as

$$\mathrm{CC} : \nu_l(\bar{\nu}_l) + N \rightarrow l^-(l^+) + X, \tag{2.1}$$

$$\mathrm{NC} : \nu_l(\bar{\nu}_l) + N \rightarrow \nu_l(\bar{\nu}_l) + X, \tag{2.2}$$

where l is the lepton flavour, N the target nucleon and X the hadronic interaction products after the fragmentation of N. The interaction between neutrinos and electrons is subdominant, with the notable exception occurring at the Glashow resonance. The resonant production of a W^- boson through the interaction of an $\bar{\nu}_e$ with an electron leads to a peak in the cross section at a neutrino energy of 6.3 PeV [61]. The neutrino interaction cross sections are shown in Figure 2.1.

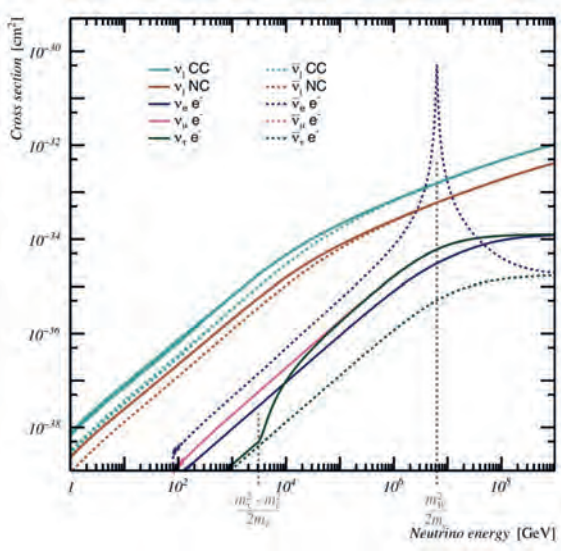

Figure 2.1: Neutrino interaction cross sections for interactions with a nucleon or an electron. The neutrino-nucleon cross sections assume an isoscalar target. The CC and NC neutrino-electron cross sections are added and represent the total cross section. Adapted from [9].

2.2 Cherenkov radiation

As a charged particle moves through matter, it causes the molecules it encounters to become polarised [3]. The molecules emit a photon when returning to their unpolarised state. If the velocity v of the particle is greater than the speed of light in that medium, constructive interference occurs. The resulting radiation is called Cherenkov radiation and is often compared to its acoustical counterpart called the sonic boom, which occurs when a plane exceeds the speed of sound in air. Cherenkov radiation is emitted at a fixed angle θ_c with the trajectory of the charged particle, which is given by

$$\cos\theta_c = \frac{1}{n\beta} \tag{2.3}$$

where n is the refractive phase index of the medium and $\beta = v/c_{\text{vacuum}}$. The Cherenkov angle for relativistic particles at the bottom of the Mediterranean Sea is 42.2°, assuming $n = 1.35$ for seawater. The minimum energy required to produce Cherenkov radiation is 0.761 MeV for an electron and 157.3 MeV for a muon. The Cherenkov angle and cone are shown in Figure 2.2.

The number of emitted photons N per unit wavelength λ per unit of distance travelled x is given by [62]:

$$\frac{d^2N}{d\lambda dx} = \frac{2\pi\alpha q^2}{\lambda^2}\left(1 - \frac{1}{n^2\beta^2}\right) \tag{2.4}$$

where q is the charge of the particle and α is the fine-structure constant. The approximate number of photons from a relativistic muon is 3.5×10^4 photons per meter. This assumes wavelengths between 300 and 600 nm where typical photomultiplier tubes are most efficient.

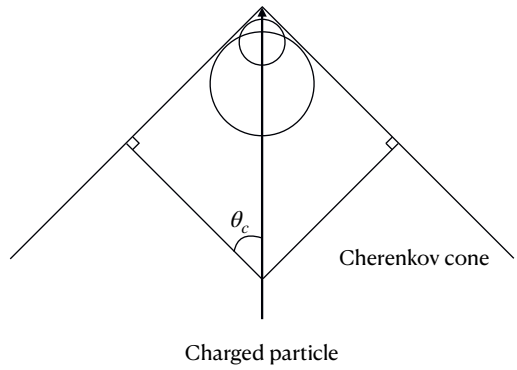

Figure 2.2: Schematic overview of the Cherenkov cone caused by a charged particle.

2.3 Light emission

The various products of neutrino interactions produce distinct light patterns when traversing matter. The most important interaction products and their corresponding energy loss and light patterns are described below.

2.3.1 Electron

At low energies, electrons primarily lose energy through ionisation [3]. Additionally, electrons travelling through a material produce bremsstrahlung photons. The electric fields of the nuclei in the medium deflect the electron which produces a photon. Above the critical energy E_c, the energy loss from bremsstrahlung becomes dominant over energy loss from ionisation. The critical energy is linked to the charge Z of the nucleus in the medium and can be described by

$$E_c \sim \frac{800}{Z} \text{ MeV}. \tag{2.5}$$

If the energy of a bremsstrahlung photon surpasses 1.022 MeV, which is twice the rest mass energy of an electron or positron (0.511 MeV), it can lead to the production of an electron-positron pair via pair production. Each of these particles can then emit additional bremsstrahlung photons.

This *cascade* or *shower* of particles and radiation is called an electromagnetic shower. The number of particles increases as the average energy per particle decreases, until the average energy drops below the threshold energy for pair production. The average energy $\bar{E}$ of the particles in the shower after x radiation lengths is approximated by

$$\bar{E} = \frac{E}{2^x}. \tag{2.6}$$

The radiation length X_0 is defined as the average distance over which the energy of an electron is reduced by a factor $1/e$ due to bremsstrahlung. It roughly matches the mean

free path of a high-energy photon in the pair production process. The radiation length in water is approximately 36 cm [63].

The maximum number of particles is reached at the critical energy below which ionisation becomes the dominant process for energy loss. This is called the shower maximum and it is reached after

$$x_{\max} = \frac{\ln(E/E_c)}{\ln 2} \tag{2.7}$$

radiation lengths. The detectable signal consists of the Cherenkov radiation from the electrons and positrons when their energy exceeds the Cherenkov threshold. The longitudinal light emission profile of electromagnetic showers is shown in Figure 2.3. An electromagnetic shower produced by a 100 TeV electron has a shower maximum after several meters. The number of photons is approximately $1.5 \cdot 10^5$ per GeV for wavelengths between 300 and 650 nm [64].

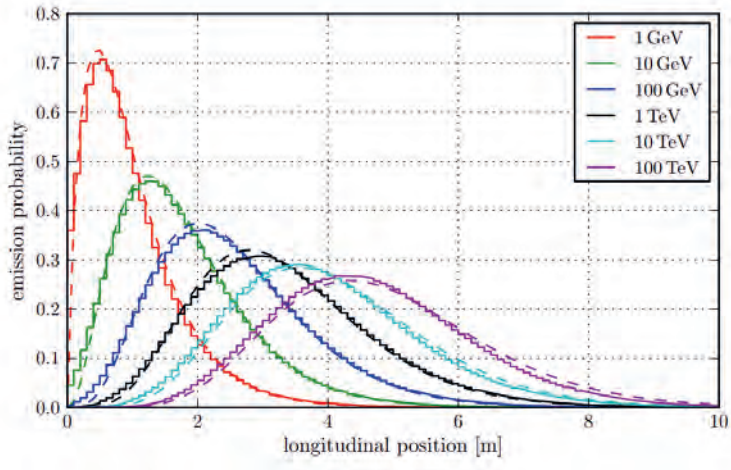

Figure 2.3: Longitudinal light emission profile for electromagnetic showers. Taken from [65].

2.3.2 Hadron

Hadrons produce similar light patterns as electrons through hadronic showers [3, 9]. The deep inelastic scattering of neutrinos cause the target nucleon to fragment which produces protons, neutrinos, pions and other hadrons. The charged pions interact with the medium producing more hadrons, while the neutral pions decay into two photons. These photons produce electromagnetic showers and the ensemble is called a hadronic shower. Neutrons and neutrinos do not emit Cherenkov light, leading to reduced light production in hadronic showers compared to electromagnetic showers. The interaction length for a hadronic shower is longer than for an electromagnetic shower, which leads to a longer longitudinal light emission profile.

2.3.3 Muon

Muons lose energy through the ionisation of the traversed medium and emit Cherenkov radiation and bremsstrahlung photons based on the same processes that govern the behaviour of electrons [3]. However, the greater mass of the muon causes a different light pattern. The energy loss due to ionisation and bremsstrahlung is inversely proportional to the square of the mass, which substantially extends the distance a muon can travel through a medium.

In addition to the processes described for an electron, a muon produces a significant amount of light via δ-rays. A δ-ray is produced when a muon removes an electron from its orbital in the medium. This electron is referred to as a δ-ray if the electron has sufficient energy to ionise the medium. Another mechanism that generates light as a muon passes through matter is known as photonuclear interactions. The inelastic scattering of the muon with a nucleus results in a hadronic shower that produces a detectable signal. The total energy loss of a muon is approximated by the formula

$$-\frac{dE}{dx} = a(E) + b(E)E, \tag{2.8}$$

where a is the energy loss due to ionisation and b is the sum of energy losses via bremsstrahlung, δ-rays and photonuclear interactions [66]. This formula can be integrated and solved for the traversed distance to obtain the average muon range

$$L = \frac{1}{b}\log\left(1 + \frac{b}{a}E_0\right), \tag{2.9}$$

where L is the muon range and E_0 is the initial muon energy. Typical values for a and b are

$$a = 2.67 \times 10^{-3}\ \text{GeV cm}^{-1} \tag{2.10}$$
$$b = 3.40 \times 10^{-6}\ \text{cm}^{-1} \tag{2.11}$$

for muon energies between 30 GeV and 35 TeV. A muon with an energy of 1 TeV can travel approximately 2.4 km.

2.3.4 Tau

The tau is the heaviest of the leptons and has a mean lifetime τ_τ of 2.903×10^{-13} s [67]. The decay happens through the weak interaction, resulting in the formation of

$$\tau^- \to \nu_\tau + e^- + \bar{\nu}_e\ (17.82\%), \tag{2.12}$$
$$\tau^- \to \nu_\tau + \mu^- + \bar{\nu}_\mu\ (17.39\%), \tag{2.13}$$
$$\tau^- \to \nu_\tau + \text{hadrons}\ (64.79\%). \tag{2.14}$$

The short lifetime causes the neutrino interaction and tau decay vertex to overlap at low energies. The tau range increases with the tau energy due to time dilatation and can be approximated at relativistic energies ($v \approx c$) by

$$L = c\tau_\tau\gamma \approx 4.9\frac{\text{cm}}{\text{TeV}}. \tag{2.15}$$

The decay of the tau particle results in the generation of a muon or it initiates an electromagnetic or hadronic shower. There is always another ν_τ in the final state that can carry a substantial amount of the initial energy due to the small energy loss during the lifetime of the tau lepton. This phenomenon is called tau regeneration and it broadens the opportunities for the detection of high-energy ν_τ that traverse or skim the Earth.

2.4 Light propagation

Light propagating through a medium undergoes scattering, absorption and chromatic dispersion. Chromatic dispersion is the phenomenon where light travels at different speeds through a medium depending on the wavelength. This occurs because the index of refraction varies with wavelength, as illustrated in Figure 2.4b.

The intensity of light is diminished due to absorption. Furthermore, the scattering of light alters the arrival time and direction at a detector. The measured absorption and scattering lengths as a function of the wavelength in the Mediterranean Sea are shown in Figure 2.4a. The absorption length is maximal at 440 nm with approximately 67 m, which corresponds to blue in the visible light spectrum.

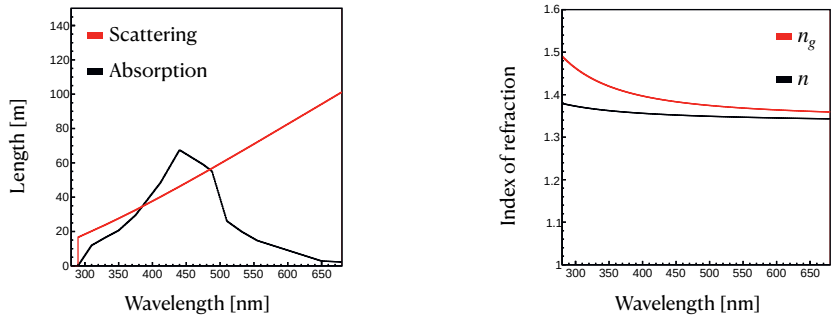

(a) (b)

Figure 2.4: Absorption and scattering length as a function of the wavelength of light (a) and phase and group index of refraction (b) in seawater. Adapted from [68].

2.5 Detection signatures

The neutrino interaction products and their light yield result in two main detection signatures:

- Track: muons from ν_μ CC interactions and ν_τ CC interactions where the τ decays into a muon,
- Shower: hadronic showers from all-flavour NC interactions, electromagnetic showers from ν_e CC interactions and ν_τ CC interactions where the τ decays either into an electron or into hadrons.

The key difference is the presence of a relativistic muon that travels substantial distances while emitting light. The electrons and hadrons that produce electromagnetic and

hadronic showers deposit all their energy in a relatively small region of space. An overview of the detection signatures is shown in Figure 2.5.

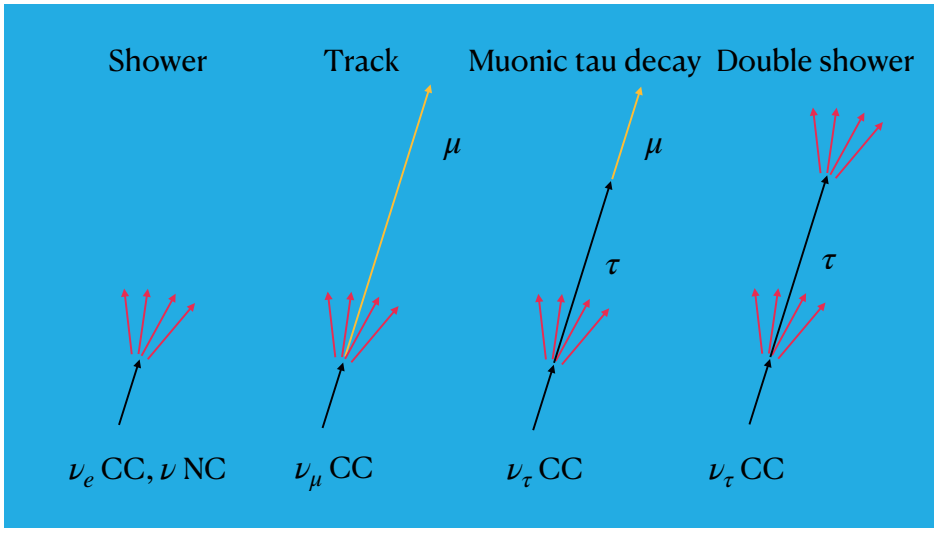

Figure 2.5: Detection signatures from high-energy neutrino interactions in water.

The ν_τ CC interaction channel can also be divided into the following categories for detection:

- Double bang or double shower: ν_τ CC interactions where the τ decays either into an electron or into hadrons,
- Muonic tau decay: ν_τ CC interactions where the τ decays into a muon.

The sum of the branching ratios of the tau lepton decaying into an electron or hadrons is 82.6% and this is seen as the most promising channel for the detection and identification of ν_τ. This channel distinguishes itself from single showers at high-energies when the tau range increases. This results in two separate showers that could be distinguished from single showers from ν NC and ν_e CC interactions. The final chapter of this thesis covers the reconstruction of double shower events, enabling their application in neutrino astronomy. The identification of muonic tau decay events is significantly more challenging due to the similarities with events with a muon that are produced in ν_μ CC interactions.

Chapter 3

The KM3NeT/ARCA detector

The light that is induced by the neutrino interaction products described in the previous chapter is detected by the Cubic Kilometre Neutrino Telescope (KM3NeT), which is currently under construction at the bottom of the Mediterranean Sea [69]. The research infrastructure hosts two deep seawater neutrino telescopes: ARCA (Astroparticle Research with Cosmics in the Abyss) and ORCA (Oscillation Research with Cosmics in the Abyss). They use the same technology and detection principle, though their size and primary scientific objectives are different.

The ARCA detector is currently under construction at a depth of 3500 m, offshore Capo Passero, Sicily, Italy. Its primary purpose is to detect neutrinos with energies beyond a TeV with the aim of doing neutrino astronomy. The ARCA field of view for upgoing neutrinos covers mainly the Southern sky, enabling the study of potential Galactic sources. Upgoing neutrinos are promising in neutrino astronomy due to the shielding of the Earth against muons from air showers in the atmosphere induced by cosmic rays. The first scientific results from ARCA, obtained with partial detector configurations, have been presented in References [70–72]. These analyses included up to 21 active detection units, out of the total of 230 that are planned. Once fully deployed, these units will collectively instrument a total volume of approximately 1 km^3.

The ORCA detector, under construction at a depth of 2500 m off the coast of Toulon, France, is specifically designed for low-energy neutrino detection. It aims to determine the mass ordering of neutrinos through the study of oscillations of atmospheric neutrinos.

3.1 Detector overview

Both detectors consist of a grid of optical modules that detect Cherenkov radiation using photomultiplier tubes [73]. The optical modules are mounted along vertical strings, which are placed on the seafloor as shown schematically in Figure 3.1. The average horizontal spacing between strings for the ARCA detector is 90 m and the vertical spacing between optical modules is 36 m. The spacing of the ORCA detector is smaller to target lower neutrino energies, maintaining an average horizontal spacing of 20 m and a vertical spacing of 9 m. The following sections cover the key KM3NeT detector components, followed by a description of the optical background sources, the data acquisition system and calibration efforts.

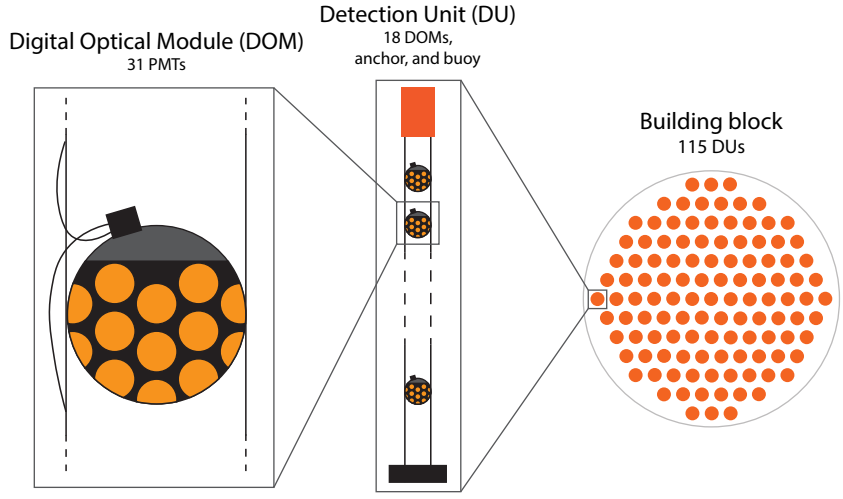

Figure 3.1: The KM3NeT detector layout. The full ARCA detector will have two building blocks of 115 detection units each. The ORCA detector will comprise a single building block.

3.2 Photomultiplier tube

Photomultiplier tubes (PMTs) are devices that convert light into an electrical signal [74]. When light hits a photocathode, it can free an electron due to the photo-electric effect. The probability for this process is given by the quantum efficiency, which is wavelength dependent. The produced photo-electron is then accelerated using a focusing electrode towards the electron multiplier. The electron multiplier consists of a series of dynodes with increasing potential. The electrons are multiplied due to secondary emission on the dynodes until they reach the anode. The signal from a photon can then be measured as an electrical pulse. A schematic overview of a PMT is shown in Figure 3.2.

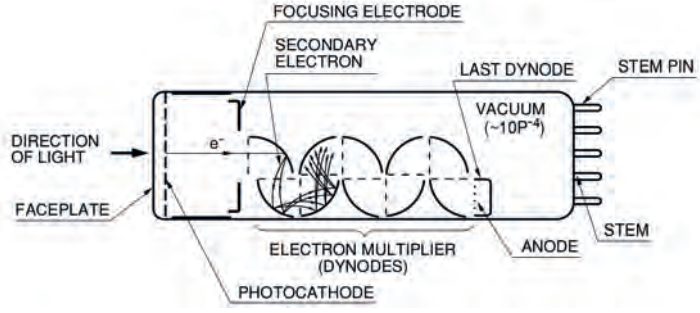

Figure 3.2: Schematic overview of a PMT. Adapted from [75].

For the initial phase of the KM3NeT detector, the Hamamatsu R12199-02 PMT has been selected as the photodetector [76]. This is an 80-mm diameter hemispherical PMT featuring 10 dynode stages and a standard bi-alkali photocathode, and is shown in Figure

3.3a. The quantum efficiency is defined as the probability for a photon to generate a photo-electron and it is shown in Figure 3.3b.

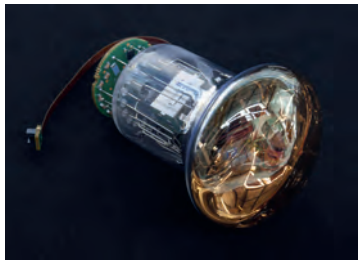

(a)

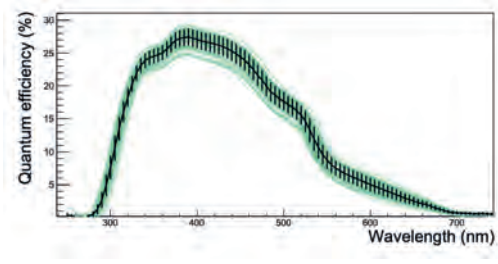

(b)

Figure 3.3: The Hamamatsu R12199-02 photomultiplier tube and base (a). The quantum efficiency of the Hamamatsu R12199-02 PMT (b). Adapted from [76].

A customised base is mounted to each PMT which consists of a current amplifier and a settable threshold discriminator. The threshold discriminator converts the analogue signal to a signal indicating whether the voltage is over threshold, which is shown in Figure 3.4a. The threshold is set at a value corresponding to 0.3 single photo-electrons and this allows for the detection of a large fraction of single photon electrons while being well separated from the noise. Light detections are digitised on the central logic board of an optical module into a *hit* which contains two variables:

- t: time at which the signal surpassed the threshold,
- ToT: total time that the signal was above the threshold.

The central logic board of the optical module is discussed in the following section.

The PMTs are supplied with high voltage in order to achieve the desired gain of the signal. The gain of a PMT refers to the factor by which it multiplies the initial photo-electron. KM3NeT targets a PMT gain of 3×10^6, but achieving this requires different high voltage levels due to the partly handmade nature of Hamamatsu PMTs, which leads to variability in gains at the same voltage. To standardise gains across all PMTs, KM3NeT utilises the relationship between the ToT distribution and gain. Figure 3.4b illustrates a typical ToT distribution for single photo-electrons from a KM3NeT PMT, with a peak at 26.4 ns which corresponds to the desired gain of 3×10^6.

The transit time is defined as the time it takes to detect a signal after a photon hits the PMT. The photon has to free a photo-electron that has to be multiplied by the dynodes before the signal is detected. The variation in transit times after photons hitting the photocathode is explained by the Poisson nature of the multiplication of electrons and the various paths a photo-electron can travel towards the first dynode. The spread of the transit time is a measure of the timing accuracy of a PMT and is measured at 1.5-3 ns [73]. The average dark count rate is measured at 1.3 kHz.

The PMTs are purchased in steps and this offers the possibility to profit from industrial performance improvements by selecting new PMT models. The model adopted for later batches is the Hamamatsu R14374 which has an improved transit time spread. A publication on the characterisation of this new PMT is in preparation.

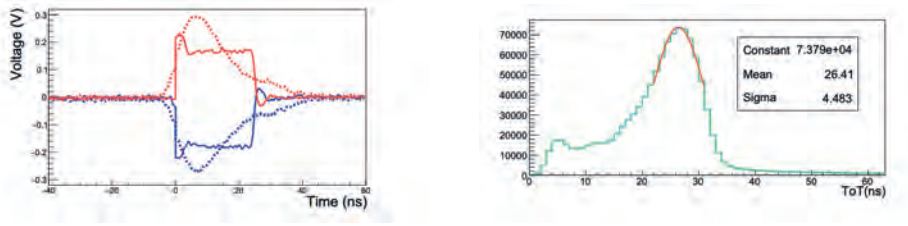

(a) (b)

Figure 3.4: Conversion of the analogue (dashed) signal to ToT (solid) using the PMT base (a). The colours represent the positive (red) and negative (blue) component of the differential signal. Typical distribution of the ToT (b). The peak is modelled using a Gaussian function centered at 26.4 ns. Adapted from [76].

3.3 Digital optical module

The main detector component of the KM3NeT experiment is the digital optical module (DOM) [73] and is shown in Figure 3.5. The DOM consists of a 44 cm diameter glass sphere housing 31 PMTs that were discussed in the previous section. The orientation of the PMTs results in an almost isotropic coverage for photons coming from below up to an angle of 32° with the top. The PMTs are surrounded by reflector rings that increase the acceptance by 20-40% and are mounted to a support structure. The structure supports the 31 PMTs and their reflector rings and a pressure gauge. The structure traps silicone gel in the spaces between the PMTs and the glass. The gel ensures optical contact between the water, glass and PMTs. The top hemisphere is perforated such that two copper wires and an optical fiber can be connected for providing power and sending and receiving data. The glass sphere is wrapped by a titanium collar so that it can be mounted to a detection unit, which is described in the next section.

Both hemispheres of a DOM have a signal collection board that pass the PMT signals to the central logic board. The central logic board is the brain of the optical module which processes the data from the PMTs and transmits it to shore. Sub-ns time synchronisation is achieved via optical Ethernet communication and the White-Rabbit protocol [77]. Additionally, the central logic board operates an acoustic piezo sensor, a LED beacon, a humidity sensor, several temperature sensors, a compass and a tiltmeter. These devices are used for monitoring and calibration tasks.

3.4 Detection unit

The detection unit is the structure that organises 18 DOMs in a vertical configuration and facilitates their connection to the optical and electrical network on the seafloor via optical fibers and copper wires [78]. A detection unit is commonly referred to as a (detection) string. The cables are housed in a flexible polyethylene tube filled with oil, which ensures a pressure balanced system. The detection unit is anchored at the seafloor and kept vertical due to the buoyancy of the DOMs and the buoy attached to the top. Two Dyneema® ropes form the mechanical structure that withstands the buoyancy force. The detection units are grouped in building blocks, each comprising 115 detection units. A schematic

Figure 3.5: The KM3NeT digital optical module.

view of this configuration is shown in Figure 3.1. The ARCA detector will consist of two building blocks and the ORCA detector will have one building block.

3.5 Optical background sources

The most substantial background in neutrino telescopes originates from cosmic rays interacting with the atmosphere and producing air showers. Many of the muons coming from the decay of short-lived particles in the air shower reach the surface of the Earth, and high-energy muons can even reach the detector depth of 3.5 km. One of the first KM3NeT data analyses shows the depth dependence of the muon rate in Reference [79].

An important background source in seawater is the decay of ^{40}K [69]. It decays mainly into ^{40}Ca while releasing an electron and an antineutrino. These electrons can emit Cherenkov radiation and they provide a constant background signal in the detector. The maximum energy of the electron is 1.31 MeV and this signal is used for the calibration of the detector. The typical rate at the sea bottom is $6 - 8$ kHz per PMT and this includes the dark count rate.

Another source of background comes from bioluminescent organisms [69]. They emit bursts of light lasting for a few seconds and the occurrence is correlated with the sea current. This is likely due to water turbulence and the collision of organisms with the DOMs. The rates can reach up to several MHz in the Mediterranean Sea.

The background from ^{40}K and bioluminescent organisms can be disentangled from the neutrino signals using the data filters. Relativistic particles cause patterns of light over larger distances that are not produced by ^{40}K or bioluminescent organisms. The background has time-position correlations between PMTs on the same DOM, while the neutrino signals

are correlated between DOMs.

3.6 Data acquisition

Data acquisition is based on an *all-data-to-shore* concept. In this, all recorded hits are transmitted to shore. These hits are called L0 hits and they are grouped together in time windows of 100 ms. The data is sent to shore via an Ethernet network through optical fibers and processed in real time.

The L0 hits are filtered by selecting coincident hits on different PMTs in the same DOM within 10 ns, resulting in a L1 hit. The filter also selects L1 hits on the PMTs of a DOM that fall within a specified angular distance, and these are identified as L2 hits. The maximum angular distance between hit PMTs is currently set at 180°, but this can be reduced in the future to reduce contamination from background hits.

Data are filtered using trigger algorithms which select subsets of hits, commonly referred to as an event, consistent with a relativistic particle crossing the detector. Several trigger algorithms run parallel on the L2 data to search for products from neutrino interactions. All hits within a predefined time window around an event are written to disk when the criteria are met. This window is set at 3.8 μs for the ARCA detector configuration with 21 detection units, and matches the time required for light to traverse the longest path within the detector. The full detector simulations utilise 5.7 μs. The following algorithms are currently in place [80]:

3DShower. This algorithm searches for pairs (ij) of correlated L2 hits that fulfil

$$|t_i - t_j| \leq |x_i - x_j| \frac{n}{c}, \tag{3.1}$$

where t is the hit time, x the position of the PMT, n the refractive index of seawater and c the speed of light in vacuum. The ARCA detector with 21 detection units selects events after finding at least 5 causally correlated hits in a sphere with a radius of 250 m.

3DMuon. The muon trigger algorithm searches for pairs of correlated hits that fulfil the Cherenkov hypothesis using different muon direction hypotheses. The Cherenkov condition is described as

$$|(t_i - t_j)c - (z_i - z_j)| \leq \sqrt{(x_i - x_j)^2 + (y_i - y_j)^2} \tan\theta_c \tag{3.2}$$

where x, y, z represent the position of the PMT and θ_c the Cherenkov angle in seawater. The algorithm selects events with at least 5 causally correlated hits within a cylinder with a radius of 120 m and a length which spans the full operational detector.

MXShower. This algorithm searches for a combination of track and shower hits that are causally correlated, and is most efficient at low energies where the topologies are more similar. Events are selected based on a minimum of 8 hits within a sphere or cylinder, similar to the selection criteria used for 3DShower and 3DMuon.

Additionally to the optical data, calibration data is stored in order to reconstruct the varying positions and orientations of each optical module due to the sea currents. The average PMT rates are stored as well and can be used to mimic the actual background rates of the detector during a data collection period for the simulations.

3.7 Calibration

To fulfill the physics objectives of ARCA it is essential to conduct precise calibrations of the detector and to measure the environmental conditions affecting the detector operation. To achieve the envisaged pointing resolution below 0.1° for tracks, the positions and orientations of the DOMs should be measured with a resolution of 20 cm and 3° respectively and the time offsets of the PMTs with 1 ns accuracy.

The optical background sources at the bottom of the Mediterranean Sea can be exploited for calibration purposes. The efficiencies of the PMTs are monitored using the ^{40}K decays in the seawater, alongside time offsets between PMTs within a DOM [81]. Time offsets between DOMs and detection units can be determined using the LED beacons and by exploiting the signals from downgoing atmospheric muon events [82]. Calibration efforts using the operational detection units have achieved the desired timing accuracy as shown in Reference [83, 84].

DOM positions and orientations vary due to the sea currents. Relative DOM positions are calibrated using acoustic signals. Acoustic signals from various acoustic beacons are detected by the piezos in each DOM and are used for the reconstruction of their relative positions [85]. The detection unit is described by a mechanical model which includes the buoyancy of the modules and contains a tilt angle with respect to a vertical string. The measured tilt angles are used to reconstruct the relative positions of the optical modules. The reconstructed tilt angles as a function of time are shown in Figure 3.6 for 21 detection units of ARCA. The maximum tilt angle in the figure corresponds to a maximum horizontal displacement of several tens of meters at the top of string. The orientation of the modules is determined using the compasses integrated in the DOMs.

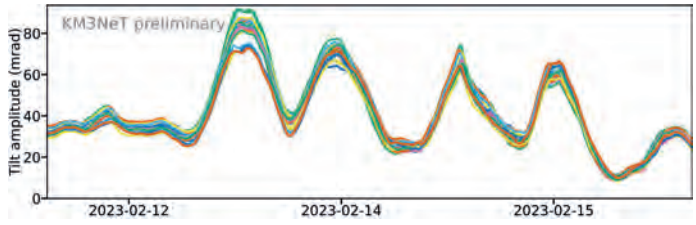

(a)

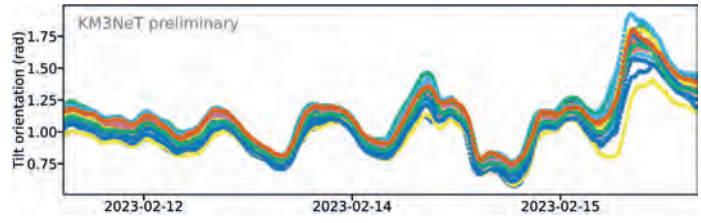

(b)

Figure 3.6: Amplitude of the tilt (a) and tilt orientation (b) for a few days of the ARCA detector with 21 detection units. Adapted from [85].

The calibration of the absolute pointing of the detector is crucial for doing neutrino astronomy. This can be achieved by obtaining the absolute positions of the optical modules.

This measurement is scheduled after a sea operation in September 2024, where the absolute positions of the acoustic emitters will be established. The absolute positions of the optical modules follow from the procedure described above.

The cosmic ray shadow from the Sun and Moon causes a deficit in the number of detected atmospheric muons from their respective positions in the sky. This phenomenon is shown in Figure 3.7. The deficit of muons can be used to verify the absolute pointing of the detector. This analysis was performed using data obtained with 6 strings of ORCA [86], and is currently carried out for ARCA.

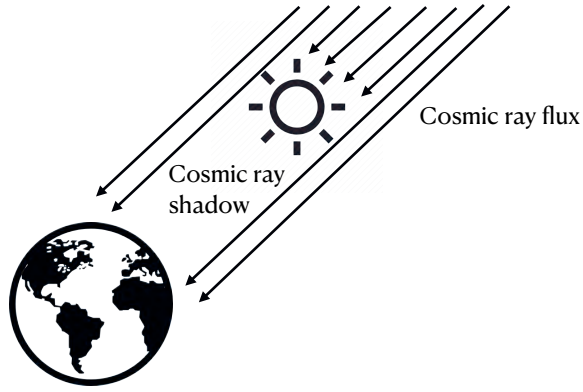

Figure 3.7: The cosmic ray shadow due to the Sun.

3.8 Current status of the detector

The research presented in this thesis was conducted using the ARCA detector. At the time of writing this thesis (spring 2024), the ARCA detector operates 28 of the planned 230 detection units. The installation of an additional 20 detection units is scheduled for the late summer of 2024. The analyses in this thesis cover data taken from May 2021 until December 2022. This period contains data taken with 6, 8, 19 and 21 detection units, which is denoted as ARCA6-21 and is further described in Chapter 6. Furthermore, the sensitivity studies for the full detector are covered and this simulated dataset is denoted as ARCA or ARCA230 and is covered in Chapter 5.

Chapter 4

Simulation and reconstruction

Monte Carlo simulations are an essential tool to compute the acceptance and the resolution of a neutrino telescope. The simulation procedure can be subdivided into several steps, for which the KM3NeT collaboration has developed dedicated software packages, each briefly outlined in the following sections.

4.1 Event generation

The volume around the detector which is used to simulate neutrino interactions is called the generation volume. This volume covers the region in which neutrino interactions are simulated. The size of this volume varies depending on the neutrino interaction because some secondary particles can travel large distances and reach the detector producing a detectable signal.

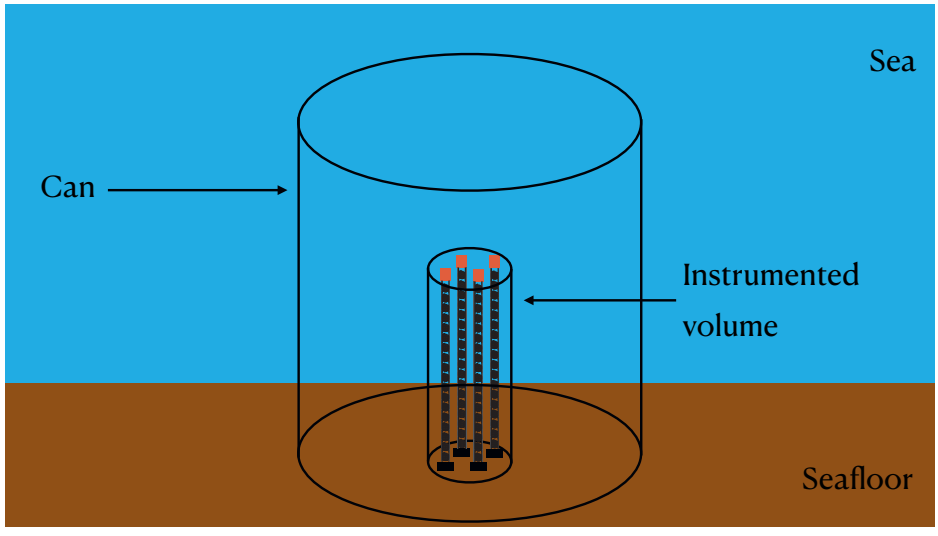

Figure 4.1: Overview of the instrumented volume and the can in which light is simulated.

The *can* is the region around the detector in which light is simulated. This volume is a cylinder surrounding the instrumented volume of the detector. The radius and height

of the instrumented volume is extended with an additional four light absorption lengths within water. The can does not include the seafloor and reaches to a kilometer above it. The can radius for the ARCA21 detector is approximately 600 m, while it extends to 900 m for a complete building block.

Neutrino interactions resulting in a shower (ν_e CC, ν NC) have a generation volume that corresponds to the can, as all emitted light from the neutrino interaction occurs within a few meters of the interaction point. In interactions leading to the production of a μ or τ lepton, the generation volume is significantly larger than the can and varies with the energy of the neutrino. An overview of the instrumented volume and the can is shown in Figure 4.1.

4.1.1 Neutrinos

Neutrino interactions are simulated using the gSeaGen simulation framework [87]. All interaction channels of neutrinos of all flavours are simulated over an energy range spanning from 10^2 to 10^8 GeV, alongside the propagation of the charged leptons to the can surface. The framework simulates neutrino interactions from resonant interactions, quasi-elastic scattering and deep inelastic scattering, with the latter being dominant at these energy levels [88]. The transmission of neutrinos through the Earth is computed, taking into account the Earth's density profile based on the PREM model as described in Reference [89].

The generated neutrino events follow a single power law spectrum $E^{-\gamma}$ with a spectral index of $\gamma = 1.4$. The simulated neutrino events are weighted according to different flux models for neutrinos of atmospheric and cosmic origin, in order to estimate their rate at the detector. The events are weighted using a neutrino flux model, the interaction cross section, the transmission probability in the Earth and normalisation constants as described in Reference [87].

As described in Section 1.3.5, the atmospheric neutrino flux consists of a conventional and a prompt contribution. The conventional contribution arises from the decay of light and long-lived mesons, such as charged pions and kaons, and dominates the flux composition up to 10-100 TeV. The prompt contribution comes from the decay of heavier and short-lived hadrons and is expected to have a harder energy spectrum than the conventional flux. In this work, the conventional component is represented by the 2006 flux model from *Honda et al.* [90]. The prompt component is taken from *Enberg et al.* [37]. Both contributions are corrected to account for the knee in the cosmic spectrum as described in Chapter 1. The correction is based on the H3a composition model [21].

4.1.2 Atmospheric muons

The interaction of cosmic rays with the atmosphere produces a large number of high-energy muons from charged pion decays that reach the depth of the detector. The atmospheric muons are simulated with the MUPAGE software package [91], which uses the rate of muons at a given zenith angle and depth under sea or in ice by means of parametric formulas. The parametric formulas have been obtained from Monte Carlo simulations of cosmic ray showers and their propagation. The muons from cosmic ray air showers can reach the detector alone or in bundles. In addition to the zenith angle and depth dependence, the simulation of muons in a bundle depends on the number of muons in

the bundle and the radial distance to the axis of the bundle. Atmospheric muon events are created by generating muons at the edge of the can where the properties are sampled from the parametric formulas.

The bundle energy threshold is an input parameter that is utilised to set a lower bound on the simulated muon energies. Simulations for the current ARCA detector use a bundle energy threshold of 100 GeV. The simulations for the full detector gave priority to high-energy atmospheric muons which may pass the event selections. Two samples were simulated with a threshold at 10 TeV and 50 TeV. It was checked that lower-energy muons have no significant impact on the analysis presented in this thesis.

4.2 Particle propagation and light simulation

The generated events are processed by an internal KM3NeT software package called *JSirene* that simulates the particle propagation, including the energy loss and the production of Cherenkov photons in water. The simulation of light from charged particles is based on probability density functions (PDFs) describing the arrival time of photons [92]. The PDFs contain probabilities for the arrival time of photons as a function of the energy of the particle, of the distance of a PMT from the particle trajectory, and of the incidence angle of light on the PMT.

The description of light emitted by muons accounts for minimum ionising particles, δ-rays, and bremsstrahlung showers emitted along the muon track. Bremsstrahlung and pair production from electrons are simulated as an electromagnetic shower. Hadrons are assumed to produce similar light patterns as electromagnetic showers. Tau leptons are treated as minimum ionising particles producing δ-rays along their trajectory.

Dispersion, absorption and scattering effects of photons are taken into account to describe the transmission of light. JSirene simplifies the process of photon scattering by focusing solely on single scattering of photons, which is solved analytically. The information on simulated photo-electrons is stored after convolving the light yield from the processes described above with the angular acceptance and the quantum efficiency of the PMTs.

4.3 Detector-response

The information on the detected photo-electrons is used as input for the *JTriggerEfficiency* software package dedicated to describe the response of the KM3NeT detector. This software simulates the PMT response to light, the front-end electronics, and random optical backgrounds. The detection times of the simulated photo-electrons from the previous simulation step are obtained by sampling transit-time distributions of the KM3NeT PMTs [9]. A model is employed to describe the relationship between the deposited charge and the number of detected photons, and this relationship may vary for each individual PMT. The simulations in the following chapters cover two basic categories. One set of simulations covers the future detector and employs a PMT with nominal parameters and a ^{40}K rate of single coincidences of 7 kHz. The other set of simulations is based on a *run-by-run* approach and mimics the background rates and PMT parameters during a data-taking run. The simulated data stream is represented by a collection of hits that are in the same format as in the data coming from the sea.

The algorithm determines whether an event is stored by applying event triggering conditions on the simulated hits, which were outlined in Section 3.6. Identical trigger conditions are applied to the simulations as well as to the data and the resulting events are input to the reconstruction algorithms for tracks and showers described in the following sections.

4.4 Reconstruction

Event reconstruction algorithms are used to extract the physical event properties from data that will be used in the search for cosmic neutrinos. The KM3NeT algorithms used here are based on maximum likelihood search methods focused on track-like signatures from muons and shower-like signatures from electromagnetic and hadronic showers.

4.4.1 Track reconstruction

Using track reconstruction algorithms, the energy (E_μ), the direction ($\vec{d}_\mu$) and the position ($\vec{x}_\mu$) at a given time (t_μ) of the trajectory of a muon are determined from the hits [93]. The PDF of the arrival time of Cherenkov light [92] from a muon is a function of the following five parameters denoted as $\bar{x}$:

- R: minimum distance between the muon path and the PMT,
- θ, ϕ: PMT orientation angles with respect to the track direction,
- Δt: difference between measured and expected hit time according to the Cherenkov hypothesis,
- E_μ: energy of the muon.

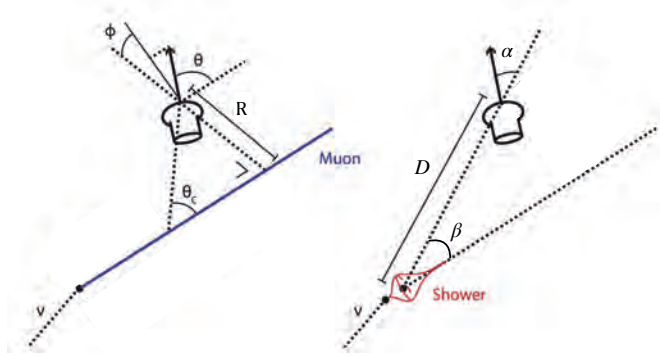

Figure 4.2: Overview of a PMT with a muon track (a) or a shower (b).

A sketch of the configuration is shown in Figure 4.2a. The number of photo-electrons as a function of R and Δt is shown in Figure 4.3. The time dependence is shown for a PMT facing the muon track and for a PMT looking away. The number of photo-electrons scales linearly with the energy of the muon.

The first step of the procedure involves a direction prefit, which explores a predefined set of 20,000 directions covering the full sky. In each direction, the position and the time of

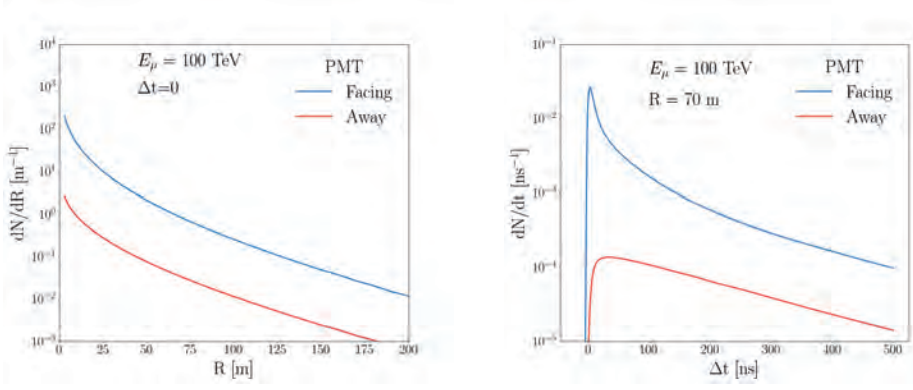

(a) (b)

Figure 4.3: Number of photo-electrons as a function of the minimum distance between the muon path and a PMT (a) and the difference between the measured and expected hit time (b). These quantities are shown for a PMT facing the muon track, and for a PMT looking away from the muon track.

the muon need to be determined. The prefit neglects scattering and dispersion of light, which allows to write an expression for the expected hit time t_i for light emitted at the Cherenkov angle. This expected and the measured hit time are used to find the optimal $\vec{x}_\mu$ and t_μ when considering a direction hypothesis. To maximise the probability that the right solution is maintained whilst limiting the CPU time, a selection of the best prefit solutions are passed to the next step.

The subsequent steps maximise a likelihood function using the hits on all PMTs within a cylinder with a radius of 150 m around the previously found muon track hypotheses. The direction and vertex are estimated using the following likelihood

$$\mathcal{L}^{\mathrm{S+B}} = \sum_{\text{1st hits}} P_{\mathrm{1st}}^{\mathrm{S+B}}(\bar{x}), \tag{4.1}$$

where $P_{\mathrm{1st}}^{\mathrm{S+B}}(\bar{x})$ is the probability density function of the first hit time for signal and background. As outlined in the detector chapter, the detector only provides accurate timing information on the first hit on a PMT. Two photons closely spaced in time will be combined into one hit with the time of the first hit and with an increased time-over-threshold (ToT). The expression in Equation 4.1 is a multiplication of the Poisson probability to register no hit up until time Δt and the detection rate at time Δt. The first hit rate from a muon is defined as

$$n_{\mathrm{1st}}(\bar{x})^{\mathrm{S}} = \exp[-N(\bar{x}, \Delta t)]\Big(n(\bar{x}, \Delta t)\Big). \tag{4.2}$$

where $n(\bar{x}, \Delta t)$ is the rate of photo-electrons at time Δt due to the muon and $N(\bar{x}, \Delta t)$ the total number of photo-electrons up until Δt. This expression has to be normalised in order to obtain the probability density function of the first hit time. The first hit rate is integrated over time

$$\int_{\Delta t_{\min}}^{\Delta t_{\max}} n_{\mathrm{1st}}(\bar{x})^{\mathrm{S}} dt = 1 - \exp[-N(\bar{x}, \Delta t_{\max})], \tag{4.3}$$

where $N(\bar{x}, \Delta t_{\max})$ covers all signal hits in time window $\Delta t_{\max} - \Delta t_{\min}$. This leads to the definition of the probability density function of the first hit time for signal and background:

$$P_{1\text{st}}(\bar{x})^{\text{S+B}} = \frac{\exp[-N(\bar{x}, \Delta t) - R_{bg}(\Delta t - \Delta t_{\min})]\Big(n(\bar{x}, \Delta t) + R_{bg}\Big)}{\alpha}, \tag{4.4}$$

$$\alpha = 1 - \exp[-N(\bar{x}, \Delta t_{\max}) - R_{bg}(\Delta t_{\max} - \Delta t_{\min})], \tag{4.5}$$

where R_{bg} is the background rate. The typical window for the ARCA detector spans from -50 to 450 ns. It's important to note that the absolute time window of all hits extends beyond 500 ns. The detected hits must not occur earlier than 50 ns or later than 450 ns relative to the anticipated hit time of a photon emitted at the Cherenkov angle from the muon track.

The likelihood function of Equation 4.1 is combined with the likelihood for background only and taking the logarithm to obtain

$$\lambda = \ln \frac{\mathcal{L}^{\text{B}}}{\mathcal{L}^{\text{S+B}}}. \tag{4.6}$$

The minimum of λ corresponds to the track direction and vertex hypothesis that is most compatible with the signal hypothesis. This minimum is found iteratively and the corresponding track parameters are stored alongside the fit quality. The fit quality is defined as $L_{\text{track}} = -\lambda$ to ensure that higher values correspond to a better fit.

The final step of the procedure estimates the energy of the muon. The expected number of photo-electrons from a muon trajectory hypothesis can be used to calculate the likelihood that PMT i registers no hit:

$$P_i^{\text{no hit}} = \exp\Big[- N(\bar{x}, t_{\max}) - R_{\text{bg}}(\Delta t_{\max} - \Delta t_{\min})\Big], \tag{4.7}$$

and the likelihood that the PMT detects one or more hits:

$$P_i^{\text{hit}} = 1 - P_i^{\text{no hit}}. \tag{4.8}$$

The muon energy is determined by maximising the following likelihood function

$$\log \mathcal{L}(E_\mu) = \sum_{i \in \text{hits}} \log\big(P_i^{\text{hit}}\big) + \sum_{i \in \text{no hit PMTs}} \log\big(P_i^{\text{no hit}}\big), \tag{4.9}$$

while varying the muon energy E_μ.

Performance

The direction and energy reconstruction are important in the study of cosmic neutrinos. The direction resolution is expressed in angular deviation ψ, which is the angle between the true direction of the neutrino and the reconstructed direction. The median and 68% percentiles for simulated ν_μ CC events using the full ARCA detector are shown in Figure 4.4a. The energy error is defined as

$$\text{Energy error} = 100\% \times \Big(\frac{E_{\text{rec}}}{E_{\text{vis}}} - 1\Big), \tag{4.10}$$

where E_{rec} is the reconstructed energy and E_{vis} is the visible energy. The visible energy is defined as the sum of the energies of the secondary particles that produce light in the detector. The energy error with the corresponding median and 68% percentiles are shown in Figure 4.4b. The difference of the median energy error with respect to 0 is commonly referred to as the energy bias. The energy resolution is defined as half the difference between the 68% quantiles of the energy error. Both distributions show events that pass preliminary analysis selection criteria based on the fit quality: $L_{\text{track}} > 50$, and the number of hits used in the reconstruction: $N_{\text{track}}^{\text{hits}} > 20$. The resolutions improve when applying more elaborate selection requirements, as seen in Chapter 5.

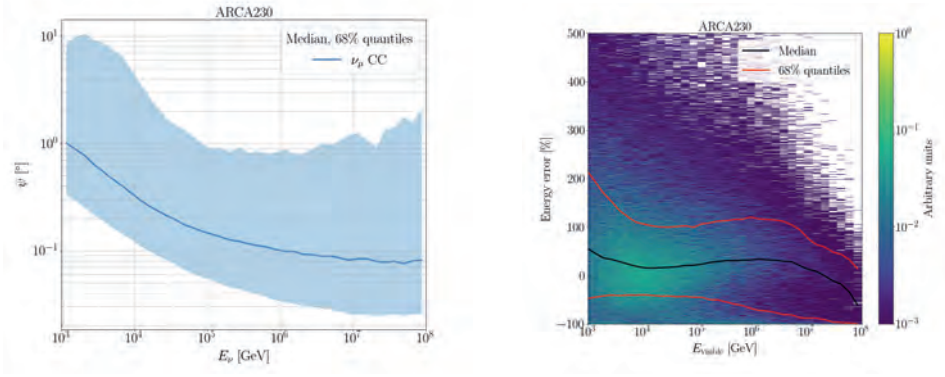

(a) (b)

Figure 4.4: Angular deviation (a) and energy error (b) of the track reconstruction for simulated ν_μ CC events with $L_{\text{track}} > 50$ and $N_{\text{track}}^{\text{hits}} > 20$ using full ARCA.

4.4.2 Shower reconstruction

ARCA utilises the Aashowerfit algorithm for shower reconstruction, employing a two-step procedure [93]. The first step estimates the shower maximum position ($\vec{x}_s$) and time (t_s) using coincident hits. The shower maximum refers to the point along the path of a high-energy particle shower where the number of secondary particles and light reaches its maximum value. Hits are selected if a DOM registered at least two hits within a time window of 20 ns on the same optical module. The position and time are found by minimising the function

$$M(\vec{x}_s, t_s) = \sum_{i \in \text{hits}} \sqrt{(1\text{ ns})^2 + (t_i - \hat{t}_i)^2}, \tag{4.11}$$

where t_i is the measured hit time and $\hat{t}_i$ the expected hit time. Particle showers emit light across several meters, yet their elongation is small with respect to the spacing of the instrument. For this reason, the expected hit time can be calculated assuming a spherical light pattern emitted from the shower maximum according to

$$\hat{t}_i = t_s + \frac{d}{v_{\text{group}}}, \tag{4.12}$$

where d is the distance from the PMT to the shower maximum and v_{group} is the group velocity of light in water.

The final fit tests different direction hypotheses, where the estimated vertex position of the first step acts as a pivot. Twelve isotropic starting directions are chosen for which the following likelihood is maximised

$$\log \mathcal{L}(E_{\text{shower}}, \vec{d}_{\text{shower}}) = \sum_{i \in \text{hit PMTs}} \log\big(P_i^{\text{hit}}\big) + \sum_{i \in \text{no hit PMTs}} \log\big(P_i^{\text{no hit}}\big), \tag{4.13}$$

where

$$P_i^{\text{hit}} = 1 - P_i^{\text{no hit}} = 1 - \exp\Big[- \mu_{\text{s}}(D_i, \beta_i, a_i, E_e) - R_{\text{bg}}(\Delta t_{\text{max}} - \Delta t_{\text{min}})\Big]. \tag{4.14}$$

Hits are selected within a window of $\Delta t_{\text{max}} - \Delta t_{\text{min}}$. The typical time window for the ARCA detector spans from -50 to 950 ns. The significant extension towards positive values allows for the inclusion of a large fraction of the scattered and consequently delayed signal hits, but it also results in the inclusion of more background hits. Optimisation of this window is yet to be conducted.

The expected number of hits μ_{s} from a shower is obtained from a distinct table compared to the track reconstruction and is generated through Monte Carlo simulations of electromagnetic showers. The expected number of hits depends on the following parameters:

- D: the distance from the vertex to the PMT;
- β: the angle between the shower direction and the vector between the vertex and the PMT;
- α: the angle between the normal vector of the PMT and the vector between the vertex and the PMT;
- E_e: the energy of the initial electron;

A depiction of a shower and PMT can be seen in Figure 4.2b. The expected number of signal hits as a function of the previously mentioned parameters are shown in Figure 4.5. In contrast to track reconstruction, the shower reconstruction doesn't utilise the hit time information for estimating the shower direction. As illustrated in Figure 4.5b, the majority of light is emitted at the Cherenkov angle ($\theta_c = 42.4°, \cos(\theta_c) = 0.75$), aiding in the estimation of the shower direction.

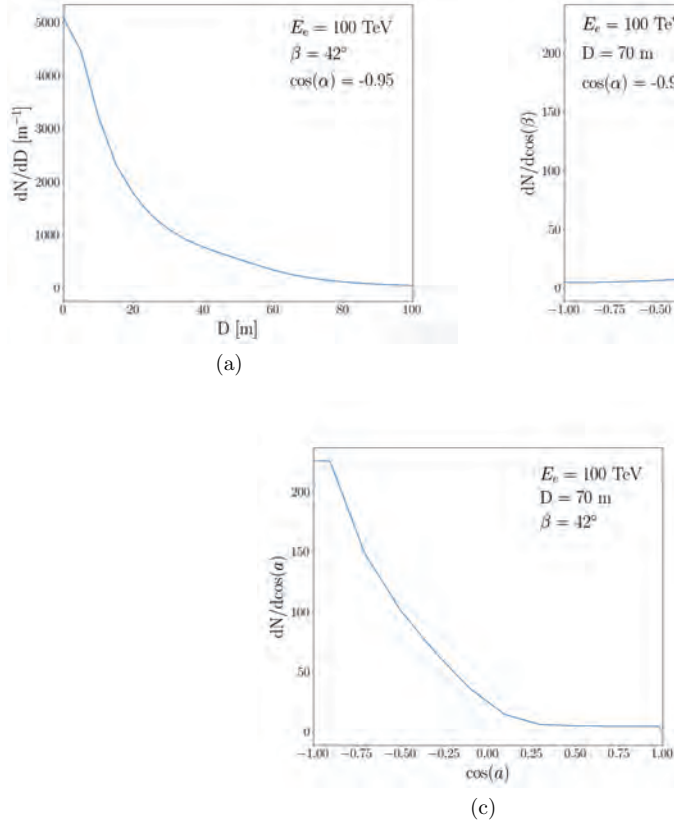

Figure 4.5: The expected number of hits from an electromagnetic shower as a function of the distance D from the vertex to the PMT (a), the cosine of the angle β between the shower direction and the vector between the vertex and the PMT (b) and the cosine of the angle α between the normal vector of the PMT and the vector between the vertex and the PMT (c).

Performance

The performance of the vertex reconstruction can be broken down into longitudinal and perpendicular components with respect to the neutrino direction. The perpendicular distance $D_\perp$ is the shortest distance between the reconstructed vertex and the shower axis. The longitudinal distance $D_\parallel$ is obtained after projecting the reconstructed vertex to the shower axis and calculating the distance to the vertex. Positive values indicate a reconstructed vertex in front of the shower, while negative values denote behind the shower. A depiction of both parameters is shown in Figure 4.6.

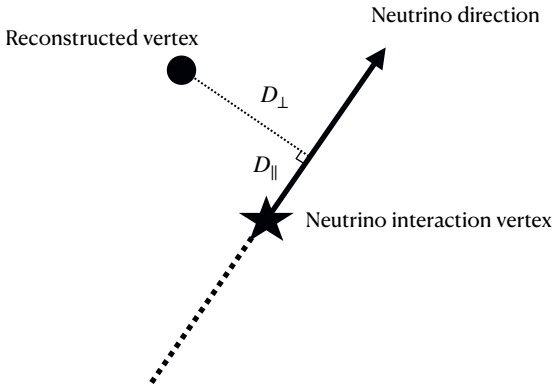

Figure 4.6: The longitudinal $D_\parallel$ and perpendicular $D_\perp$ distance with respect to the neutrino direction.

The position resolution for contained simulated ν_e CC events using the full ARCA detector is shown in Figure 4.7.

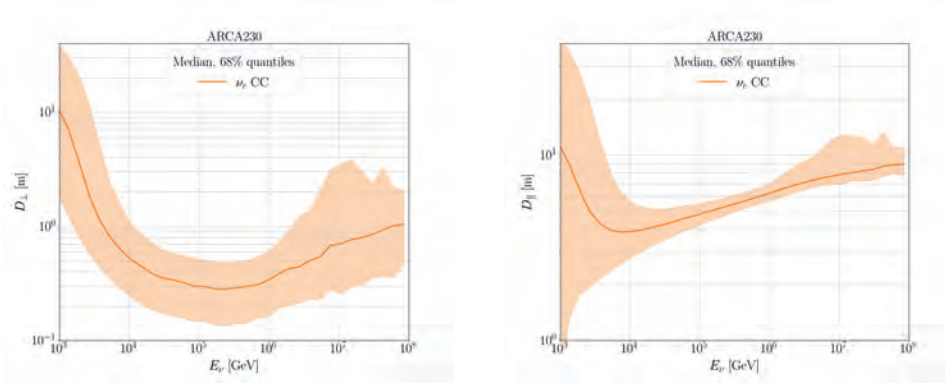

(a) (b)

Figure 4.7: Perpendicular (a) and longitudinal (b) vertex position resolution of the shower reconstruction for ν_e CC events with a contained neutrino interaction vertex using full ARCA.

The increase of $D_\parallel$ as a function of E_ν is explained by the vertex reconstruction assumption of point-like light emission. The algorithm finds the position where most light is emitted, which is not at the neutrino interaction vertex but at the shower maximum. When an electron interacts with the seawater, secondary particles are produced through pair production and bremsstrahlung. These secondary particles undergo similar interactions and the emitted Cherenkov light intensifies as can be seen in the longitudinal light emission profile of Figure 2.3. The distance from the position where the majority of light is emitted to the neutrino vertex increases with energy, as depicted in Figure 4.7b.

The angular deviation and energy resolution of contained simulated ν_e CC events using the full ARCA detector is shown in 4.8. The improved energy error and resolution for shower-like events with respect to tracks is attributed to the containment of the light, whereas the track reconstruction excels in the direction reconstruction due to the extensive distances tracks can travel within the detector.

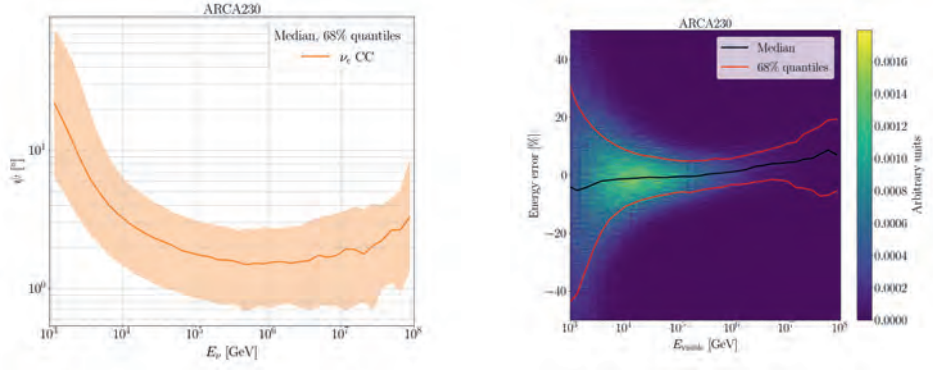

(a) (b)

Figure 4.8: Angular deviation (a) and energy error (b) of the shower reconstruction for simulated ν_e CC events with a contained neutrino interaction vertex using the full ARCA detector.

4.4.3 Shower reconstruction using timing information

The Aashowerfit reconstruction algorithm fits the direction of the shower without the inclusion of information on the hit times. The algorithm assumes that light is emitted from a fixed position and time, but high-energy showers are elongated over several meters as discussed in the previous section. A novel shower reconstruction algorithm was developed, featuring an enhanced shower model, as documented in Reference [94]. The longitudinal light emission profile of Figure 2.3 is used to account for the elongated shape of showers. The expected number of hits on a PMT due to an electromagnetic shower is sampled several times along the emission profile in order to calculate a weighted average. This requires a different PDF that includes the arrival time of light in order distinguish hits from different positions along the shower profile. The time dependence of the number of photo-electrons is shown in Figure 4.9.

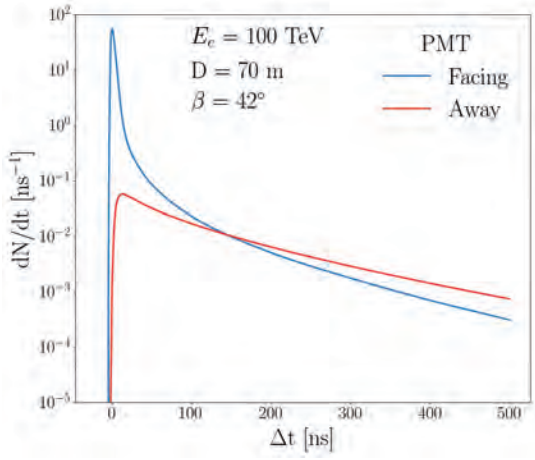

Figure 4.9: Number of photoelectrons as a function of the difference between the measured and expected hit time for an electromagnetic shower. These quantities are shown for a PMT facing the shower, and for a PMT looking away from the shower.

The direction reconstruction performance of Aashowerfit and the new algorithm which adopts the longitudinal shower profile and includes hit time information is shown in Figure 4.10. The improvement in performance is explained by the small lever-arm from the longitudinal profiles of the showers, enhancing the performance of direction reconstruction, similar to what is observed in reconstruction of track-like events.

The sensitivity studies described in the following chapters do not consider this new reconstruction algorithm because it is currently too computationally expensive to run over large datasets. Future efforts will focus on improving the speed of the algorithm. The algorithm could already be used to process a subset of the dataset that has been filtered through selection criteria to enhance the signal-to-background ratio and decrease the volume of events.

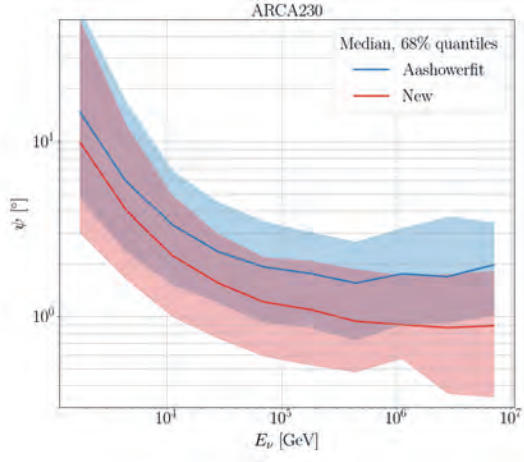

Figure 4.10: Angular deviation of the shower reconstruction for contained simulated ν_e CC events for Aashowerfit and the new algorithm which adopts the longitudinal shower profile and includes hit time information.

Chapter 5

Neutrino astronomy with full ARCA

Published in "Astronomy potential of KM3NeT/ARCA". Eur. Phys. J., vol. C84, no. 9, p. 885, 2024 [95].

This chapter builds upon the description of the event simulation and reconstruction presented in the previous chapter. Simulated datasets are used to study the potential of the full ARCA detector (230 strings, 2 building blocks) in doing neutrino astronomy. An event selection is applied to increase the ratio of signal and background events of the simulated dataset. This is followed by the development of detector-response functions that describe the performance of the detector to neutrino flux models. These functions are used as input for a statistical analysis to study the sensitivity and discovery potential of ARCA to neutrino point sources and an all-sky diffuse neutrino flux.

5.1 Event selection

The collected data from ARCA are dominated by events from environmental noise and the atmospheric muon background. Any possible neutrino source in the dataset is obscured by the abundance of background, and therefore selection criteria are applied to increase the neutrino purity. This is done separately for each of the two observation channels: tracks and showers. The selection criteria are based on the output from the track and shower reconstruction algorithms. The events passing these selection criteria are used to train a boosted decision tree (BDT) model, whose output allows to determine the final selections. The selections are designed to optimise the discovery potential of the detector to neutrino point sources. This is done by maximising the number of cosmic neutrino events, while keeping the background low. The track selection targets events from neutrino interactions where there is a μ lepton produced. This is for ν_μ CC and ν_τ CC interactions where the τ decays into a μ.

The maximisation of signal events has to be balanced with the rejection of the abundant atmospheric muon background. The rejection of the atmospheric neutrino background is less paramount, for the discrimination between neutrinos of cosmic origin and from the atmosphere is done on a statistical basis using the difference in spectral index. Fermi acceleration of cosmic rays predicts an E^{-2} dependence of the flux of cosmic neutrinos, while the atmospheric neutrino flux spectral index is higher resulting in fewer events at higher energies.

The full ARCA event rate per year at trigger level is presented in Table 5.1, accompanied by the number of cosmic neutrino events with and without a μ. The atmospheric muon

and neutrino flux model are described in Chapter 4. As described in the previous chapter, the muon bundle energy has a lower threshold at 10 TeV. Lower-energy muons have no significant impact on the analysis presented in this chapter. Expected cosmic event rates are obtained using a cosmic neutrino flux of $\phi^{\nu_i+\bar{\nu}_i} = 1.2 \times 10^{-8} \left(\frac{E_\nu}{\text{GeV}}\right)^{-2}$ GeV^{-1} cm^{-2} s^{-1} sr^{-1}. The increased detection of ν_μ events is attributed to the extensive distances muons can cover. This capability enables the telescope to identify ν_μ events, even when neutrino interactions occur far from the detector. Events from ν_e and ν_τ interactions predominantly exhibit shower-like signatures, depositing all energy in a limited space. As a result, detection is only possible when these events take place in close proximity to the detector.

	Trigger [yr^{-1}]
Atmospheric μ ($>$ 10 TeV)	8.1×10^7
Atmospheric ν	1.9×10^5
Cosmic ν	729
Cosmic ν with μ	459
Cosmic ν without μ	270
Cosmic ν_e	143
Cosmic ν_μ	434
Cosmic ν_τ	152

Table 5.1: Number of events per year for full ARCA at trigger level.

5.1.1 Track selection

The track selection is designed to find upgoing track neutrino events that are well reconstructed. The background contamination is first reduced by a set of selection criteria called the **Level-1** selection. The resulting events are input to the BDT in order to obtain the final selection.

Level-1 selection

The first suppression of background is achieved by selecting upgoing and horizontal events with a reconstructed zenith angle $\theta_{track} > 80°$ obtained using the track reconstruction. Downgoing events are characterised by $\theta = 0°$ and upgoing events by $\theta = 180°$. True upgoing events can only be caused by neutrinos due to the shielding of the Earth, but misreconstructed atmospheric muons can mimic this signal. The majority of atmospheric muons are removed, but a significant number of background events remain as shown in Figure 5.1. The shaded area indicates the region removed by this criterion and the dotted red line indicates cosmic ν events that produce a μ and are reconstructed within 10° of the true neutrino direction.

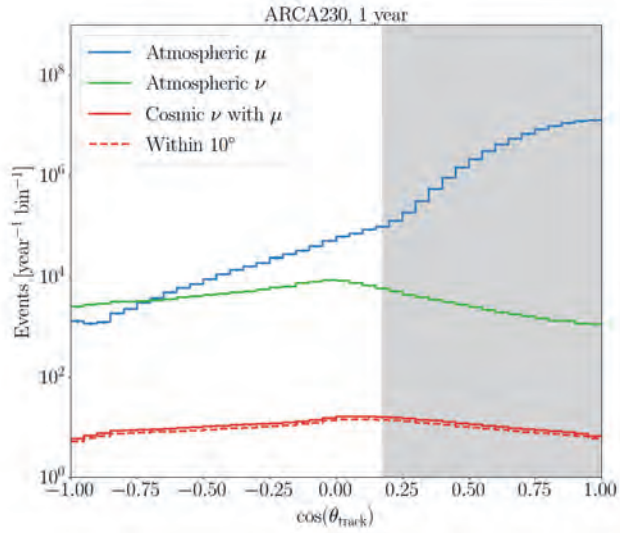

Figure 5.1: Event rate per year as a function of the cosine of the reconstructed zenith angle using full ARCA. The distribution shows all triggered events and the shaded area covers the rejected events due to the zenith criterion.

The misreconstructed atmospheric muons are further suppressed by a series of requirements that complete the Level-1 selection. The criteria are:

- Likelihood: $\log_{10}(L_{\text{track}}) > 1.4$;
- Direction error estimate: $\beta_0 < 1.26°$;
- Track length: $l_{\text{track}} > 100$ m;
- Conditional cut on the energy (E_{track}), the fitted number of photo-electrons along the track (N_{pe}), the likelihood divided by the number of hits used in reconstruction ($N_{\text{reco}}^{\text{hits}}$):
  - $\log_{10}(E_{\text{rec}}\ [\text{GeV}]) > 4.5$;
  - Or ($\log_{10}(E_{\text{rec}}\ [\text{GeV}]) < 4.5$ and $N_{\text{pe}} > 1$ and $L_{\text{track}}/N_{\text{track}}^{\text{hits}} > 0.45$).

The distribution of the track likelihood after the zenith angle requirement is shown in Figure 5.2a. The shaded area covers the rejected events that are excluded in Figure 5.2b, which depicts the direction error estimate. The same procedure applies to Figures 5.2c and d.

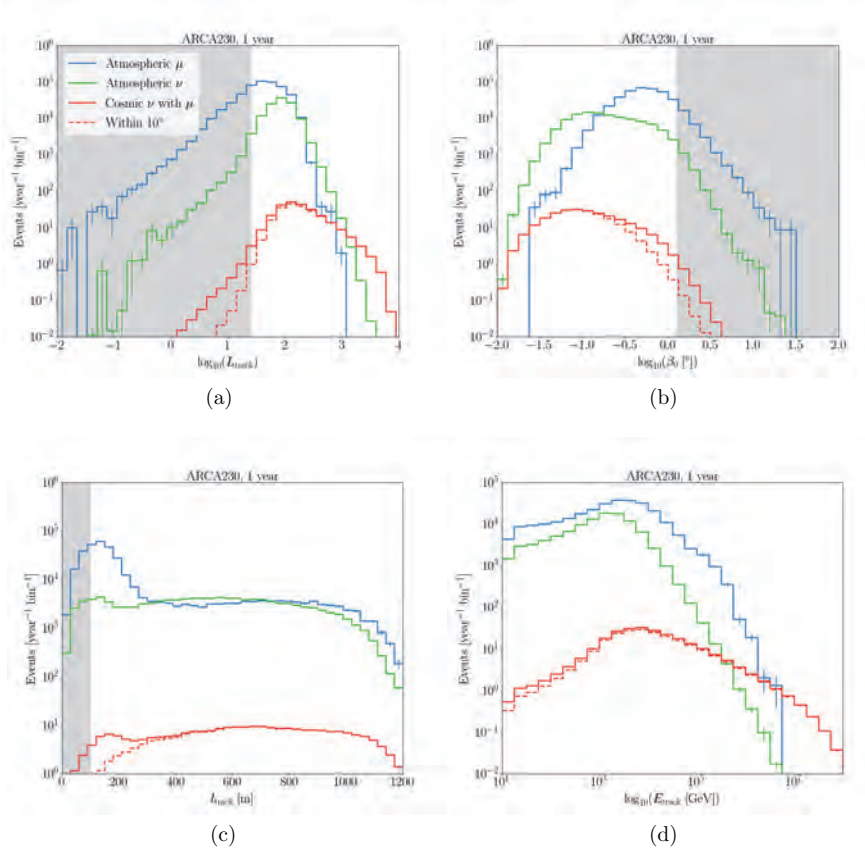

Figure 5.2: Track likelihood (a), direction error estimate (b), fitted track length (c) and reconstructed energy (d) distributions. The top left distribution (a) illustrates the events passing the zenith angle requirement and the shaded area covers the rejected events that are excluded in the following plot. The same procedure applies to (c) and (d).

The events passing the track length criterion are selected if $\log_{10}(E_{\text{rec}}\ [\text{GeV}]) > 4.5$. For $\log_{10}(E_{\text{rec}}\ [\text{GeV}]) < 4.5$, events are selected based on the estimated number of photo-electrons and the likelihood divided by the number of hits, as shown in Figure 5.3. The estimated number of photo-electrons may fall below 1 because events are triggered whenever there are 5 coincident hits according to one of the trigger requirements. In some cases, the track reconstruction may classify these hits as background for the best-fit track hypothesis, leading to a reduced number of estimated photo-electrons.

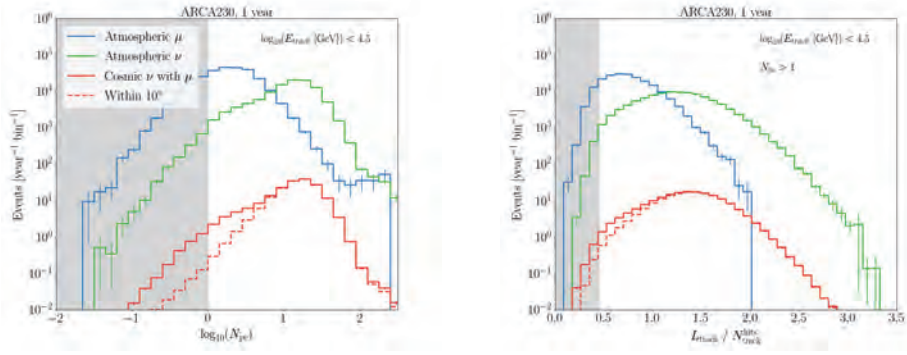

(a) (b)

Figure 5.3: The number of photo-electrons along the fitted track (a) and the track likelihood divided by the number of hits (b) for events passing the track likelihood, the direction error estimate, the track length and $\log_{10}(E_{\text{rec}}\ [\text{GeV}]) < 4.5$ selection requirements.

The number of surviving events per year is shown in Table 5.2.

	Trigger [yr^{-1}]	Up [yr^{-1}]	Level-1 [yr^{-1}]
Atmospheric μ (> 10 TeV)	8.1×10^7	5.3×10^5	2.0×10^5
Atmospheric ν	1.9×10^5	1.2×10^5	1.0×10^5
Cosmic ν with μ	459	260	248
Within 10°	385	227	225

Table 5.2: Number of events per year for full ARCA at different track selection levels.

Boosted decision tree

The sample of events that passes the Level-1 selection are classified by a BDT model. The ROOT::TMVA software package is used to classify the surviving cosmic neutrino and atmospheric background events [96]. The dataset is divided into two subsamples: one for training and another one for evaluating the final result. The model provides a track score where higher values indicate a higher probability to be a cosmic neutrino event. The model is trained using the selection of variables presented in Table 5.3. The variables are listed in order of their importance in discriminating signal from background.

Symbol	Description
N_{pe}	Number of photo-electrons along reconstructed track
β_0	Estimated direction error
d^{μ}_{track}	Distance between closest and furthest μ hypothesis Cherenkov hit
l_{track}	Track length
$\Delta\theta^{\text{max}}_{\text{track}}$	Maximum difference between reconstructed zenith angles of the prefits
θ_{track}	Reconstructed zenith angle obtained using the track reconstruction
$N^{\text{prefit}}_{\text{track}}$	Number of prefits within 1 degree of best fit
$N^{\text{prefit,up}}_{\text{track}}$	Number of upgoing prefits
E_{track}	Reconstructed track energy
$CToT^{\text{both}}_{\text{track}}$ / $C^{\text{both}}_{\text{track}}$	Ratio μ and shower Cherenkov hit ToT with number of hits
$C100^{\text{both}}_{\text{track}}$ / $C^{\text{both}}_{\text{track}}$	Fraction of μ and shower Cherenkov hits within 100 m
$C100^{\mu}_{\text{track}}$ / C^{μ}_{track}	Fraction of μ Cherenkov hits within 100 m
$N^{\text{hits}}_{\text{track}}$	Number of hits used in the reconstruction
$N^{\text{prefit,down}}_{\text{track}}$	Number of downgoing prefits
$L^{\text{max,down}}_{\text{track}}$	Optimal likelihood of a downgoing track
$CToT^{\mu}_{\text{track}}$ / C^{μ}_{track}	Ratio μ Cherenkov hit ToT with number of hits
$C^{\text{both}}_{\text{track}}$	Number of Cherenkov hits that fulfill the μ and shower hypothesis
C^{μ}_{track}	Number of Cherenkov hits that fulfill the μ hypothesis
$d^{\text{both}}_{\text{track}}$	Distance between closest and furthest μ and shower hypothesis Cherenkov hit

Table 5.3: Input variables for the BDT training of the track selection.

The Cherenkov hit variables contain the number of hits that fulfill one or both of the following Cherenkov hypotheses:

$$\text{Shower hypothesis} : |\Delta t| = |t_{\text{hit}} - t_{\text{vertex}} - \frac{d}{c_{\text{water}}}| < 20 \text{ ns}, \tag{5.1}$$

$$\text{Muon hypothesis} : |\Delta t| = |t_{\text{hit}} - t_{\text{vertex}} - \frac{z_j}{c_{\text{vacuum}}} - \tan(\theta_c)\frac{R_j}{c_{\text{vacuum}}}| < 20 \text{ ns}, \tag{5.2}$$

where Δt is the difference between the measured hit time and expected hit time. These hits can be counted with respect to a reconstructed track or shower resulting in 6 variables described in Table 5.4. The number of Cherenkov hits can also be counted within 100 m from the reconstructed vertex ($C100$) and summing the ToT of the hits ($CToT$).

	Reconstructed track	Reconstructed shower
μ hypothesis	C^{μ}_{track}	C^{μ}_{shower}
Shower hypothesis	$C^{\text{shower}}_{\text{track}}$	$C^{\text{shower}}_{\text{shower}}$
Both	$C^{\text{both}}_{\text{track}}$	$C^{\text{both}}_{\text{shower}}$

Table 5.4: Summary of Cherenkov hit variables that quantify the number of hits that are compatible with a track and/or shower hypothesis. This can be calculated for a reconstructed track or shower resulting in 6 variables.

The model is employed on both the test and training samples, as illustrated in Figure 5.4. The patterns in both samples are similar, except for background events exhibiting high track scores. This suggests a slight overtraining of the model on specific features in the training dataset, affecting its generalisation to the newly encountered test dataset. The track score is shown in Figure 5.5 for upgoing ($\theta > 100°$) and horizontal events ($80° < \theta < 100°$).

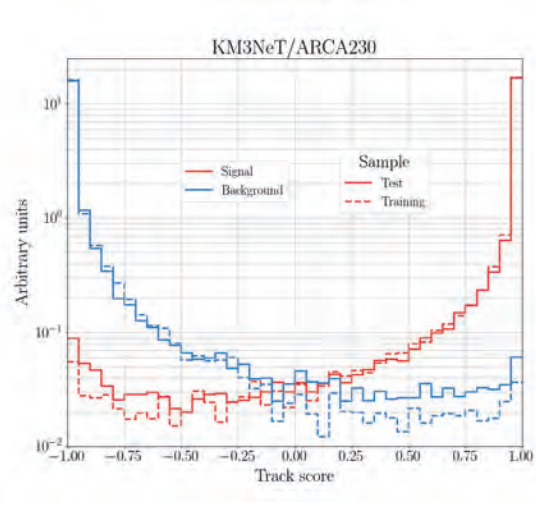

Figure 5.4: Track score for the training and test sample.

The final selection has a stricter requirement for horizontal events due to the higher misreconstructed muon contamination. The selection process maintains a neutrino purity greater than 99% while maximising the signal efficiency. The selection is given by

- $\theta > 100°$: track score > 0.4
- $80° < \theta < 100°$: track score > 0.9.

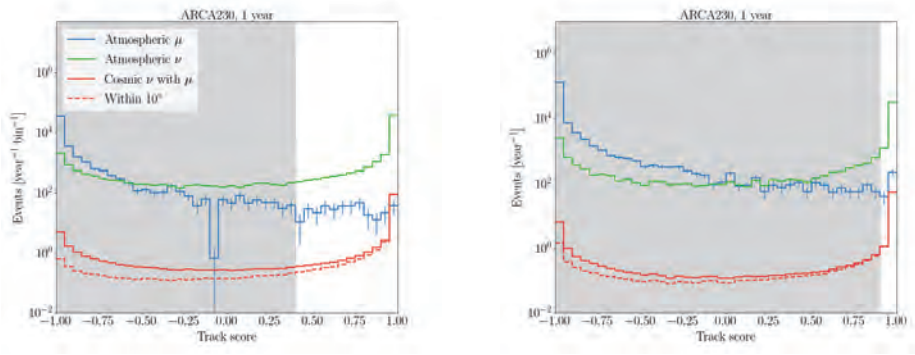

(a) (b)

Figure 5.5: Full ARCA track classifier score for $\theta > 100°$ (a) and $80° < \theta < 100°$ (b). The shaded area covers events that are rejected.

The BDT selection rejected some clear high-energy signal events and therefore an additional selection on the rejected events was designed to improve the signal efficiency at high-energy. Events are selected if they meet one of the following criteria:

- $\log_{10}(L_{\text{track}}) > 2.9$,
- $\log_{10}(\beta_0\ [°]) <$ -1.4,
- $L_{\text{track}}/N^{\text{hits}}_{\text{track}} > 1.9$.

The corresponding distributions for events passing the Level-1 selection are shown in Figure 5.6a,b,c. The sample is completed with events having reconstructed energies surpassing 1 PeV, featuring at least 3 prefits within 1 degree of the best-fit solution, and satisfying the condition $(l_{\text{track}}$- 450 m$)/(L_{\text{track}}/N^{\text{hits}}_{\text{track}}) >$ -320. The final condition is presented in Figure 5.6d for events that meet the requirements of $\log_{10}(E_{\text{rec}}\ [\text{GeV}]) > 6$ and $N^{\text{prefit}}_{\text{track}} > 3$. Although some muons meet this requirement, the fraction of signal that gets rejected is negligible.

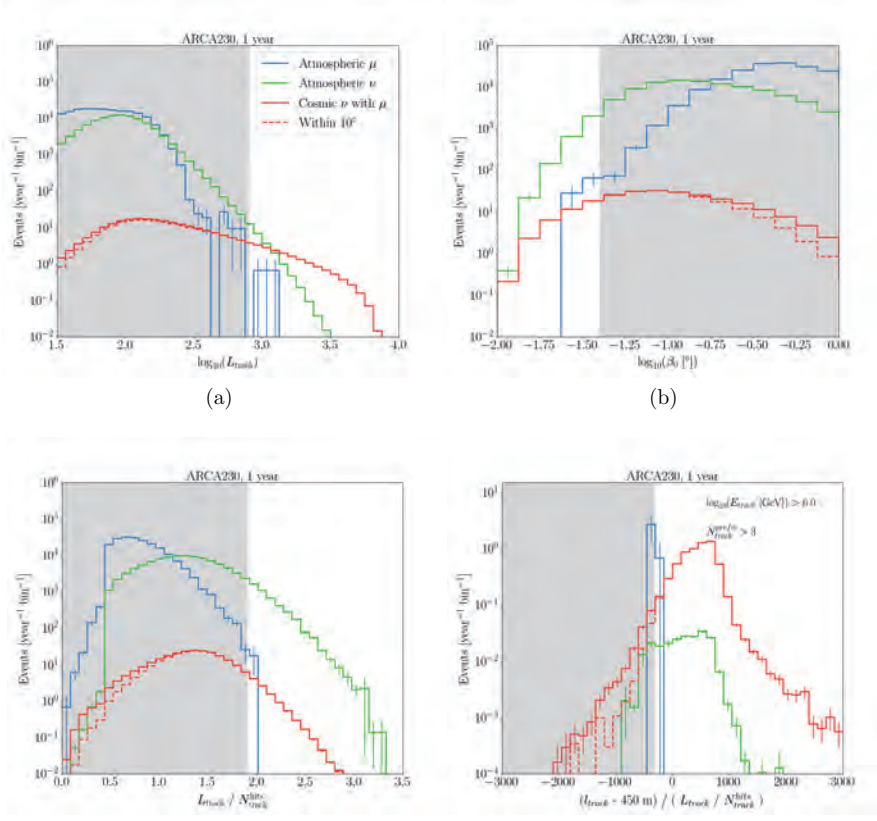

Figure 5.6: Track likelihood (a), direction error estimate (b), track likelihood divided by the number of hits (c) for events passing the Level-1 selection. The fitted track length divided by the likelihood for events satisfying $\log_{10}(E_{\text{rec}}\ [\text{GeV}]) > 6$ and $N_{\text{track}}^{\text{prefit}} > 3$ are shown in (d). The shaded area covers the rejected events.

The final ARCA event rate as a function of the reconstructed energy and zenith angle of the track selection is shown in Figure 5.7. The event rate per year for the BDT selection and the additional selection are shown in Table 5.5, alongside the final selection which sums both contributions.

	Trigger [yr^{-1}]	BDT [yr^{-1}]	Additional [yr^{-1}]	Final [yr^{-1}]
Atmospheric μ (> 10 TeV)	8.1×10^7	600	110	710
Atmospheric ν	1.9×10^5	7.8×10^4	7010	8.5×10^4
Cosmic ν with μ	459	164	52	216
Within 10°	385	161	52	213

Table 5.5: Number of selected events per year for full ARCA at different track selection levels.

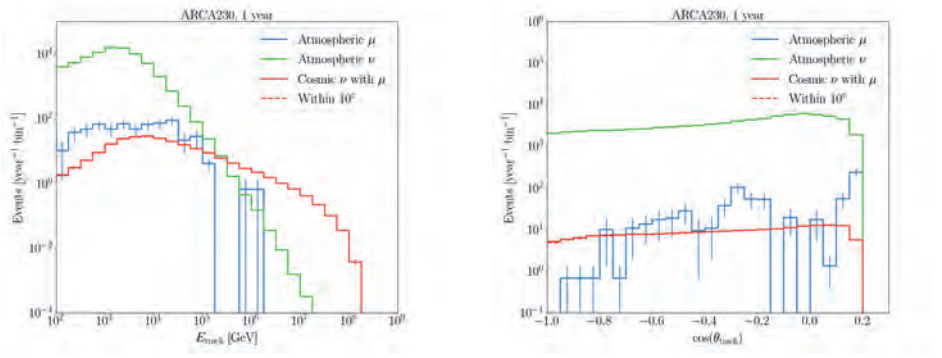

(a) (b)

Figure 5.7: The selected track event rate per year for full ARCA as a function of the reconstructed energy (a) and zenith angle (b).

5.1.2 Shower selection

The selection procedure for shower-like events is optimised to improve the discovery potential for point-like neutrino sources and the diffuse flux by selecting as many neutrino events that do not pass the track selection. The selection focuses on neutrino events that do not result in the production of a μ lepton. This includes events induced by ν_e CC, ν NC and ν_τ CC interactions where the τ decays into an electron or hadrons. Similar to the track selection, the shower selection starts with a set of criteria to reduce the atmospheric muon background. These requirements are called the **Level-1** selection and are followed by the training of another BDT.

Level-1 selection

The Level-1 selection starts with excluding the events that were selected in the track selection. When events pass both selection criteria, they are selected as track due to the superior angular resolution of the track reconstruction. The following requirement considers the reconstruction status. Virtually all events are successfully reconstructed as track and therefore the shower selection uses information from the track and shower reconstruction algorithms. The atmospheric muon background is downgoing and these events typically produce their first hits on the top of the detector. This results in a reconstructed vertex above the detector that can be used to reject a large fraction of the background. Events are selected with a reconstructed track and shower vertex Z-coordinate below 650 m, just below the top layer of optical modules. These selection criteria are called the containment requirements. The reconstructed shower vertices of the muons and the cosmic neutrino events are shown in Figure 5.8, alongside the applied selection.

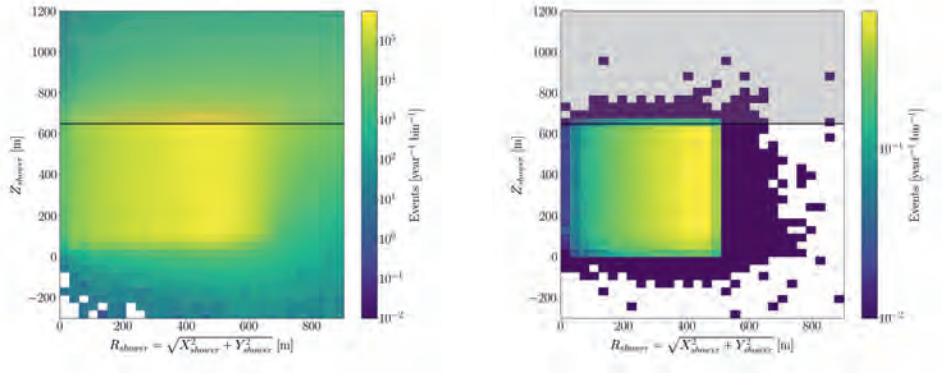

(a) (b)

Figure 5.8: Reconstructed shower vertex positions of muons (a) and cosmic neutrino events (b) that pass the reconstruction status selection requirement. The shaded area represents events that are rejected.

The track reconstruction vertices of the muons and the cosmic neutrino events are shown in Figure 5.9.

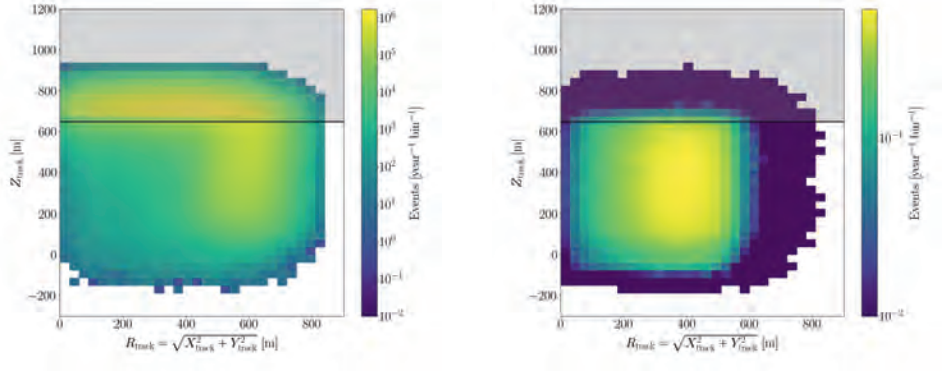

(a) (b)

Figure 5.9: Reconstructed track vertex positions of muons (a) and cosmic neutrino events (b) that pass the reconstruction status selection requirement. The shaded area represents events that are rejected.

The final requirements to complete the Level-1 selection are based on variables that count the number of hits. The number of hits that fulfil the shower Cherenkov hypothesis from Equation 5.1 with respect to the reconstructed shower $C^{\text{shower}}_{\text{shower}} > 10$ is shown in Figure 5.10a. Events are selected with $C^{\text{shower}}_{\text{shower}} > 10$. This selection criteria is called the Cherenkov hit requirement. The following criterion concerns the number of hits used in the shower reconstruction. The logarithm of the number of hits used in the shower reconstruction is shown in Figure 5.10b. Events are selected with $\log_{10}(N^{hits}_{shower}) > 2.6$.

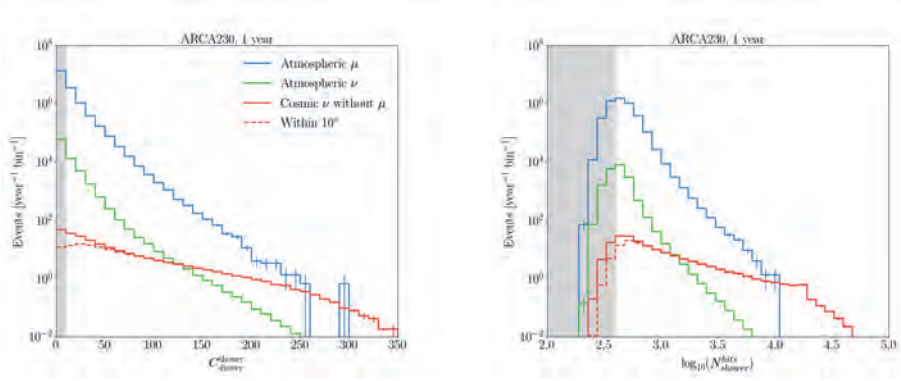

(a) (b)

Figure 5.10: Number of Cherenkov hits that fulfill a shower hypothesis with respect to the reconstructed shower for events that pass the containment requirements (a). Number of hits used in the shower reconstruction for events that pass the Cherenkov hit requirement (b). The shaded area covers events that are rejected.

The Level-1 selection consists of events passing the number of hits requirements and the yearly expected event rates are shown in Table 5.6.

	Trigger [yr^{-1}]	Containment [yr^{-1}]	Level-1 [yr^{-1}]
Atmospheric μ ($>$ 10 TeV)	8.1×10^7	1.9×10^7	3.2×10^6
Atmospheric ν	1.9×10^5	8.0×10^4	1.2×10^4
Cosmic ν without μ	269	220	144
Within 10°	157	133	114

Table 5.6: Event rate per year for full ARCA at different shower selection levels.

Boosted decision tree

The subsequent and final selection criterion is based on a BDT shower score variable. The model is trained using the selection of variables presented in Table 5.7. The variables are listed in order of their importance in discriminating signal from background. The training of the model and evaluation of the dataset are similar to that of the track channel, except for that the model returns a shower score.

Variable	**Description**
l_{track}	Track length
$R_{\text{shower}} = \sqrt{X^2_{\text{shower}} + Y^2_{\text{shower}}}$	Shower reconstruction radius
$R_{\text{track}} = \sqrt{X^2_{\text{track}} + Y^2_{\text{track}}}$	Track reconstruction radius
Z_{shower}	Shower reconstruction height
I_R	Inertia ratio of QStrategy hits
θ_{shower}	Reconstructed zenith angle obtained using the shower reconstruction
Z_{track}	Track reconstruction height
GP_{shower}	Gold parameter of hits used in shower reconstruction
θ_{track}	Reconstructed zenith angle obtained using the track reconstruction
GP_Q	Gold parameter of hits passing the QStrategy hit selection
$N^{\text{hits}}_{\text{track}}$	Number of hits used in track reconstruction
N_{pe}	Number of photo-electrons along reconstructed track
N^{hits}_Q	Number of hits passing the QStrategy hit selection
ToT^{sum}_Q	Total ToT of hits passing the QStrategy hit selection
E_{shower}	Shower reconstruction energy
$C^{\text{shower}}_{\text{shower}}$	Number of Cherenkov hits that fulfill the shower hypothesis
$C100^{\text{shower}}_{\text{shower}}$	Number of Cherenkov hits within 100 m that fulfill the shower hypothesis
$N^{\text{hits}}_{\text{shower}}$	Number of hits used in shower reconstruction
N_{early}	Number of coincident hits with residuals earlier than -20 ns
$CToT^{\mu}_{\text{track}}$	Total ToT of μ hypothesis Cherenkov hits with respect to reconstructed track
L_{shower}	Shower reconstruction likelihood

Table 5.7: Input variables for the BDT model training of the shower selection.

Several variables were inherited from previous analyses that were based on an obsolete vertex reconstruction algorithm; QStrategy. This algorithm is not used anymore, but the hit selection is adapted to calculate variables denoted as Var_{Q}. The gold parameter is defined as an exponential weighted sum of the hit time residuals. The inertia ratio is a metric for the sphericity of the hits. More information on the gold parameter and the inertia ratio can be found in Appendix 9.1 and 9.2. The shower score for the training and test sample is shown in Figure 5.11. The compatibility of the distributions indicates the absence of overtraining on specific features of the training data by the model.

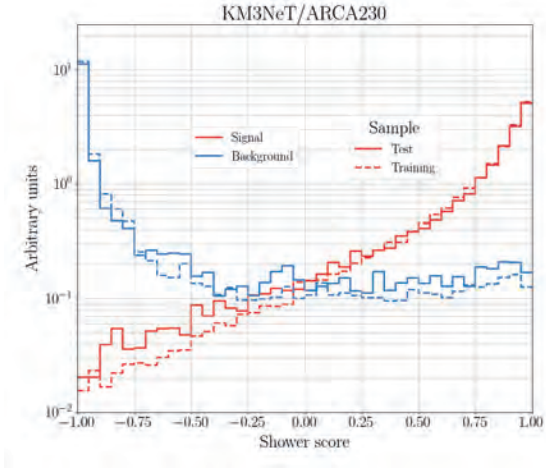

Figure 5.11: Shower score for the training and test sample.

The final selection consists of the Level-1 selection requirements, followed by a selection using the shower score. The shower score as a function of the reconstructed shower energy of the events surviving the Level-1 selection is presented in Figure 5.12. The atmospheric muon distribution has two populations of events at 10 and 50 TeV, matching the two separate muon bundle energy thresholds described in Chapter 4. The discrimination between signal and background is easier at high-energy, which is taken into account by applying an energy-dependent requirement on the shower score according to

$$\text{Shower score} > -0.7 \cdot \log_{10}(E_{\text{shower}}\ [\text{GeV}]) + 2.9, \tag{5.3}$$

which is visualised using the shaded region in the distribution.

The final shower selection event rates are shown in Table 5.8.

	Trigger [yr^{-1}]	Level-1 [yr^{-1}]	Final [yr^{-1}]
Atmospheric μ ($>$ 10 TeV)	8.1×10^7	3.2×10^6	110
Atmospheric ν	1.9×10^5	1.2×10^4	290
Cosmic ν without μ	269	144	53
Within 10°	157	114	52

Table 5.8: Number of events per year for full ARCA at different shower selection levels.

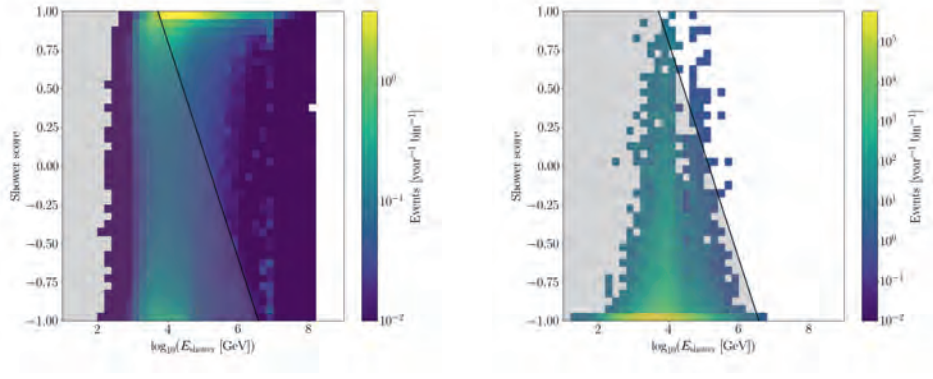

(a) (b)

Figure 5.12: Shower score as a function of the reconstructed energy for muons (a) and cosmic neutrino events (b) that pass the Level-1 selection. The shaded area represents the events that are rejected.

5.1.3 Performance

The effective area $A_{\text{eff}}^{(\nu_i+\bar{\nu}_i)/2}$ at trigger level, and of the final track and shower selections can be found in Figure 5.13 for different neutrino flavours and $\cos(\theta)$ bands. This quantity, integrated over energy and solid angle, is defined as the ratio between the rate of detected events N_{det} and the neutrino flux Φ according to

$$A_{\text{eff}} = \frac{N_{\text{det}}}{\Phi}. \tag{5.4}$$

It represents the area of a hypothetical detector that has a 100% neutrino detection efficiency. The effective area is averaged over particles and anti particles such that each flavour can be convolved with a $\Phi^{\nu_i+\bar{\nu}_i}$ flux in order to obtain the event rate in the detector. The decrease in effective area for upgoing events is due to the absorption of high-energy neutrinos in the Earth. The distribution for the shower channel shows an increase of effective area at 6.3 PeV due the resonant production of a W^- boson when an $\bar{\nu}_e$ interacts with an electron at this specific energy. This phenomenon is known as the Glashow resonance and was discussed in Chapter 2.

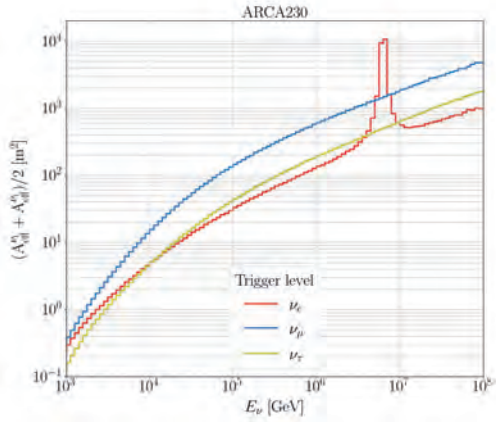

(a)

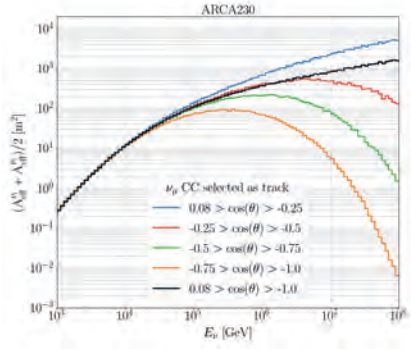

(b)

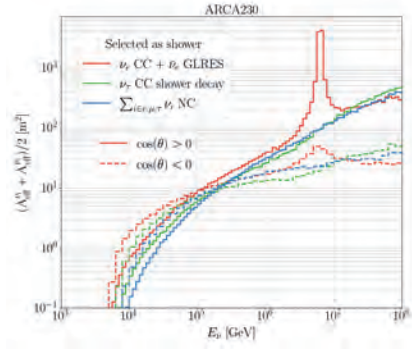

(c)

Figure 5.13: The full ARCA effective area for a flux of $\nu_i + \bar{\nu}_i$ at trigger level for all neutrino flavours and interactions (a). The effective area for ν_μ CC events selected as track for different $\cos(\theta)$ bands (b). The effective area for the shower channel covers both upgoing and downgoing events from ν_e CC, ν_τ CC and ν NC interactions (c).

The angular deviation of the track reconstruction for ν_μ CC events selected as track and of the shower reconstruction for ν_e CC events selected as shower is shown in Figure 5.14. The resolution reaches below 0.1° for tracks and below 2° for showers, which is unprecedented in neutrino telescopes. The angular resolution for tracks is significantly better than for showers due to the different light pattern. Muons travel long distances in the detector, yielding a long lever-arm which constrains the direction.

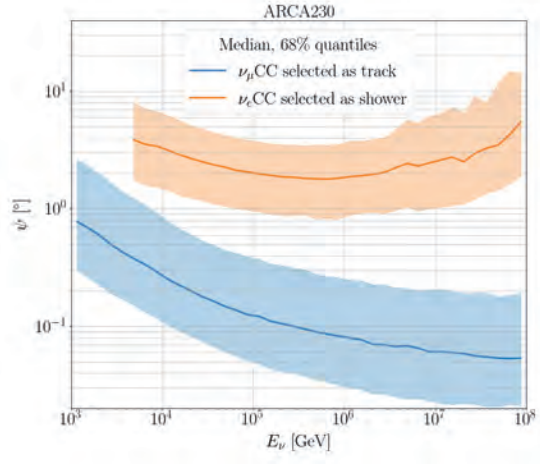

Figure 5.14: Angular deviation of ν_μ CC events selected as track and ν_e CC events selected as shower.

The energy error was defined in Equation 4.10 and is shown in Figure 5.15 together with the median and 68% quantiles.

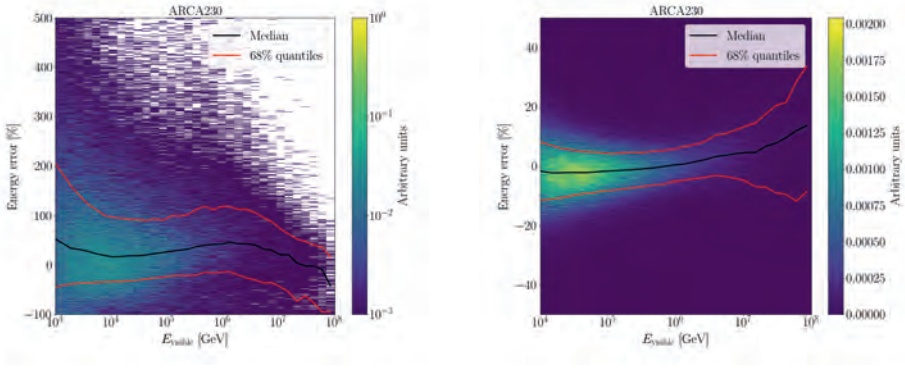

(a) (b)

Figure 5.15: Energy error of ν_μ CC events selected as track and ν_e CC events selected as shower.

The energy resolution is defined as half the difference between the 16th and 84th percentiles of the energy error distributions and is shown in Figure 5.16. The energy resolution for showers improves further when an additional containment cut is applied: $R_{shower} < 500$ m. In contrast to the angular resolution, the energy resolution for showers is significantly better than for tracks, thanks to the containment of events within the detector.

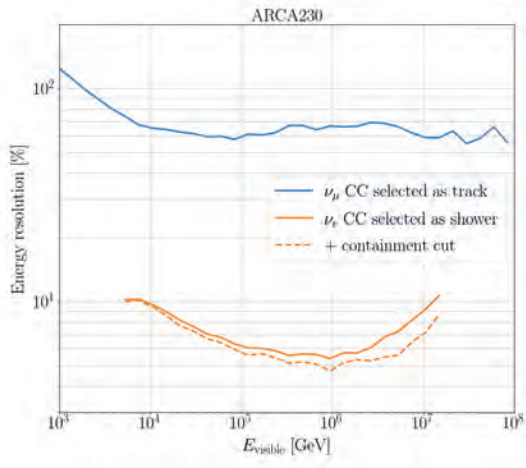

Figure 5.16: Energy resolution of ν_μ CC events selected as track and ν_e CC events selected as shower. The energy resolution for ν_e CC events improves when an additional containment cut is applied: $R_{shower} < 500$ m.

The final event rates per year for full ARCA are shown in Table 5.9, alongside the signal efficiency and the neutrino purity. The signal efficiency is calculated by dividing the number of cosmic neutrino events that pass the selections by the number of upgoing cosmic neutrino events for tracks, and cosmic neutrino events that pass the containment criterion for showers. The purity is significantly higher in the track channel than the shower channel, which can be explained by rejection of downgoing track events. This choice could also be made for the shower channel, resulting in a higher purity but a lower number of signal events. The efficiency of the tracks is also superior to that of showers, but a fair comparison is difficult because the efficiency for tracks is calculated using the cosmic neutrino events after the upgoing selection, and the efficiency for showers using the cosmic neutrino events that survive after a loose containment criterion.

	Trigger [yr^{-1}]	Track selection [yr^{-1}]	Shower selection [yr^{-1}]
Atmospheric μ (> 10 TeV)	8.1×10^7	710	110
Atmospheric ν	1.9×10^5	8.5×10^4	290
Cosmic ν	729	220	59
Cosmic ν with μ	459	216	6
Cosmic ν without μ	270	4	53
Cosmic ν_e	143	3	29
Cosmic ν_μ	434	194	9
Cosmic ν_τ	152	22	21
Efficiency		93.7%	38.8%
Neutrino purity		99.2%	76.8%

Table 5.9: Event rate per year for full ARCA at trigger level and at track and shower selection level.

5.2 Neutrino point sources

The neutrino selections for both tracks and showers are used to create a set of functions that describe the detector performance. These detector-response functions include the effective area, the point spread function and the energy response. The effective area is convolved with a flux model to estimate the number of events in the detector for a given point source. The true energy distribution of the neutrinos is translated to a reconstructed energy distribution by the energy response. The energy response returns a reconstructed energy probability distribution for each true neutrino energy. The neutrinos point back to their source, but the reconstruction introduces possible deviations from their true direction. These deviations are simulated by the point spread function that translates a true neutrino direction to a probability density for possible reconstructed directions. These detector-response functions are used as inputs to the estimation of the sensitivity and discovery potential of full ARCA in the search for point-like neutrino sources.

5.2.1 Point spread function

The angular deviations ψ between the reconstructed and neutrino direction of the selected events are used to construct the point spread function. The point spread function $dP/d\Omega$ is defined as the probability density of ψ per unit solid angle Ω. Distributions of $dP/d\log_{10}(\psi)$ are obtained from the simulations and converted to $dP/d\Omega$ via

$$\frac{dP}{d\Omega} = \frac{d\log_{10}(\psi)}{d\Omega}\frac{dP}{d\log_{10}(\psi)} = \frac{1}{2\psi\pi\sin(\psi)\ln(10)}\frac{dP}{d\log_{10}(\psi)} \tag{5.5}$$

for each neutrino flavour and defined observation channel. This function is constructed for $\log_{10}$ neutrino energy bins of size 0.2 to account for the energy dependence of the reconstruction. Example distributions of $dP/d\log_{10}(\psi)$ and $dP/d\Omega$ for ν_μ CC events selected as track and ν_e CC events selected as shower are shown in Figure 5.17.

5.2.2 Method

The sensitivity and discovery potential estimations are obtained using a *binned* method where the datasets are represented by two-dimensional distributions. The dimensions were chosen by identifying two key characteristics that distinguish a possible cosmic neutrino signal from the atmospheric muon and neutrino background. The first characteristic is the distance of a reconstructed direction to the candidate source location, since signal events are spatially correlated to the source location and the background is not. The second parameter is the reconstructed energy, taking advantage of the different spectral indices for the cosmic neutrino signal and the atmospheric backgrounds.

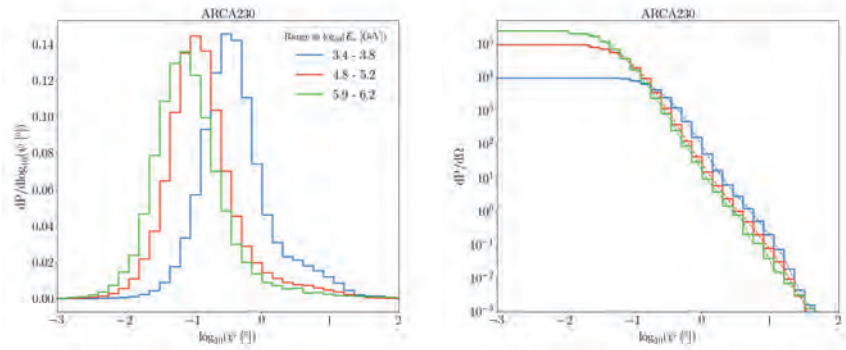

(a) ν_μ CC events selected as track

(b) ν_μ CC events selected as track

(c) ν_e CC events selected as shower

(d) ν_e CC events selected as shower

Figure 5.17: Distributions of $dP/d\log_{10}(\psi)$ (a,c) and $dP/d\Omega$ (b,d) for different energy ranges. The distributions are shown for for ν_μ CC events selected as track (a,b) and for ν_e CC events selected as shower (c,d).

The detector-response functions are used to create expected distributions for signal and background for different flux models and observation times. The flux models are given by a single power law with different spectral indices γ according to

$$\Phi^{\nu_i+\bar{\nu}_i} = \mu \times \Phi_0 \times \left(\frac{E}{\mathrm{GeV}}\right)^{-\gamma}, \tag{5.6}$$

where Φ_0 is the flux normalisation, μ is the signal strength that can be varied and i indicates the neutrino type. The studied spectral indices cover $\gamma = 2.0, 2.5, 3.0, 3.2$, ranging from the expected spectral index $\gamma = 2.0$ due to Fermi acceleration of cosmic rays, to higher spectral indices like for NGC 1068 which was recently determined by the IceCube Collaboration [50].

The expected signal distributions (S_{ij}^c) are obtained by convolving the flux model with the effective area, the point spread function and the energy response. This is done separately for each channel c: track and shower. The background distributions (B_{ij}^c) are obtained by calculating the density of background events as a function of declination δ

from atmospheric neutrinos and muons. An example distribution of expected signal and background events for tracks and showers is shown in Figure 5.18. All following example distributions are shown for a source at $\sin(\delta) = 0.1$ using 3 years of full ARCA operation. The flux model is characterised by spectral index $\gamma = 2.0$, signal strength $\mu = 1$ and flux normalisation $\Phi_0 = 4 \times 10^{-9}$ GeV^{-1}s^{-1}cm^{-2}. The signal distribution for showers shows an increase of events around 6 PeV, which is the energy at which the Glashow resonance cross section has its peak. Fluctuations in the background distribution for showers are explained by the energy distribution of the atmospheric muons passing the shower selection (see Figure 5.12).

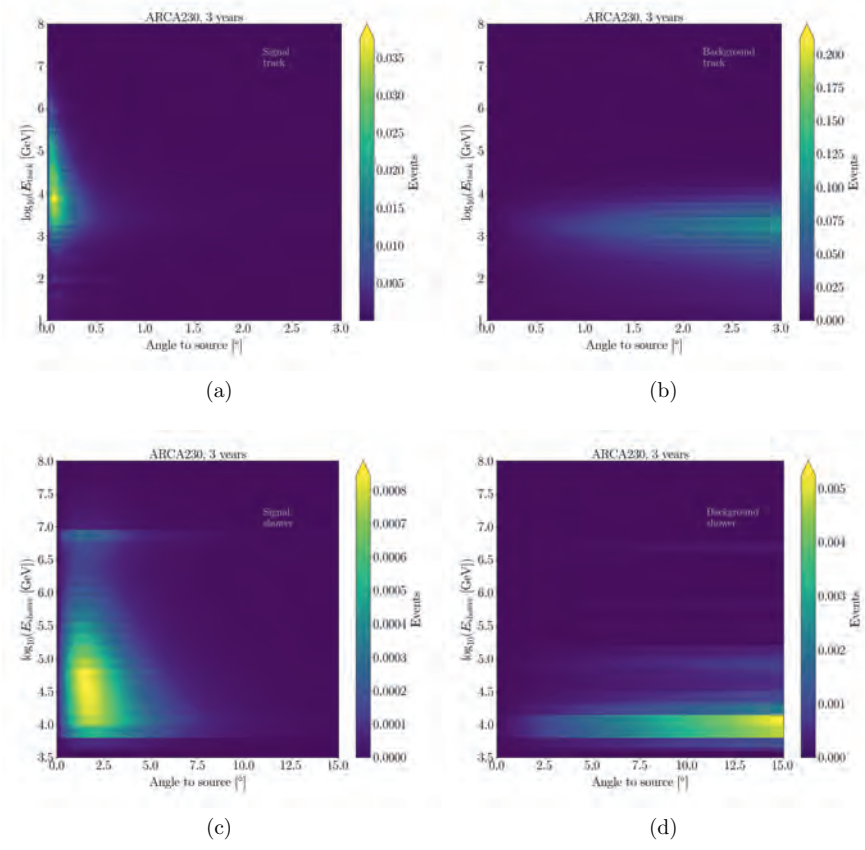

Figure 5.18: Expected signal and background histograms for 3 years of full ARCA operation looking at a source at $\sin(\delta) = 0.1$. The flux has a spectral index of 2.0, a signal strength of 1 and flux normalisation $\Phi_0 = 4 \times 10^{-9}$ GeV^{-1}s^{-1}cm^{-2}. The left column shows the signal histograms and the right column the background histograms. The upper row contains the track channel and the bottom row the shower channel.

Based on the expected signal and background distributions, pseudo-experiments using Poissonian statistics are generated. One pseudo-dataset contains two histograms of observed events; one for the track channel and one for the shower channel. The expectation

value for a pseudo-dataset N_{ij}^c for a given channel c is defined as

$$N_{ij}^c = B_{ij}^c + \mu S_{ij}^c. \tag{5.7}$$

The signal strength μ is varied from 0 for background-only (H0) datasets, and higher values for combined signal and background (H1) datasets. The potential to discriminate H1 from H0 datasets is studied by choosing a test statistic λ. The test statistic is a log likelihood ratio and is defined as

$$\lambda = \log L(\mu = \hat{\mu}) - \log L(\mu = 0), \tag{5.8}$$

where the log likelihood for a H0 hypothesis is subtracted from the log likelihood for a H1 hypothesis. The estimated signal strength $\hat{\mu}$ of the dataset is obtained by maximising the likelihood

$$\log L = \sum_{ij \in \text{bins}} \sum_{c \in \text{channels}} N_{ij}^c \log\left(B_{ij}^c + \mu S_{ij}^c\right) - B_{ij}^c - \mu S_{ij}^c, \tag{5.9}$$

while varying μ.

An example of the test statistic for different signal strengths when looking at the example source introduced earlier in this section using tracks and showers is shown in Figure 5.19.

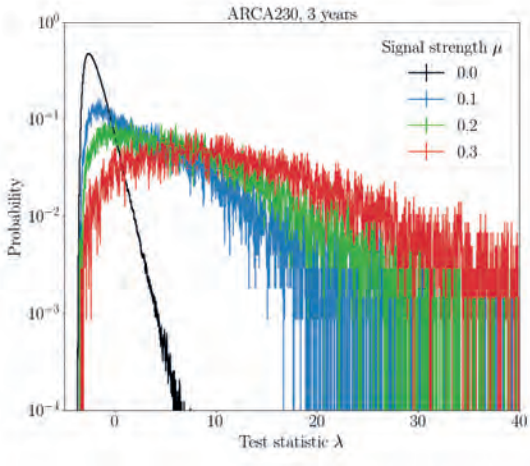

Figure 5.19: Test statistic distribution for a point source at $\sin(\delta) = 0.1$ with 3 years of full ARCA operation. The flux has a spectral index of 2.0 and a flux normalisation of $\Phi_0 = 4 \times 10^{-9}$ GeV^{-1}s^{-1}cm^{-2}.

The test statistic distributions are normalised and used to calculate two statistical quantities: the confidence level and the P-value. The confidence level is found by integrating a signal and background test statistic distribution from the median of the background-only distribution until infinity. This quantity can be used to calculate the signal strength, and therefore neutrino flux, for which the resulting test statistic would be higher than the median for background-only in 90% of the cases. This flux is commonly referred to as the sensitivity of the detector.

The P-value is calculated by integrating the background-only test statistic distribution from the median of a signal test statistic distribution until infinity. The p-values are used to determine the flux normalisation for which a 3σ or 5σ discovery could be claimed

in 50% of the pseudo-experiments. These fluxes are known as the discovery fluxes. An example of the calculation of the confidence level and p-value is shown in Figure 5.20. The confidence levels and p-values for the example source described earlier in this section are shown in Figure 5.21.

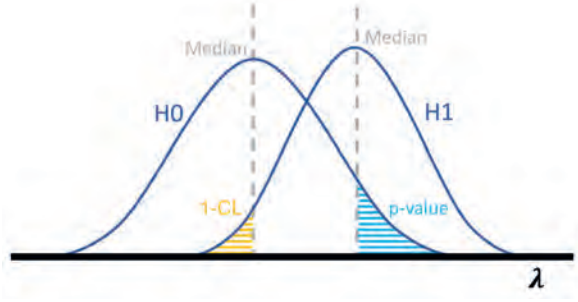

Figure 5.20: Example on the calculation of the P-value and confidence level (CL) using a background-only (H0) and a combined signal and background (H1) test statistic distribution. Adapted from [68].

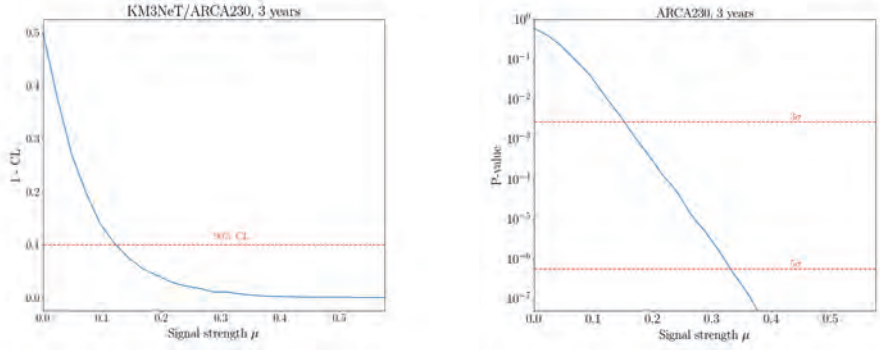

(a) (b)

Figure 5.21: Confidence levels (a) and P-values (b) for a point source at $\sin(\delta) = 0.1$ with 3 years of full ARCA operation. The flux has a spectral index of 2.0 and flux normalisation $\Phi_0 = 4 \times 10^{-9}$ GeV^{-1}s^{-1}cm^{-2}.

5.2.3 Results

The point source sensitivity for a spectral index of $\gamma = 2$ of full ARCA with 3 years of data is shown in Figure 5.22. The track channel is the dominant factor of the performance of the detector in setting the limit on a possible neutrino flux. The addition of the shower channel gives an approximate 11% improvement in the sensitivity.

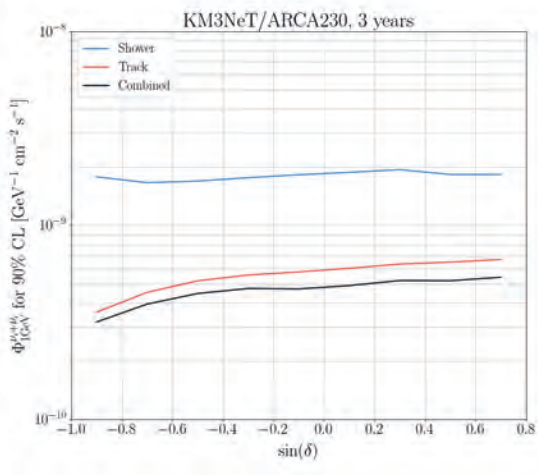

Figure 5.22: Full ARCA point source sensitivity for $\gamma = 2$ for tracks, showers and the combination using 3 years of data.

The full ARCA sensitivity for the combination of tracks and showers is compared with the sensitivity of 15 years of ANTARES [97] and 7 and 10 years of IceCube [98, 99] in Figure 5.23. The sensitivity of full ARCA is better than IceCube for similar livetime due to the better angular resolution of ARCA. The largest difference is found in the Southern Sky, where IceCube is less sensitive due to their location on the Southern Hemisphere. The recent Galactic Plane observation by the IceCube Collaboration [44] puts ARCA in an excellent position to confirm this source and to distinguish point source contributions from diffuse emission.

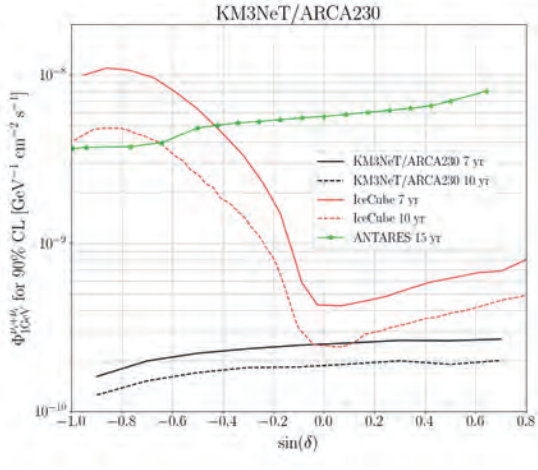

Figure 5.23: The $\gamma = 2$ sensitivity for the combination of channels are compared with 15 years of ANTARES [97] and 7 and 10 years of IceCube [98, 99].

The sensitivities for other spectral indices are shown in Figure 5.24a. The large difference in the flux normalisations for different spectral indices can be explained by the single power law of the flux model. The energy dependence is fixed at GeV: $(\frac{E_\nu}{\text{GeV}})^{-\gamma}$, which results in large differences in the flux normalisation when considering TeV energies or higher where ARCA is sensitive. This can be illustrated by the neutrino flux as a function of the

energy for the different spectral indices, as shown in Figure 5.24b. The flux corresponding to the sensitivity at $\sin(\delta) = 0.1$ using 3 years of full ARCA data is used to calculate the energy dependence of the flux for the different spectral indices. The fluxes overlap at approximately 15 TeV in neutrino energy, which indicates that neutrinos with these energies are most important for ARCA in the search for neutrino point sources.

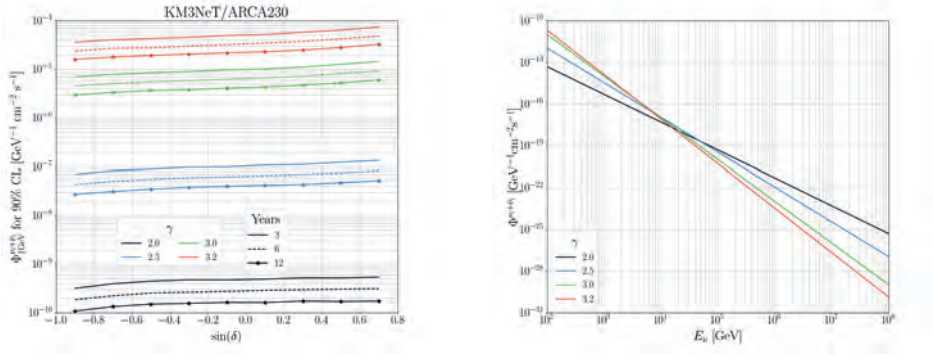

(a) (b)

Figure 5.24: Sensitivity of full ARCA for different spectral indices (a). The neutrino flux as a function of energy for different spectral indices (b). The flux corresponding to the sensitivity at $\sin(\delta) = 0.1$ using 3 years of full ARCA data is used to calculate the energy dependence of the flux for the different spectral indices.

The 5σ discovery fluxes of full ARCA for neutrino point sources are given in Figure 5.25. These fluxes represent the neutrino point source flux that is needed to claim a 5σ discovery.

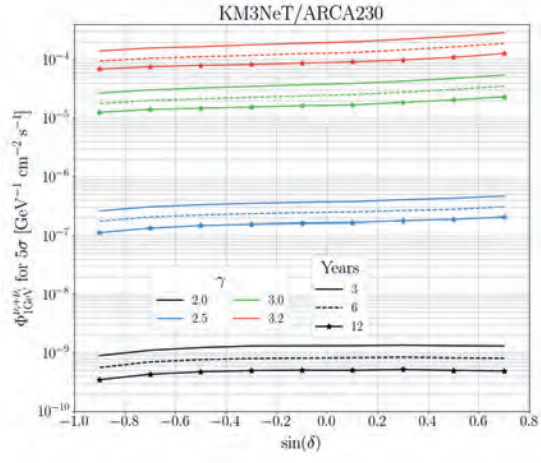

Figure 5.25: Point source 5σ discovery flux for different spectral indices.

NGC 1068

Recently, the IceCube Collaboration reported the discovery of an excess of neutrinos coming from the nearby active galaxy NGC 1068 [50]. The excess has a global significance of 4.2 σ and a single power law was fitted with $\gamma = 3.2$. The discovery potential of ARCA for this flux was studied and is shown in Figure 5.26. A 5σ discovery can be claimed after 3 years of full ARCA operation. IceCube determined the power law between 1.5 and 15 TeV but this analysis assumes a flux over the full energy range. The discovery potential is driven by the contribution from the track channel. This can be explained by the spectral index of the flux, which results in fewer high-energy events. This has a larger impact on the direction resolution of the shower channel, which limits the impact on the discovery potential.

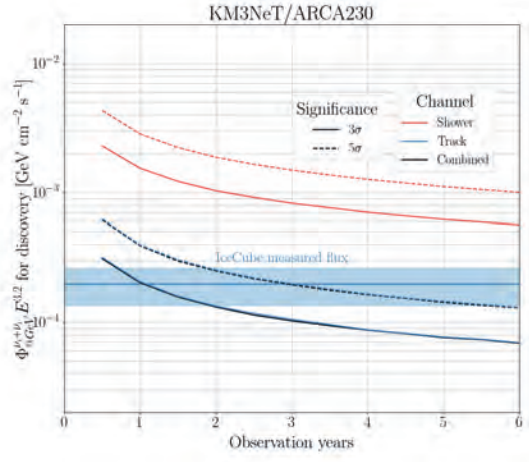

Figure 5.26: The ARCA discovery flux for NGC 1068. The blue lines represent the fitted flux normalisation of IceCube including statistical and systematic uncertainties [50].

5.3 Diffuse flux

The search for an all-sky diffuse flux of cosmic neutrinos follows a similar procedure as the point source analysis. The differences are in the assumed flux model, and the expected signal and background histograms, which now contain $\cos(\theta)$ instead of angular distance to the source. The reconstructed energy ranges from $1 < \log_{10}(E_{rec}\ [\text{GeV}]) < 8$ with 10 bins for tracks and 8 bins for showers. The cosine of the reconstructed zenith angle ranges from -1 to 1 with 20 bins. The distribution of the track reconstruction zenith angles are exclusively populated in the upgoing and horizontal regions. The spectral index of the flux model is equal to the best-fit result from the ν_μ analysis by the IceCube Collaboration [42] and is given by

$$\Phi^{\nu_i+\bar{\nu}_i} = \mu \times \Phi_0 \times \left(\frac{E}{\text{GeV}}\right)^{-2.37}, \tag{5.10}$$

assuming equal flux Φ_0 from ν_e, ν_μ and ν_τ. This reference flux is scaled by the signal strength μ in order to study the discovery potential for this spectral index. An example of expected signal and background distributions can be seen in Figure 5.27 for 3 years of full ARCA operation. The flux normalisation was set at $\Phi_0 = 6.85 \times 10^{-7}$ GeV^{-1} s^{-1} cm^{-2} sr^{-1} with a signal strength of 1.0. Fluctuations in the downgoing region of the background

distribution for showers are explained by the irregular zenith angle distribution of the atmospheric muons passing the shower selection (see Figure 5.12). This region could be removed from the analysis, but this resulted in a worse sensitivity and discovery potential due to the loss of cosmic signal events.

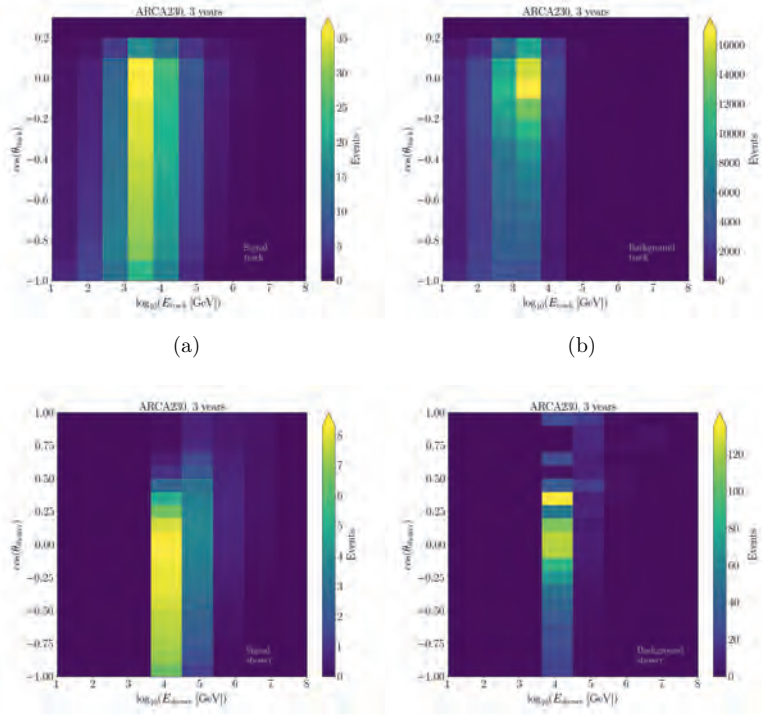

Figure 5.27: Expected signal and background histograms of the diffuse analysis for 3 years of full ARCA operation. The flux normalisation was set at $\Phi_0 = 6.85 \times 10^{-7}$ GeV^{-1} s^{-1} cm^{-2} sr^{-1} with a signal strength of 1.0. The left column shows the signal histograms and the right column the background histograms. The upper row contains the track channel and the bottom row the shower channel.

Similar to the point source analysis, these distributions are used to generate pseudo-experiments for the H0 and H1 hypotheses. The signal is varied by changing the signal strength, which leads to a different flux normalisation. The test statistic is identical to that of the point source analysis as defined in Equation 5.8. An example of the test statistic can be seen in Figure 5.28 and the confidence levels and p-values in Figure 5.29.

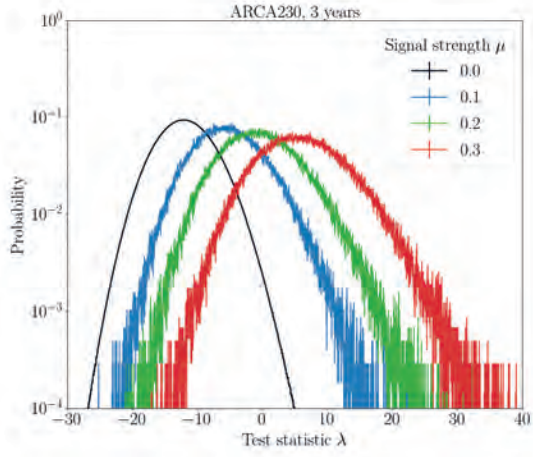

Figure 5.28: Test statistic distribution for the diffuse analysis for 3 years of full ARCA operation using $\Phi_0 = 6.85 \times 10^{-7}$ GeV^{-1} s^{-1} cm^{-2} sr^{-1}.

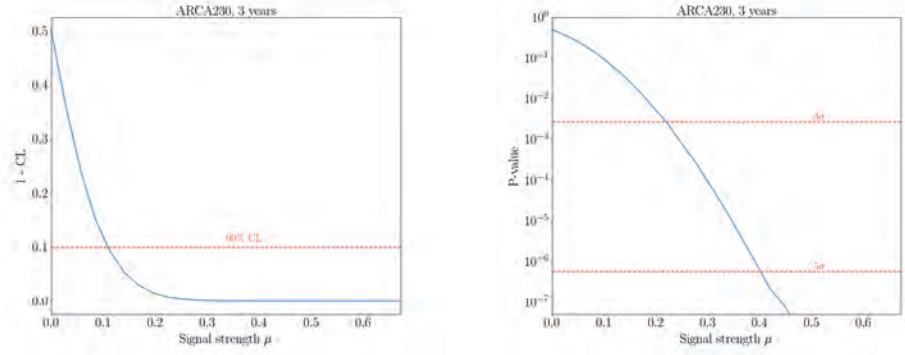

(a) (b)

Figure 5.29: Diffuse analysis confidence levels (a) and P-values (b) for different signal strengths for 3 years of full ARCA operation assuming $\Phi_0 = 6.85 \times 10^{-7}$ GeV^{-1} s^{-1} cm^{-2} sr^{-1}.

The 5σ discovery fluxes for full ARCA are shown in Figure 5.30 for a diffuse neutrino flux with $\gamma = 2.37$ as reported by the IceCube Collaboration [42]. In contrast with the discovery potential for neutrino point sources, the diffuse discovery flux benefits most from the shower channel. The energy resolution is crucial in order to separate the spectral index of atmospheric and cosmic neutrinos, which is better in the shower channel than in the track channel. An all-sky diffuse cosmic neutrino flux having the same properties as the one observed by the IceCube Collaboration can be discovered with 5σ within half a year of full ARCA operation. By taking advantage of data from the current growing detector [71], such re-discovery can happen earlier.

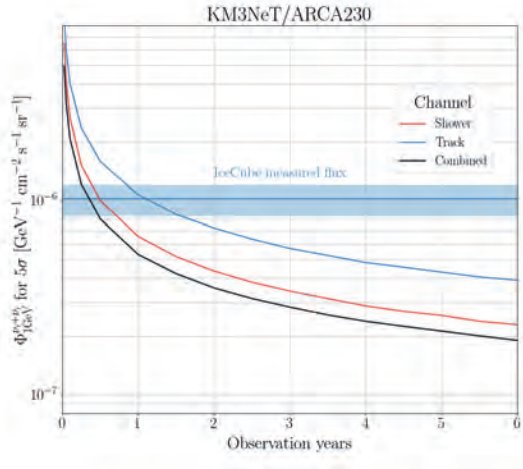

Figure 5.30: The discovery flux for 5σ statistical significances using full ARCA, concerning the diffuse neutrino flux with a spectral index of $\gamma = 2.37$ as reported by IceCube [42]. The blue lines represent the fitted flux normalisation of IceCube including statistical and systematic uncertainties.

5.4 Systematic uncertainties

The results in this chapter are difficult to interpret without a proper understanding of the systematic uncertainties. Systematic uncertainties can introduce biases that affect the accuracy of the results. Recognising and quantifying these uncertainties allows to study their impact on the astronomy potential of full ARCA.

A thorough comprehension of the absorption and scattering lengths of light in water holds significance when reconstructing the detected hit patterns into the physical characteristics of neutrino interactions. The absorption and scattering length of light in the seawater at the ARCA site has been measured with ∼10% accuracy [100]. The precision of these measurements is expected to improve by taking advantage of the LED beacons in the DOMs and the deployment of dedicated calibration units. Previous studies varied the water properties in the light simulation by ±10% and determined the influence on the direction and energy reconstruction [69]. The influence of systematic uncertainties is presented in Table 5.10, as well as the change in reconstruction performance due to missing DOMs and detection strings.

Effect	Track		Shower	
	$\Delta E/E$	$\Delta\psi$	$\Delta E/E$	$\Delta\psi$
$\Delta\lambda_{\mathrm{abs}} = \pm 10\%$	$\pm 8\%$	$\pm 0.1^\circ$	$\pm 30\%$	$< 0.1^\circ$
$\Delta\lambda_{\mathrm{scat}} = \pm 10\%$	$\pm 0.6\%$	$\pm 0.1^\circ$	$< 1\%$	$< 0.1^\circ$
1% missing DOMs		0.01°	$< 0.1\%$	$+0.02^\circ$
1 missing DU		0.01°	$< 0.1\%$	$+0.025^\circ$

Table 5.10: Estimated effects of systematic uncertainties on the event reconstruction performance. Adapted from [69].

The impact on the direction reconstruction is at most $\pm 0.1^\circ$ for both tracks and showers, but the angular resolution for tracks only reached 0.2° at the time of writing Reference [69]. The current track direction reconstruction reaches 0.06°, which is approximately 3 times better. The point source analysis was repeated after adjusting the point spread

function. This involved shifting the median resolution for tracks by $\pm 0.1^\circ$ in scenario I and implementing an identical relative shift as observed in the previous track reconstruction performance in scenario II. The median angular resolution of the showers was also shifted by $\pm 0.1^\circ$ and the impact on the discovery flux for 3 years of full ARCA operation is shown in Figure 5.31. Scenario I yields a maximum degradation of the discovery flux of 20%, while scenario II maintains the degradation within 10%. The impact of changes in the direction reconstruction performance on the discovery potential of the all-sky diffuse neutrino flux is negligible.

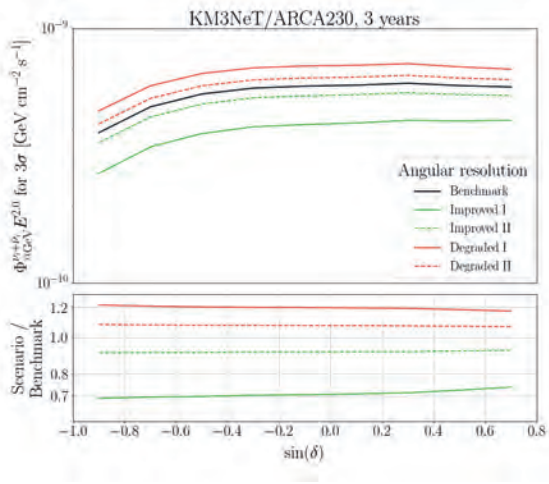

Figure 5.31: The 3σ discovery flux for neutrino point sources using tracks and showers for 3 years of full ARCA operation. The benchmark scenario encompasses the detector performance discussed in the preceding sections. Scenario I and II entail modifications of the direction resolution performance as described in the text.

The largest effect on the energy reconstruction performance was seen when varying the absorption length, resulting in a relative shift of $\Delta E/E \pm +8\%$ for tracks and $\Delta E/E \pm 30\%$ for showers. The energy response of both the point source analysis and the all-sky diffuse analysis was modified and the impact on the 3σ discovery flux stays within 5% for both analyses. The 3σ discovery flux for the diffuse analysis is shown in Figure 5.32.

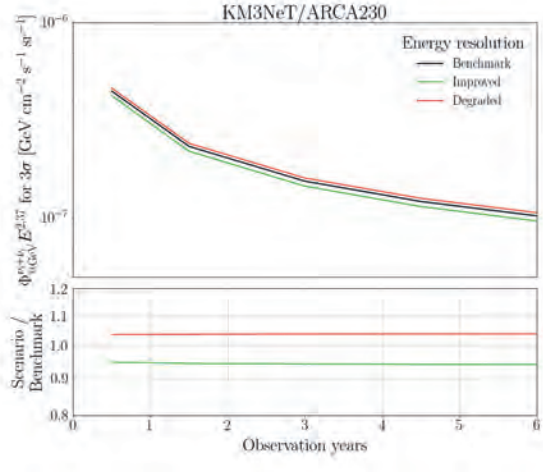

Figure 5.32: The 3σ discovery flux for the all-sky diffuse neutrino flux using tracks and showers. The benchmark scenario encompasses the detector performance discussed in the preceding sections. The improved and degraded scenarios cover the discovery flux after modifying the energy reconstruction performance with $\Delta E/E \pm +8\%$ for tracks and $\Delta E/E \pm 30\%$ for showers.

Another systematic uncertainty is the acceptance of the optical modules to light. In the past, the effective area of the DOM was modelled in GEANT [101] and has been measured within 1% using ^{40}K decays in the seawater [102]. The influence on the reconstruction performance and analysis results are negligible. Recent work with the current ARCA detector studied the influence of uncertainties in the PMT quantum efficiency and water absorption length [71, 72]. The effective area of the PMTs was varied with ±5% and ±10% to study the impact, and an identical modification of the full ARCA effective area was employed for this analysis. The impact on the discovery flux for both the point source search and the diffuse flux analysis stays within 10%. The 3σ discovery flux for the point source analysis is shown in Figure 5.33.

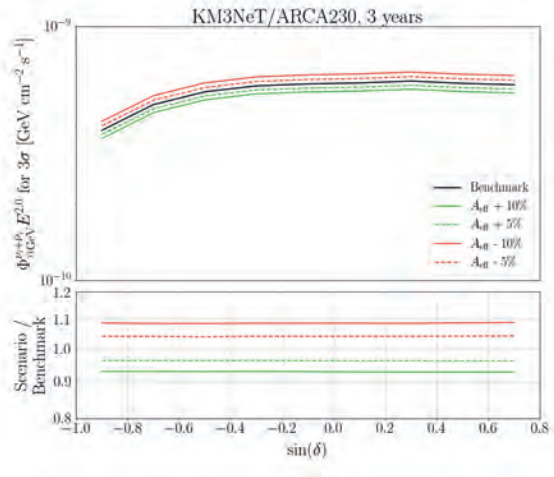

Figure 5.33: The 3σ discovery flux for neutrino point sources using tracks and showers. The benchmark scenario encompasses the detector performance discussed in the preceding sections, while the green and red curves show the discovery flux after modifying the effective area of the detector.

The relative position and orientation calibration of the ARCA21 detector already reaches resolutions necessary for reaching sub 0.1 degree angular resolution [69, 85]. The largest challenge in actually achieving this resolution is found in the absolute orientation of the detector. The first step in absolute pointing will be made by looking at the cosmic ray shadow from the Sun and Moon. Cosmic rays are blocked and this results in a deficit of atmospheric muon events from the known direction of the Sun and Moon. Results using this method have already been shown for ORCA [86], and such analysis is currently being performed for ARCA. The envisaged pointing will be obtained after obtaining the absolute positions of the acoustic emitters on the seafloor. This measurement is scheduled during a sea operation in September 2024. The detection of acoustic signals by the piezos in the DOMs and the hydrophones on the string anchor allows to reconstruct their absolute position and fixing the absolute pointing as described in Section 3.7.

Chapter 6

Point source search using ARCA6-21

Published in "Search for cosmic neutrino point sources and extended sources with 6-21 lines of KM3NeT/ARCA". Proceedings of Science (ICRC2023), no. 1018, 2023. [70].

This chapter applies the search methods discussed in the previous chapter to explore the high-energy neutrino sky with ARCA [70]. The analysis builds upon the initial point source analysis, which utilised data from 6-8 ARCA detection units [68], by incorporating additional data from 19 and 21 detection units. The simulations of the full detector are replaced with *run-by-run* simulations that simulate the background rates and the status of the optical modules during data taking. Another set of event selections was developed to reject background events, before creating a new set of detector-response functions. These functions are not only used to scan the sky and to calculate the sensitivity to neutrino point sources, but also to calculate the test statistic of the ARCA data to determine whether a neutrino point source is significantly detected. The analysis is carried out for 101 astrophysical candidate sources that are possible - or confirmed - high-energy neutrino sources. This chapter presents the results of the study of 101 astrophysical objects and whether they are high-energy neutrino emitters.

6.1 Source candidates

The astrophysical objects examined in this study were chosen for their likelihood of generating high-energy neutrinos. The source candidate list is compiled on the following grounds:

- **Marked by other neutrino telescopes.** The most significant sources from source searches by the IceCube and ANTARES collaborations were selected [99, 103, 104]. This includes the time-integrated discovery of NGC 1068 [50], the association of TXS 0506+056 with a high-energy neutrino [46], and the observation of the Galactic plane with neutrinos [44].
- **Real time alerts.** IceCube alert locations were compared to the 4FGL-DL3 Fermi-LAT catalogue and sources were selected based on their proximity and luminosity [105].
- **High-energy γ-ray sources**. Sources from the LHAASO collaboration [106] and the TeVCat catalogue [107] were selected based on evidence of a hadronic component in cosmic ray production, which is necessary for neutrino production.
- **Extra-galactic active galactic nuclei.** High-energy neutrinos should be accom-

panied by γ rays, but the production regions could be opaque to high-energy photons [108, 109]. Therefore it is believed that sources that are bright radio emitters could be marked as potential neutrino emitters. Sources were selected from the Radio Fundamental Catalog [110] with the brightest radio component.

Approximately 10% of the selected sources are spatially extended in the sky. This is taken into account in the analysis by smearing the point spread function with a Gaussian where the standard deviation is equal to the source extension. An overview of all the candidate sources is found in Appendix 9.3.

6.2 Data sample

This analysis uses data from the period between May 2021 and December 2022 when ARCA was running with 6-21 detector strings. The effective data taking time of 424 days was obtained using four detector configurations, as summarised in Table 6.1. As described in [68], the ARCA6 dataset was split in two due to a period where data was taken with incorrect position and time calibrations in the trigger. Simulations showed that this resulted in a trigger inefficiency of 30%, which is taken into account in the analysis. For simplicity, this work denotes the ARCA6 dataset as a whole.

Configuration	Period	Livetime [days]
ARCA6	May 2021 - September 2021	92
ARCA8	September 2021 - June 2022	210
ARCA19	June 2022 - September 2022	52
ARCA21	September 2022 - December 2022	69

Table 6.1: Effective data taking time for different ARCA configurations.

6.3 Event selection

6.3.1 ARCA6-8

The event selection for ARCA6-8 has been described in [68], but will be briefly summarised in this section. The event selection isolates track-like cosmic neutrino events from ν_μ and $\bar{\nu}_\mu$ CC simulations, while reducing the atmospheric muon background. The atmospheric muons are simulated as described in Section 4.1.2. The background from atmospheric neutrinos emerges from the same ν_μ and $\bar{\nu}_\mu$ CC simulations, but weighted with the atmospheric neutrino flux model. The simulations are used to optimise the selection by maximising cosmic neutrino events while reducing the background. The final background estimate for a neutrino source candidate is obtained from scrambling the ARCA data, which is discussed in Section 6.3.4.

The shower channel was not utilised for this dataset due to the small number of deployed detection strings. The detector covered a relatively small instrumented volume where showers could be contained, resulting in a poor direction resolution and discrimination capability of signal from background.

The track selection requirements for the ARCA6-8 dataset were obtained without a BDT and are defined as:

- Track reconstruction zenith angle: $\theta_{\text{track}} > 84.26^\circ$ ($\cos(\theta_{\text{track}}) < 0.1$),
- Shower reconstruction zenith angle: $\theta_{\text{shower}} > 84.26^\circ$ ($\cos(\theta_{\text{shower}}) < 0.1$),
- Track reconstruction likelihood: $L_{\text{track}} > 50$,
- Number of hits in the track reconstruction: $N_{\text{track}}^{\text{hits}} > 20$.

The selection requirements on the reconstructed zenith angle of the track and shower reconstruction reject the majority of downgoing atmospheric muons. Additionally, conditions on the track likelihood and the number of hits reduce the instances of atmospheric muons being incorrectly identified as upgoing.

The zenith angle and energy distributions of the ARCA6-8 dataset are shown in Figure 6.1, alongside the ratio of data with the sum of event contributions from the simulations. The number of cosmic ν events with a μ is shown, along with the number of events reconstructed within 10°. When comparing the data with the simulations, there is a noticeable underestimation in the simulated event count of the ARCA8 dataset. This discrepancy might be attributed to a type of background events not included in the simulations, yet the discrepancy remains within the uncertainties linked to atmospheric muon simulations. For the ARCA6 dataset, the situation is reversed. This leads to a general underestimation of the simulated event count for the combined ARCA6-8 dataset. The number of events from data and different Monte Carlo (mc) contributions is presented in Table 6.2.

	ARCA6	ARCA8
Data	4205	11537
Atmospheric μ	5020	8260
Atmospheric ν	240	510
Cosmic ν with μ	1.79	4.14
Within 10°	1.24	2.99
Data / mc	0.80	1.32

Table 6.2: Total number of events for the track selection of the ARCA6 and ARCA8 datasets.

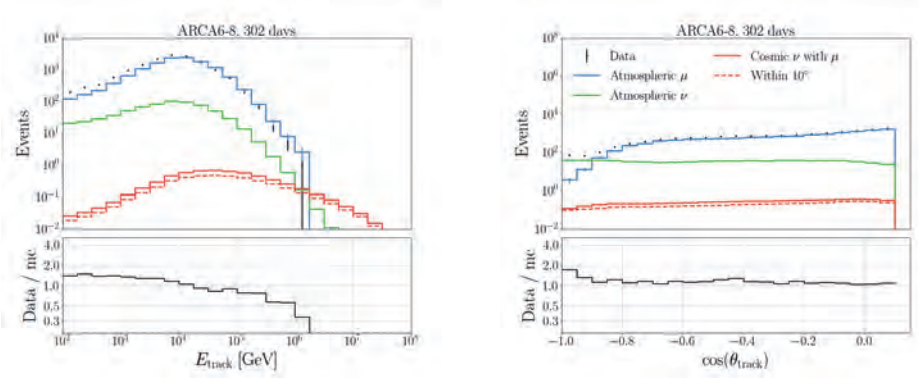

(a) (b)

Figure 6.1: Reconstructed energy (a) and zenith angle (b) at track selection level for the ARCA6-8 dataset.

6.3.2 ARCA19-21

The ARCA19-21 dataset represents 121 days of livetime. For this sample, events reconstructed as showers were incorporated for the first time, giving access to cosmic ν_e and ν_τ. The simulated dataset with ν_μ and $\bar{\nu}_\mu$ CC interactions from the ARCA6-8 analysis was extended with all neutrino flavours and interactions for the ARCA19-21 dataset. This enables a second observation channel based on shower-like events described in Section 6.3.2. The ν_τ CC simulations lead to an approximate 10% rise in track-like cosmic neutrino events, due to the τ lepton's branching ratio of 0.17 for decaying into a muon, creating a track signature. The selection criteria for tracks and showers are tailored to optimise the potential for discovering neutrino point sources.

Track selection

The ARCA19-21 track selection is identical to that of the ARCA6-8 analysis, except that the requirement on the shower reconstruction direction is replaced by a BDT selection.

The event selection before the application of the BDT model is called the **Level-1** selection as described in Section 5.1. The distributions of the variables used for the Level-1 selection are shown in Figure 6.2, where the shaded area covers the region where events are rejected.

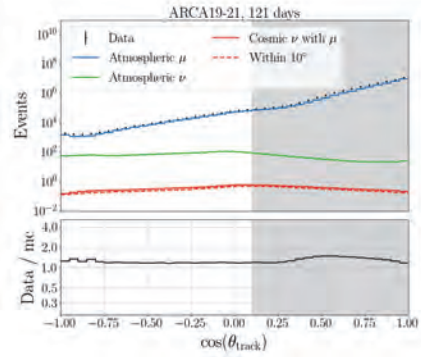

(a)

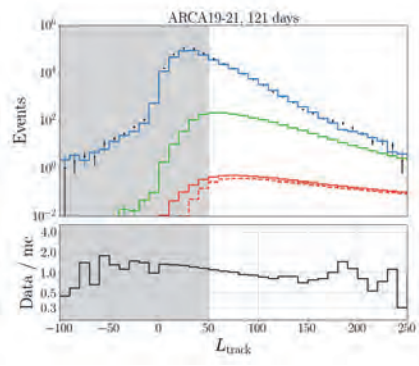

(b)

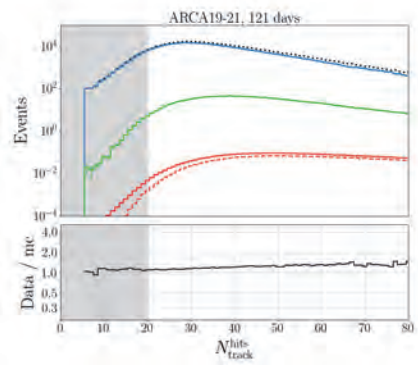

(c)

Figure 6.2: Event distributions for the ARCA19-21 dataset of the reconstructed zenith angle (a), track likelihood (b) and number of hits used in the track reconstruction (c). The shaded region covers events that are rejected.

Next the events are subjected to a BDT selection. The BDT was trained to distinguish upgoing neutrino events from atmospheric muon events that are misreconstructed as upgoing. A separate simulation dataset was produced to train the model. The input variables for training the model are the same as for the full ARCA analysis presented in Table 5.3. A separate model was trained for the ARCA19 and ARCA21 dataset and the resulting classifier score is shown in Figure 6.3. The final requirement selects events with a track score > 0.95 represented by the shaded area in the Figure.

The reconstructed energy and zenith angle distributions of the ARCA19-21 sample are shown in Figure 6.4. The final number of events is shown in Table 6.3.

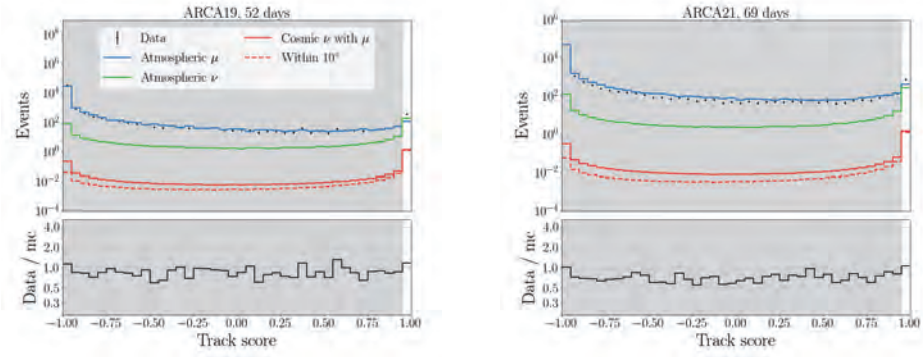

(a) (b)

Figure 6.3: Track score for the data and simulations for the ARCA19 (a) and ARCA21 (b) datasets.

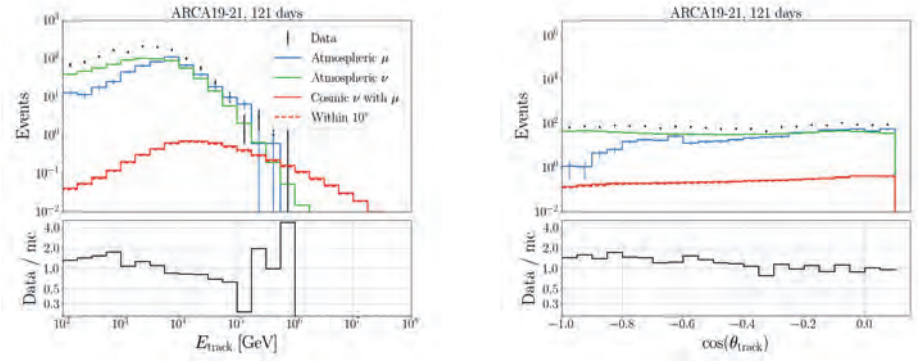

(a) (b)

Figure 6.4: ARCA19-21 reconstructed energy (a) and zenith angle (b) after the BDT selection.

	Trigger	Upgoing	Level-1	Final
Data	84099234	448595	98626	1603
Atmospheric μ	6.3×10^7	3.7×10^5	9.4×10^4	550
Atmospheric ν	5200	1660	1330	810
Cosmic ν with μ	17.9	8.09	7.39	5.8
Within 10°	12.17	6.23	6.02	5.44
Data / mc	1.33	1.19	1.04	1.17

Table 6.3: Total number of events in the ARCA19-21 dataset at different track selection levels, alongside the different contributions from the simulations.

The event display of the event with the highest reconstructed track energy of the ARCA21 dataset is shown in Figure 6.5. The colours represent relative hit times where red and green indicate earlier with respect to blue. The reconstructed energy was estimated at 310 TeV.

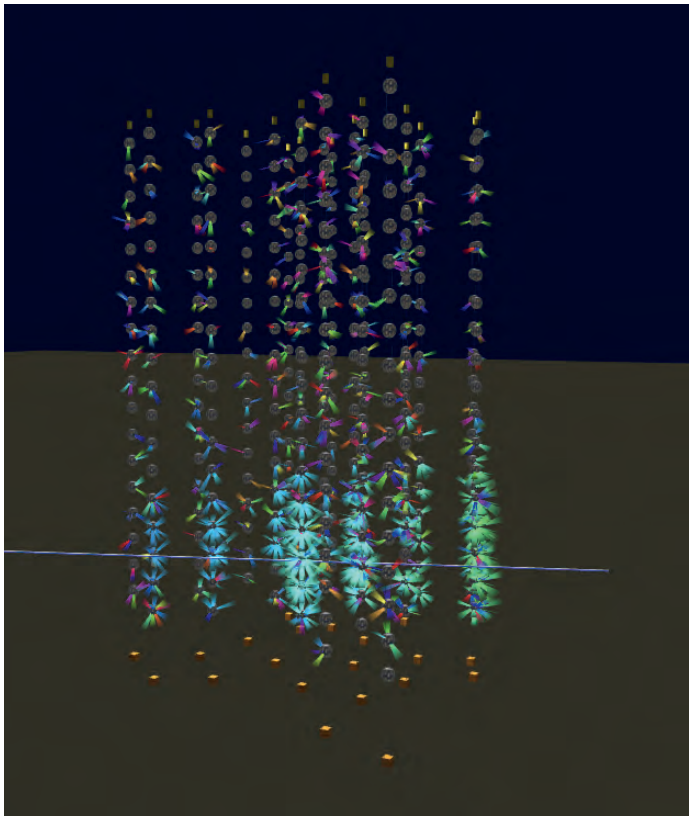

Figure 6.5: Event display for the highest energy event from the ARCA21 track dataset. This event had a reconstructed track energy of 310 TeV.

Shower selection

This section covers the first attempt for an ARCA shower selection using the ARCA19-21 data. The event selection targets events where no muon is produced. This includes ν_e CC, ν NC and ν_τ CC events where the τ decays into an electron or hadrons. The shower selection entails the following series of requirements:

- Reconstruction status: check for complete track and shower reconstruction
- Contained shower reconstruction: $100 < Z_{\text{shower}} < 600$ m and $R_{\text{shower}} = \sqrt{(X_{\text{shower}} - 25.351)^2 + (Y_{\text{shower}} - 289.473)^2} < 274.519$ m
- Track length and number of hits: l_{track} [m] / $N_{\text{track}}^{\text{hits}} < 2.0$
- Inertia ratio: $I_R > 0.1$

The successful reconstruction of showers by the shower reconstruction algorithm is a fundamental criterion for choosing shower events. Having a fully reconstructed track introduces additional variables for event selection. The extra criterion on the track reconstruction success does not exclude signal events arising from cosmic neutrino interactions. The containment requirement selects events within and on the borders of the instrumented volume and is shown in Figure 6.6 alongside the footprint of the detector. This selection requirement results in the rejection of atmospheric muon background events, as well as improving the average reconstruction performance. The reconstructed shower vertex positions for the two datasets are shown in Figure 6.7.

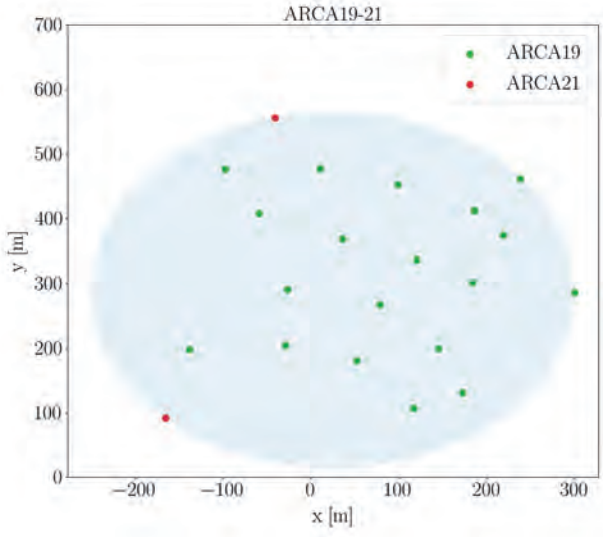

Figure 6.6: Footprint of detector string positions for the ARCA19 and ARCA21 configurations. The circle covers the area in which events are selected.

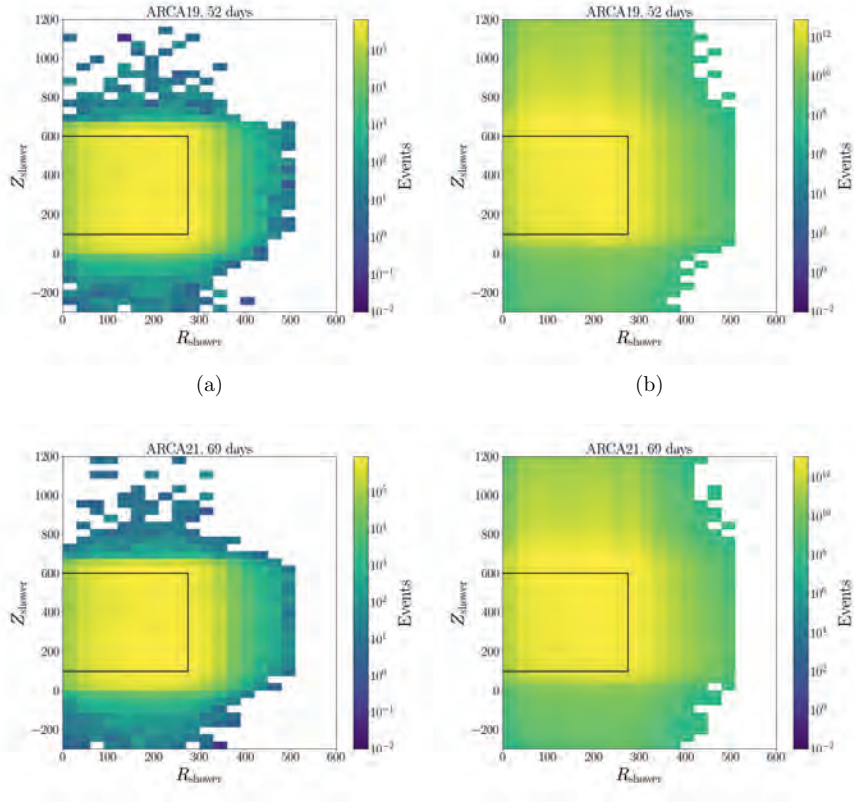

Figure 6.7: Reconstructed shower vertex positions of the ARCA19 (top) and ARCA21 (bottom) datasets for the cosmic neutrino signal (left) and atmospheric muons (right). The box covers selected events.

The selection requirements before the training of the BDT include the fitted track length and the number of hits used in the track reconstruction. Shower events are shorter in length compared to tracks from muons, which is used to reject muons from the atmospheric background sources. Another requirement was set on the inertia ratio I_R, which was used in the full ARCA selection. This ratio is a measure of the sphericity of the hit pattern, and is close to 0 for linear tracks and approaches $\frac{1}{3}$ for spherical patterns. A detailed description of the inertia ratio is given in Appendix 9.2. The event distributions of the shower selection variables are shown in Figure 6.8. The number of cosmic ν events without a μ is shown, along with the number of events reconstructed within 20°.

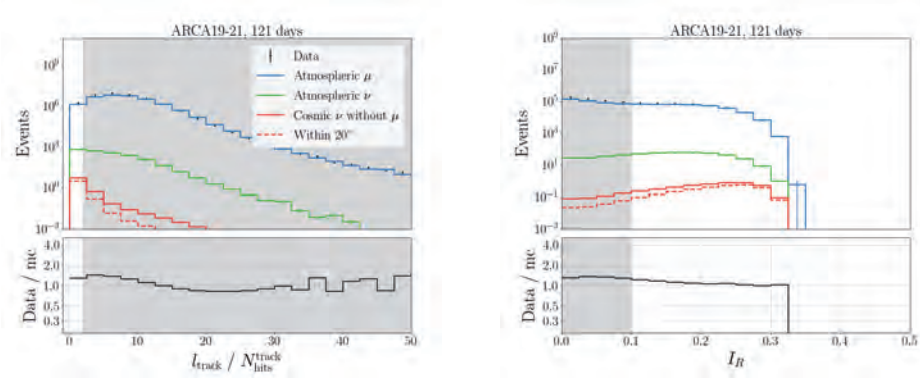

(a) (b)

Figure 6.8: The reconstructed length divided by the number of hits (a) of events passing the containment criteria for the ARCA19-21 dataset. The inertia ratio (b) of events passing the reconstructed length divided by the number of hits requirement. The shaded area covers events that are rejected.

The events passing the inertia ratio selection are used to train a BDT model. The training is done using the same dedicated training simulation sample that was used for the track channel. After training, the model is used to evaluate the whole dataset of events that are passing the previously described selection criteria. The variables used for training are presented in Table 6.4, ordered in their importance to discriminate signal from background.

Variable	Description
θ_{shower}	Reconstructed zenith angle obtained using the shower reconstruction
θ_{track}	Reconstructed zenith angle obtained using the track reconstruction
Z_{shower}	Shower reconstruction height
$R_{\text{shower}} = \sqrt{X^2_{\text{shower}} + Y^2_{\text{shower}}}$	Shower reconstruction radius
GP_{shower}	Gold parameter of hits used in shower reconstruction
$R_{\text{track}} = \sqrt{X^2_{\text{track}} + Y^2_{\text{track}}}$	Track reconstruction radius
N_{pe}	Number of photo-electrons along reconstructed track
GP_Q	Gold parameter of hits passing the QStrategy hit selection
Z_{track}	Track reconstruction height
E_{track}	Track reconstruction energy
L_{track}	Track reconstruction likelihood
$N^{\text{hits}}_{\text{track}}$	Number of hits used in track reconstruction
$C^{\text{shower}}_{\text{shower}}$	Number of Cherenkov hits that fulfill the shower hypothesis
I_R	Inertia ratio of QStrategy hits
l_{track}	Track reconstruction length
N^{hits}_{Q}	Number of hits passing the QStrategy hit selection
E_{shower}	Shower reconstruction energy
$C^{\text{shower}}_{\text{track}}$	Number of Cherenkov hits that fulfill the shower hypothesis with respect to the track reconstruction
$N^{\text{hits}}_{\text{shower}}$	Number of hits used in shower reconstruction
ToT^{sum}_{Q}	Total ToT of hits passing the QStrategy hit selection
$C100^{\text{shower}}_{\text{shower}}$	Number of Cherenkov hits within 100 m that fulfill the shower hypothesis
C^{μ}_{shower}	Number of Cherenkov hits that fulfill the muon hypothesis with respect to the shower reconstruction
L_{shower}	Shower reconstruction likelihood
C^{μ}_{track}	Number of Cherenkov hits that fulfill the track hypothesis
$CToT^{\text{shower}}_{\text{shower}}$	Total ToT of shower hypothesis Cherenkov hits

Table 6.4: Input variables for the BDT model training of the shower selection for the ARCA19 and ARCA21 datasets. The variables are ordered according to their importance.

The model provides each event with a shower score, where higher values indicate a higher probability to be signal. The shower score of the evaluated dataset is given in Figure 6.9. The atmospheric muon contamination at high shower scores highlights the difficulty to discriminate signal from background for these datasets. The final shower selection is identical to the track selection with the following requirement: shower score > 0.95.

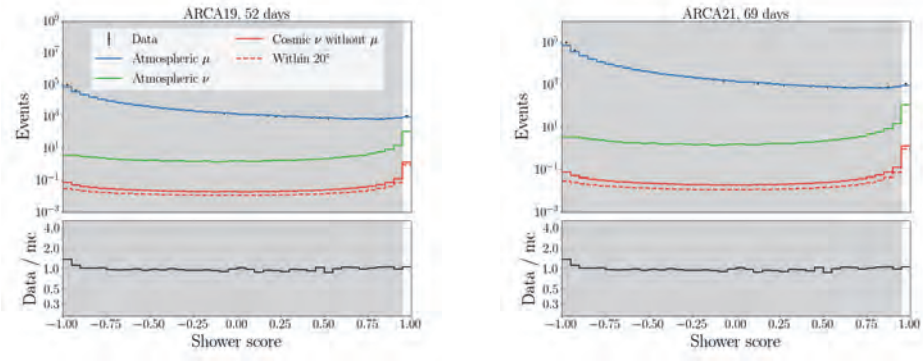

(a) (b)

Figure 6.9: Shower score for the ARCA19 (a) and ARCA21 (b) datasets.

The reconstructed energy and zenith angle distributions of events passing the shower selection are given in Figure 6.10 and the corresponding event rates are shown in Table 6.5.

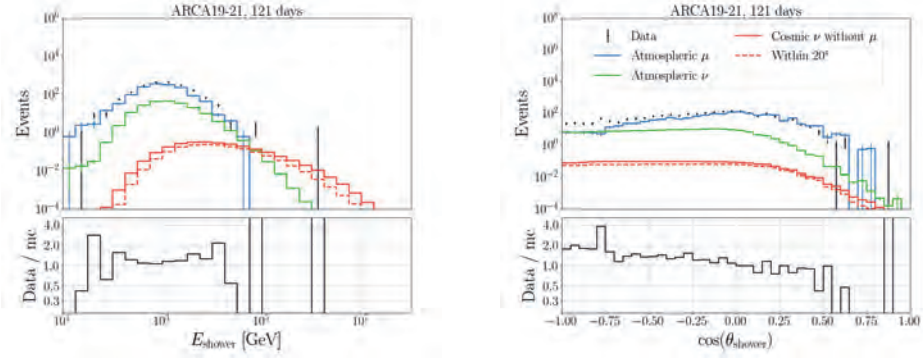

(a) (b)

Figure 6.10: Reconstructed energy (a) and zenith angle (b) of events passing the shower selection for ARCA19-21.

	Trigger	Contained	Length / hits	Inertia	Final
Data	84099234	30064727	1034356	463450	1913
Atmospheric μ	6.3×10^7	2.3×10^7	8.3×10^5	4.1×10^5	1430
Atmospheric ν	5200	1970	510	370	200
Cosmic ν without μ	10.13	5.82	4.8	4.33	2.21
Within 20°	4.63	3.17	2.84	2.7	1.51
Data / mc	1.33	1.29	1.24	1.14	1.17

Table 6.5: Total number of events for the ARCA19-21 dataset passing different shower selection levels.

The event display with the highest reconstructed shower energy is shown in Figure 6.11. The reconstructed energy was estimated at 1.3 PeV.

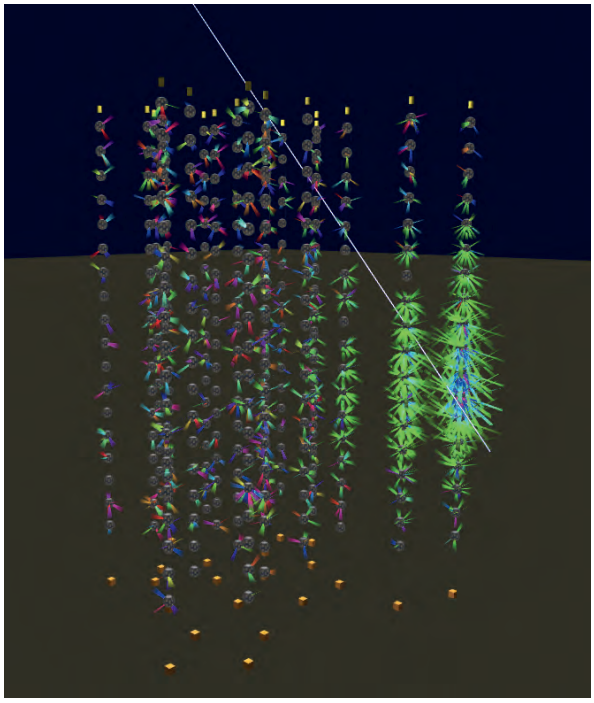

Figure 6.11: Event display for the highest energy event from the ARCA21 shower dataset. This event had a reconstructed shower energy of 1.3 PeV.

6.3.3 Performance

The number of events passing the track selection of the different datasets is presented in Table 6.6. The selection efficiencies for track signal events are $\sim 77\%$ for the ARCA6-8 period, and $\sim 87\%$ for the ARCA19-21 period. The efficiency is calculated by dividing the number of cosmic neutrino events by the number of events after the upgoing selection requirement. The higher efficiency for ARCA19-21 can be attributed to the larger detector which simplifies the rejection of atmospheric muons. The combined ratio of events from data and simulations (data/mc) shows a 13% overall underestimation of the data by the simulation, but this does not affect the point source analysis since the background estimate comes from scrambled data. This approach eliminates the reliance of the analysis on the anticipated number of background events as predicted by atmospheric muon and neutrino simulations. More details are provided in Section 6.3.4.

	ARCA6	ARCA8	ARCA19	ARCA21
Data	4205	11537	516	1087
Atmospheric μ	5020	8260	130	430
Atmospheric ν	240	510	290	520
Cosmic ν with μ	1.79	4.14	2.26	3.54
Within 10°	1.24	2.99	2.14	3.3
Data / mc	0.8	1.32	1.23	1.15
Efficiency	77%	77%	86%	88%
Neutrino purity	4.6%	5.8%	70%	55%

Table 6.6: Total number of events selected as track for the ARCA datasets.

The number of events passing the shower selection is shown in Table 6.7. The efficiency is calculated with respect to the containment criterion.

	ARCA19	ARCA21
Data	808	1105
Atmospheric μ	510	910
Atmospheric ν	80	110
Cosmic ν without μ	0.93	1.28
Within 20°	0.63	0.89
Data / mc	1.35	1.07
Efficiency	0.38	0.38
Neutrino purity	0.14	0.11

Table 6.7: Total number of events selected as shower for the ARCA19 and ARCA21 datasets.

The effective areas of the different detector periods are shown in Figure 6.12 for events induced by ν_μ CC interactions that were selected as track. The effective area for ARCA already exceeds the effective area for upgoing events of the ANTARES detector.

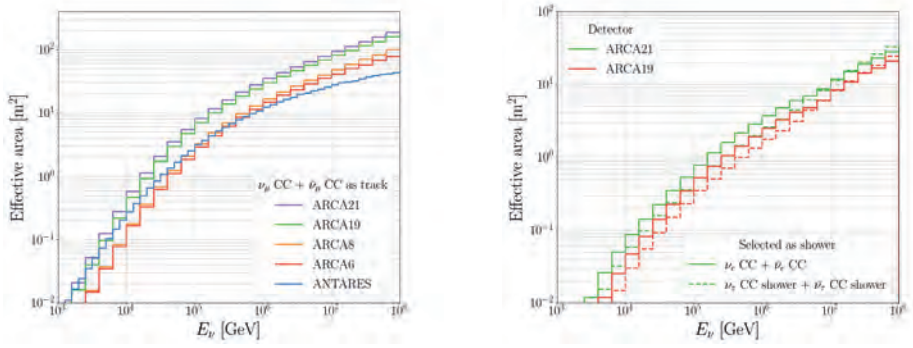

(a) (b)

Figure 6.12: Effective area as a function of neutrino energy for events induced by ν_μ CC interactions selected as track for the ARCA6-8-19-21 detector configurations (a). The same is presented for neutrino events induced by ν_e CC and ν_τ CC interactions where the τ decays into an electron or hadrons (b).

The angular resolution for ν_μ CC events selected as track and ν_e CC selected as shower is shown in Figure 6.13. The resolution for tracks improved significantly for ARCA19-21 with respect to ARCA6-8, and reaches 0.2° at the highest energies. For the full detector this is expected to improve towards 0.06° as seen in the previous chapter. The shower direction resolution is poor and this was not understood at the time at which the analysis was performed. The poor resolution was recently attributed to an error in the reconstruction software that did not incorporate the correct status of the PMTs during data taking. The simulations produced data with various malfunctioning PMTs turned off, but this was not propagated to the reconstruction software. This problem leads to the presented reconstruction performance and was not fixed for this analysis, but future angular resolutions with the ARCA21 detector will already approach 2° for full ARCA as described in Chapter 5.

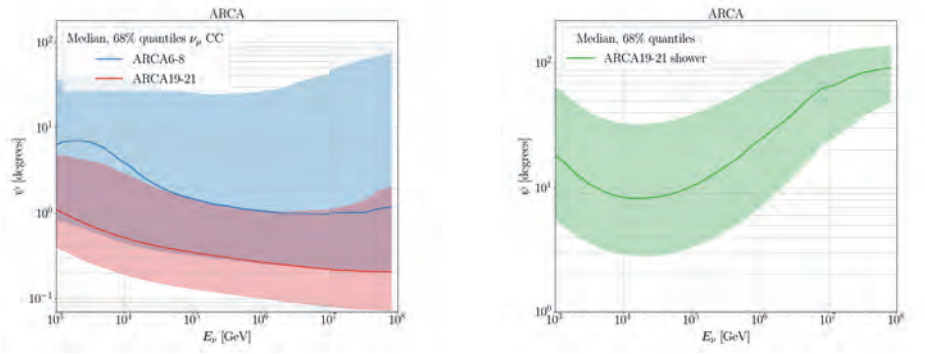

(a) (b)

Figure 6.13: Angular resolution as a function of neutrino energy for ν_μ CC events selected as track (a) and ν_e CC events selected as shower (b).

The energy resolution for selected events is shown in Figure 6.14. The shower energy resolution improves at higher energies which is opposite to the direction reconstruction.

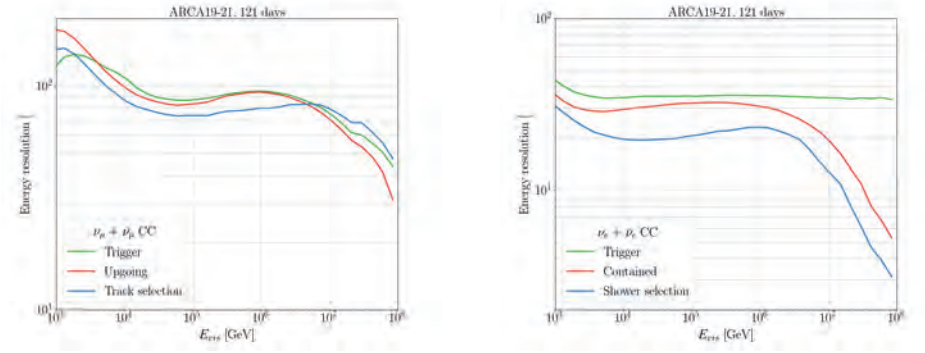

(a) (b)

Figure 6.14: Energy resolution as a function of the visible energy for ν_μ CC events selected as track (a) and ν_e CC events selected as shower (b).

6.3.4 Background expectation

The estimate of the background is obtained by scrambling the data in right ascension. A spline is fitted to the declination of the data and the energy dependence $F(\log_{10}(E))$ is modeled by a sum of two or three Gaussians. The expected number of background events N_{bkg} around each candidate source is calculated using

$$N_{\text{bkg}} = n \times F(\delta) \times F(\log_{10}(E)) \tag{6.1}$$

where the normalisation n is defined to ensure that the integration over all energies and over the full sky gives the total number of events in the data. The data and the background model for the ARCA21 dataset is shown in Figure 6.15. Similar models are made for the other datasets.

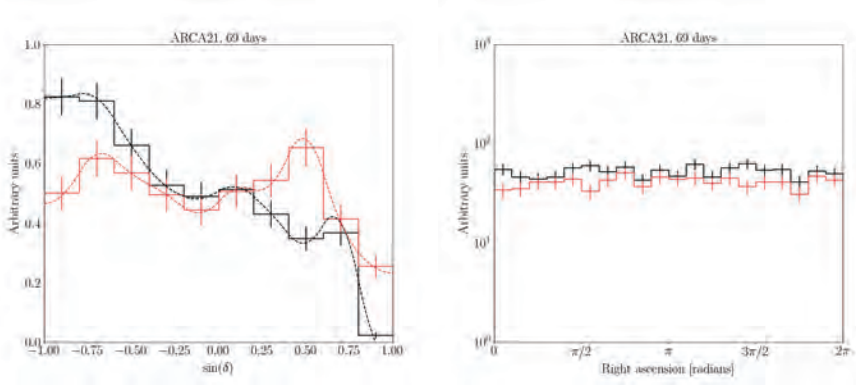

(a) (b)

(c)

Figure 6.15: The background model for ARCA21. Distributions of events that are selected as track and shower are shown as a function of sin(δ) (a), right ascension (b) and the reconstructed energy (c). The histograms with data are superimposed with the corresponding fits.

6.4 Point source search analysis

In the search for point sources, the same binned approach employed in the full ARCA analysis from the previous chapter is utilised. The analysis tests the hypothesis of neutrino flux models with spectral indices $\gamma = 2$ and 2.5. Furthermore a spectrum with $\gamma = 3.2$ is tested for one source: the nearby active galaxy NGC 1068 that was recently discovered by the IceCube Collaboration as a neutrino source [50]. The neutrino spectrum is convolved with the declination dependent effective area for a given source location. This results in separate event distributions for each detector period and observation channel. The events are smeared with the energy and direction response of each detector. An example of the point spread function for tracks and showers using the ARCA21 detector is shown in Figure 6.16. The point spread functions of all detector periods are compared in Figure 6.17.

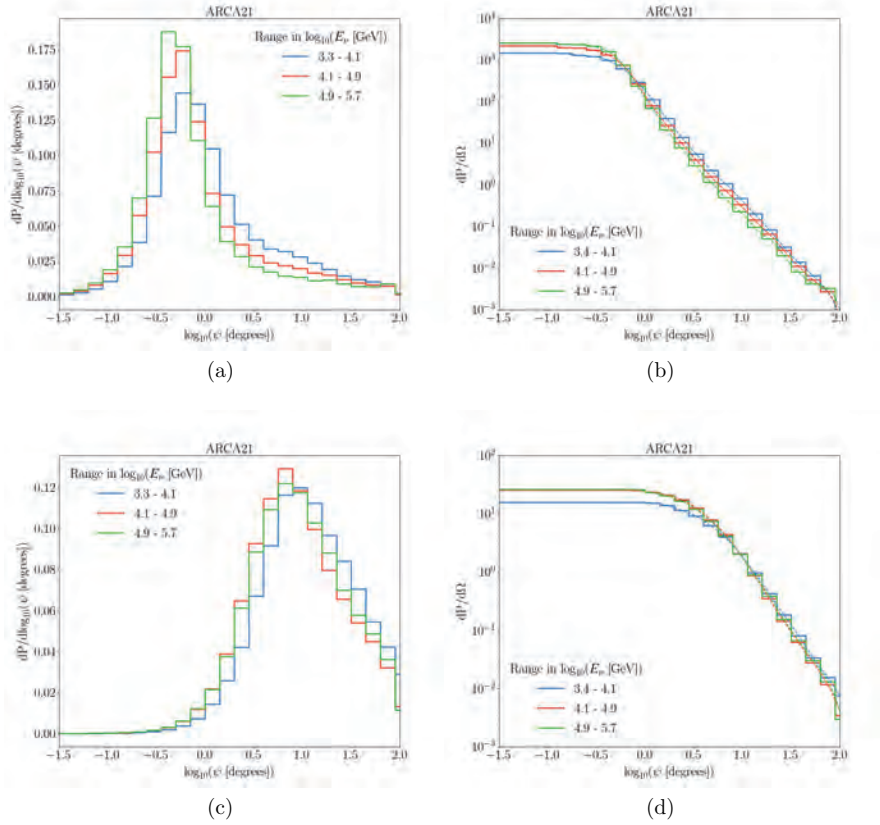

Figure 6.16: Distributions of $dP/d\log(\psi)$ (left) and $dP/d\Omega$ (right) for ARCA21. The top row shows selected ν_μ events selected as track and the bottom row shows ν_e events selected as shower.

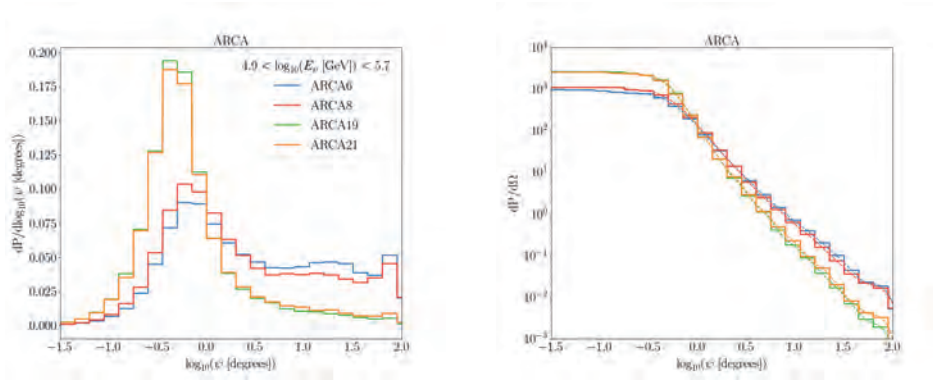

(a) (b)

Figure 6.17: Comparison of distributions of $dP/d\log(\psi)$ (left) and $dP/d\Omega$ (right) for the different ARCA configurations.

The events are binned in reconstructed energy and distance to the source. This leads to expected event distributions for the different ARCA periods and detection channels. An example distribution for tracks and showers with the ARCA21 detector is shown in Figure 6.18. The example distributions assume a source at $\sin(\delta) = 0$ and the exposure of the ARCA21 dataset. The flux model is characterised by spectral index $\gamma = 2.0$ and flux normalisation $\Phi_0 = 1.0 \times 10^{-8}$ GeV^{-1} s^{-1} cm^{-2}.

The expected signal and background distributions are used to generate pseudo-experiments using Poisson statistics. One pseudo-experiment contains a distribution for each detector period and detection channel. The test statistic is calculated using Equation 5.8, which was presented in the previous chapter. Example distributions of the test statistic using tracks only and the subsequent confidence levels are shown in Figure 6.19. The final step of the analysis reverses the scrambling of the data and looks at the event distributions around each candidate source. The test statistic of the combined dataset is used to calculate the p-value. If no significant detection is made, upper limits are established for the normalisation of the neutrino flux. If the observed test statistic of a source is below the median of the test statistic distribution for background only, the upper limit is set to the sensitivity in order to prevent a lower observed limit.

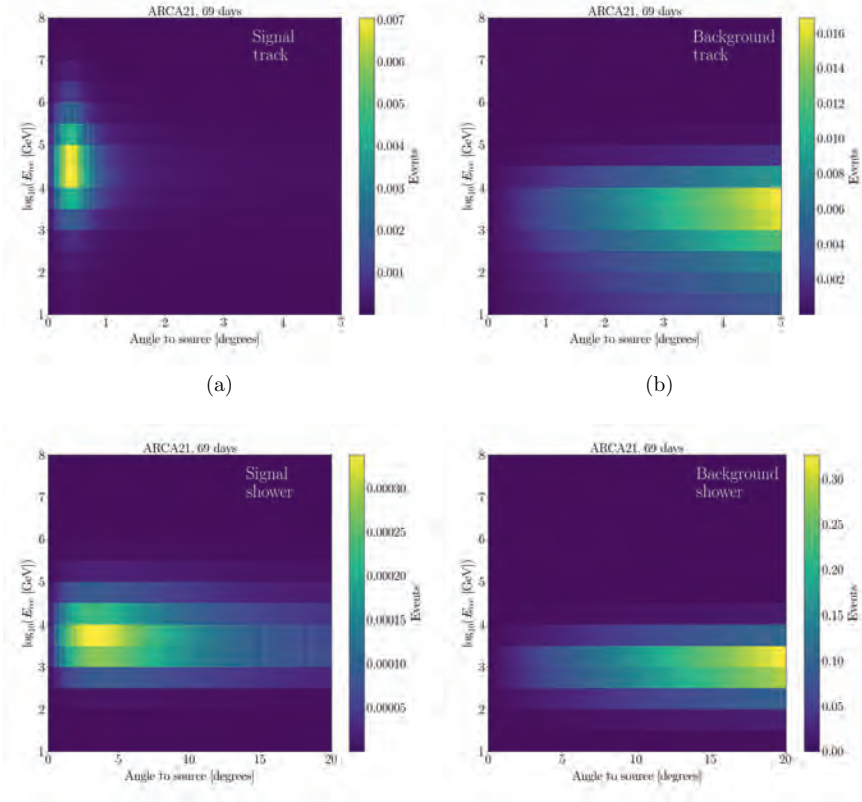

(a) (b)

(c) (d)

Figure 6.18: Expected signal (left) and background (right) distributions as a function of reconstructed energy and angular distance to the source for a point source at $\sin(\delta) = 0$ using the ARCA21 dataset. The top row represents the track channel and the bottom row the shower channel.

6.5 Sensitivity and discovery potential

The generation of pseudo-experiments and resulting confidence levels and p-values are used to study the potential for discovering neutrino point sources. The sensitivity and 3σ discovery flux for a neutrino point source are calculated, which is helpful in optimising the event selection and analysis method before looking at the data. The sensitivity and the 3σ discovery flux are shown in Figure 6.20. These quantities are calculated using tracks only from ARCA6-21, showers only using ARCA19-21, and the combination of both. There is no significant improvement in the sensitivity or discovery flux when the showers are included. This can be attributed to the high background contamination and the poor angular resolution caused by the error in the reconstruction software. For this reason, it was decided to exclude the ARCA19-21 shower data from the final part of this analysis. Work is ongoing to improve the event selection for showers and to study the reconstruction performance after fixing the reconstruction software. This is expected to

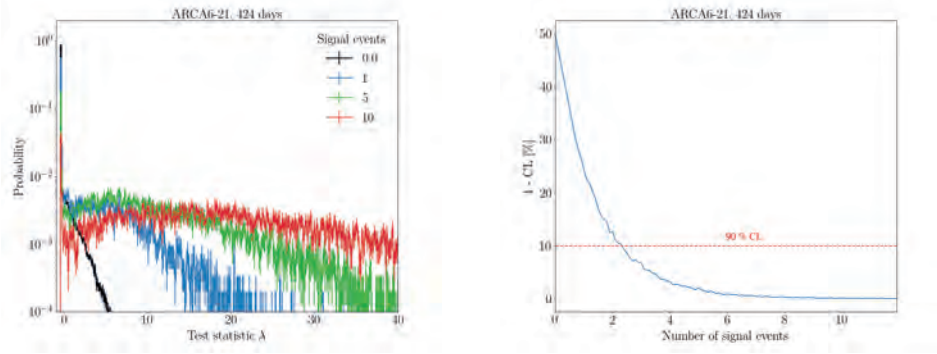

(a) (b)

Figure 6.19: Test statistic distributions (a) and confidence levels (b) from pseudo-experiments using the tracks selected in the ARCA6-21 dataset. These distributions were obtained by assuming a source at $\delta = 0°$.

improve further after the deployment of more detection strings which results in a larger instrumented volume. The resolution is expected to improve to one degree for the full detector as described in the previous chapter and in Reference [111].

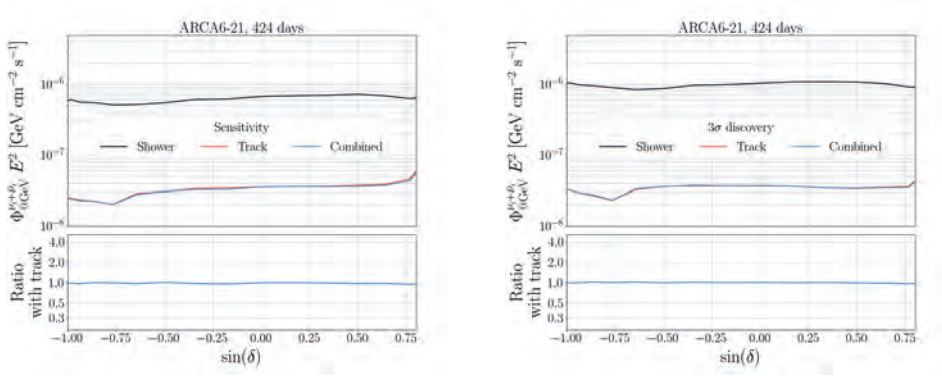

(a) (b)

Figure 6.20: Sensitivity and discovery flux as a function of $\sin(\delta)$ of ARCA6-21 for tracks, showers and the combination of both channels. The bottom panel shows the ratio of the combined results with the track result.

6.5.1 Systematic uncertainties

The significance of any measurement relies on understanding the potential systematic uncertainties that may affect the outcome. This is also valid for ARCA in the search for cosmic neutrino events from candidate sources. One important uncertainty in the detector is caused by the movement of the optical modules due to sea currents. The relative position calibration of the ARCA21 detector already reaches an optical module position resolution of 20 cm [85]. This does not cover a potential tilt of the detector due to slopes on the seabed. A detailed study of this has not yet been conducted, but the dynamic calibrations can give estimates for the resulting uncertainty on the reconstructed zenith angle of events. This is estimated to be 0.3° and will be improved in future work.

The largest challenge in actually achieving the quoted angular resolutions is found in the absolute orientation of the detector. To accomplish this, a system of transponders will be set up, of which the exact positions on the seabed can be determined at the time of installation through the use of the deployment ship's GPS. Possible cross-checks are being envisioned by detecting the acoustic signals from the boat directly with the piezo sensors in the DOMs. Finally, a 'physics' cross-check could be made by detecting the shadow of the Sun and Moon. Cosmic rays are blocked and this results in a deficit of atmospheric muon events from the known direction of the Sun and Moon. This method was already shown for ORCA in [86] and will be repeated for ARCA, but this will not reach the accuracy of 0.06° which is demanded by the accuracy of the track reconstruction at the highest energies. These studies are still ongoing, but the systematic uncertainty can be estimated by looking at the acoustic beacon positions. The measured positions after deployment are compared with their position after calibration and this provides an estimate of the absolute position and orientation of the detector. This uncertainty influences the reconstructed azimuthal angle of events and it is estimated to be 0.4°.

The systematic uncertainties on the direction are taken into account by modifying the point spread functions. For simplicity, it is assumed that both sources of uncertainty influence the zenith and azimuthal angles equally. They are modelled by applying a Gaussian smearing of the point spread function with a standard deviation of $\sqrt{0.4^2 + 0.3^2} = 0.5°$. Future work will improve on this by treating the uncertainties on the zenith and azimuthal angles separately.

Another important systematic uncertainty is the acceptance of the detector. This covers the uncertainties on the water and PMT properties and has been studied in [71, 72]. These preliminary studies result in a conservative 30% uncertainty of the detector acceptance. The signal contribution in the pseudo-experiments is smeared by a Gaussian function to account for this uncertainty. The sensitivity and 3σ discovery flux of a neutrino point source with and without systematics is shown in Figure 6.21.

6.6 Results: the neutrino sky with ARCA6-21

There are on average 31 events observed inside the 5 degree cone around each candidate source for the combined ARCA6-21 dataset. Skymaps of the ARCA6-21 datasets are shown in Figure 6.22. The p-value is computed for each source to determine whether or not the candidate is significantly detected. All candidate sources are consistent with a background-only hypothesis. For the $E^{-2.0}$ spectrum the most signal-like source is the active galactic nucleus J1512-0905 at right ascension 228.21°, declination −9.10° with a

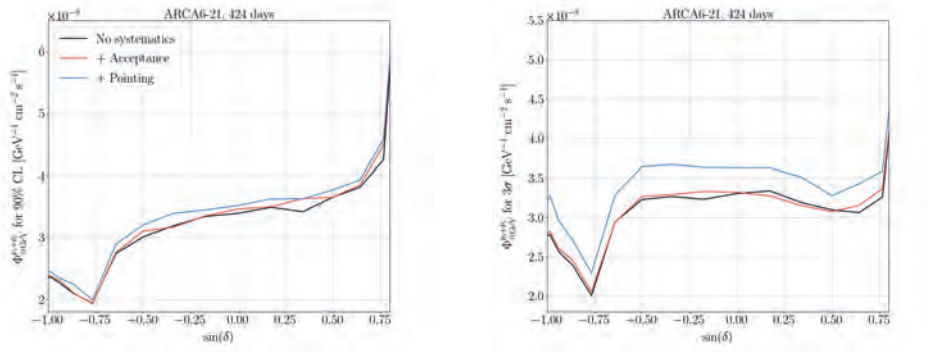

(a) (b)

Figure 6.21: Sensitivity (a) and discovery flux (b) of ARCA6-21 for tracks only without systematics and after including the Gaussian smearing and the systematic uncertainty on the acceptance.

pre-trial p-value of 0.011. This p-value has to be corrected for the number of trials in the analysis. The probability to find the highest test statistic $\lambda_{\text{obs}}^{\text{max}}$ from one or more of the candidate sources considering only background is computed using

$$\text{Post-trial p-value} = 1 - \prod_{\text{sources}} \left(1 - P(\lambda > \lambda_{\text{obs}}^{\text{max}} | \lambda(\mu = 0))\right). \tag{6.2}$$

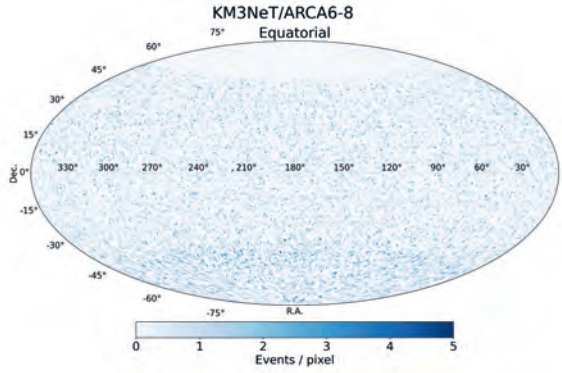

(a)

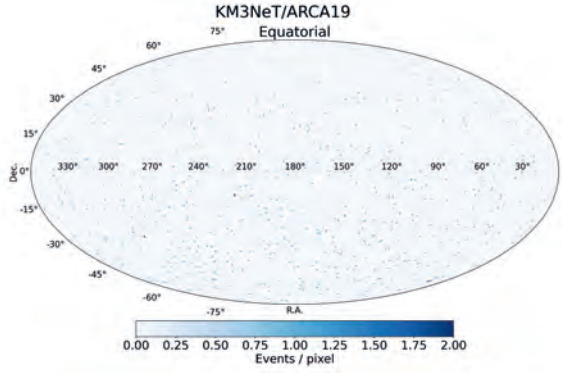

(b)

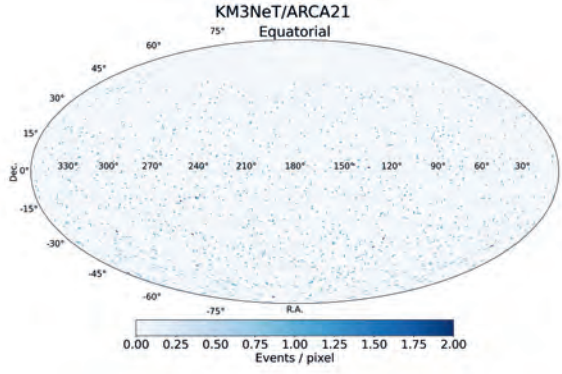

(c)

Figure 6.22: Skymaps of selected events of the ARCA6-8 (a), ARCA19 (b) and ARCA21 (c) datasets. The skymaps are generated using HEALPix [112].

This calculation does not include the trials by testing different flux models, which is 2 ($\gamma = 2.0, 2.5$) for most sources and 3 for NGC 1068 ($\gamma = 2.0, 2.5, 3.2$). The resulting post-trial p-value is 0.66. A summary of the top five lowest p-values is given in Table 6.8.

Name	δ	Fitted signal events	λ	Observed limit on the number of signal events	Flux limit [GeV^{-1} s^{-1} cm^{-1}] $\times 10^{-8}$	P-value
J1512-0905	-9°5'60"	2.049	3.144	6.348	8.09	0.011
J0750+1231	12°31'12"	1.475	2.345	5.567	7.79	0.018
Mkn 421	38°12'36"	1.657	1.167	4.760	7.56	0.038
PKS 0215+015	1°45'0"	1.467	0.860	5.095	6.78	0.056
IC 443	22°30'0"	0.799	0.180	4.378	6.32	0.077

Table 6.8: Summary of the top five most signal-like sources in the E^{-2} analysis.

The $E^{-2.5}$ spectrum analysis also has the J1512-0905 source with the lowest pre-trial p-value. The source with the highest test statistic is the blazar Mkn 421 at right ascension 166.11° and declination 38.21° with a pre-trial p-value of 0.020 and a post-trial p-value of 0.56. This blazar stands among the nearest to Earth and is known for its bright emission of X-rays and gamma rays [113]. A summary of the top five sources is shown in Table 6.9.

Name	δ	Fitted signal events	λ	Observed limit on the number of signal events	Flux limit [GeV^{-1} s^{-1} cm^{-1}] $\times 10^{-5}$	P-value
J1512-0905	-9°5'60"	2.930	-0.654	8.941	2.10	0.010
J0750+1231	12°31'12"	1.820	-0.618	7.532	2.27	0.018
Mkn 421	38°12'36"	2.769	0.162	6.371	2.81	0.020
PKS 0215+015	1°45'0"	2.882	-1.542	7.335	1.93	0.025
NGC 253	-25°17'24"	3.005	-2.869	7.918	1.63	0.032

Table 6.9: Summary of the top five most signal-like sources in the $E^{-2.5}$ analysis.

The softer $E^{-3.2}$ spectrum was only used to study NGC 1068. This active galactic nucleus is located at right ascension 40.7° and declination $-0.01°$ with a pre-trial p-value of 0.98. The post-trial p-value is identical because it was the only source studied for this flux model.

Since there is no significant detection for any of the candidate sources, upper limits on the flux are established. The sensitivity and upper limits of the candidate sources are shown in Figure 6.23. Some candidate source limits appear to be lower than the sensitivity, but this is due to interpolation of the sensitivity between the studied declinations.

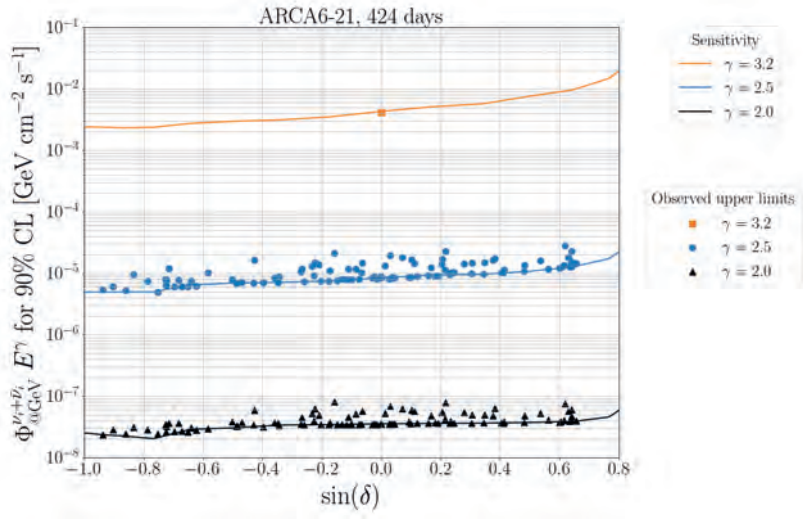

Figure 6.23: Upper limits and sensitivity for the ARCA6-21 point source analysis using 424 days of data. The $\gamma = 2.0$ and 2.5 analyses show the upper limits of 101 sources while the $\gamma = 3.2$ analysis looked solely at NGC 1068.

The ARCA6-21 observed limits and sensitivities for the E^{-2} spectrum are shown in Figure 6.24 for different detectors. The limits and sensitivities are compared with the IceCube integrated point source result with 10 years of data [99], the full ANTARES dataset [97] and the expected sensitivity of the full ARCA detector [111]. The first ARCA point source analysis used three months of data with 6 detection strings followed by the ARCA6-8 analysis, which yielded a factor 2 improvement [68]. This work presents another factor three improvement which is a prime example of the power of a larger detector. The reduced atmospheric muon background and the improved angular resolution greatly improves the sensitivity. This is expected to accelerate even further due to the recent deployment of another 7 detection strings and planned deployment for September 2024. The sensitivity of ANTARES can be matched in the near future allowing ARCA to probe the Southern Sky where IceCube is less sensitive due to their detector location in the Southern Hemisphere. The recent observation of the Galactic plane by the IceCube Collaboration [44] foreshadows discoveries by ARCA in this region. The improving angular resolution of ARCA will help to distinguish diffuse neutrino emission from point sources which will be key in understanding cosmic ray acceleration in our galaxy.

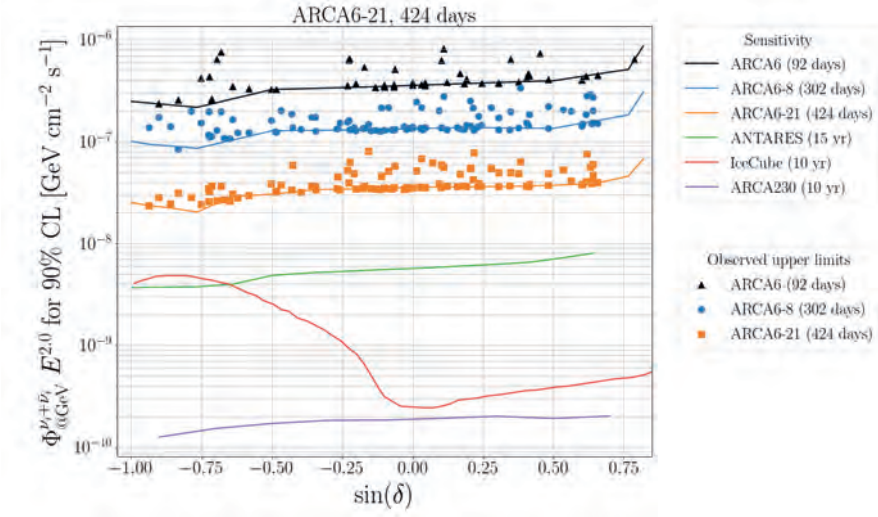

Figure 6.24: Comparison of the observed limits and sensitivities on the $\gamma = 2.0$ neutrino flux for the ARCA6-21 analysis as a function of declination. The results are compared with earlier presented results of the full ANTARES dataset [97], 10 years of IceCube data [99] and the full ARCA sensitivity [111].

Chapter 7

Double cascade reconstruction

Published in "High-energy reconstruction for single and double cascades using the KM3NeT detector". Proceedings of Science (ICRC2021), no. 1089, 2021. [94].

The standard KM3NeT reconstruction algorithms focus on two detection channels: track signatures from muons and shower signatures from hadronic and electromagnetic cascades. This chapter covers a novel reconstruction algorithm focused on double cascade signatures which are produced by tau neutrinos as described in Chapter 2. The tau lepton has a mean lifetime of 2.9×10^{-13} s and it decays into hadrons and leptons [67]. The branching ratio to an electron or hadrons is 0.83 resulting in another shower-like signature as shown in Figure 7.1. Due to time dilation, the showers are spaced approximately 5 cm per TeV. This distance represents the travelling length of the tau, referred to as the tau length throughout this chapter.

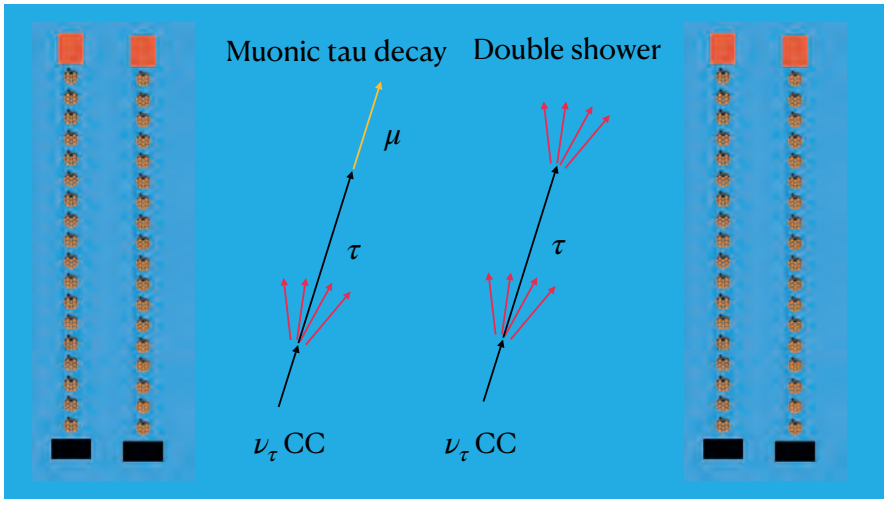

Figure 7.1: Event signatures for ν_τ CC interactions. The produced tau lepton either decays into a muon (left) or into an electron or hadrons (right) producing a shower-like signature.

The reconstruction algorithm evaluates a double shower model by analysing the hit times associated with each event, aiming to determine the tau length, the division of energy between both showers and an improved estimation of the direction of the interacting neutrino. The enhanced direction resolution arises from the *lever-arm effect*, caused by

the displacement of the showers. This feature is more evident in the reconstruction of tracks, where light is emitted over long distances in the detector. The reconstruction algorithm consists of four stages:

1. Default ARCA shower reconstruction: Aashowerfit
2. Tau length prefit
3. Double cascade full fit
4. Energy asymmetry fit

The single shower reconstruction provides an estimate of the direction and a vertex close to one of the two cascades. The tau length prefit searches for a second shower along the estimated direction. The process proceeds with a full event fit, allowing all parameters to vary freely. The final step determines the division of energy between the two showers.

7.1 Event selection

The development and characterisation of the reconstruction chain was carried out using a sample of simulated ν_τ and $\bar{\nu}_\tau$ CC events where the τ decays into hadrons or an electron (ν_τ CC shower) for the full ARCA detector. The algorithm has significant computational costs as it relies on a probability density function (PDF) with five dimensions to characterise the expected photons from a shower. Hence, an event selection was implemented to pick out potentially interesting events, simultaneously reducing the volume of processed events. The event selection process excludes events that are not contained, which are anticipated to be poorly reconstructed, along with low-energy events where the tau travel distance is too short to differentiate from single showers from ν_e CC interactions. The selection criteria are based on the output of the track and shower reconstruction, which are applied to all events as part of the standard procedure for the processing of data and simulations.

The selection criteria for applying the reconstruction are:

- Contained shower reconstruction vertex
  - $x^2_{\text{shower}} + y^2_{\text{shower}} = R_{\text{shower}} < 460$ m,
  - $70 \text{ m} < z_{\text{shower}} < 600$ m,
- Contained track reconstruction vertex
  - $x^2_{\text{track}} + y^2_{\text{track}} = R_{\text{track}} < 460$ m,
  - $70 \text{ m} < z_{\text{track}} < 600$ m,
- $E_{\text{shower}} > 20$ TeV,

where x, y, z are the reconstructed vertex positions coordinates and E_{shower} is the reconstructed shower energy. The detector is centered at $x, y = 0$ and $z = 0$ represents the seafloor. The vertex requirements guarantee contained events, enhancing reconstruction performance and the capability to differentiate signal events from atmospheric muon background events.

The reconstructed energy requirement rejects events with a very short tau length that would otherwise be indistinguishable from single showers. The tau length, true neutrino

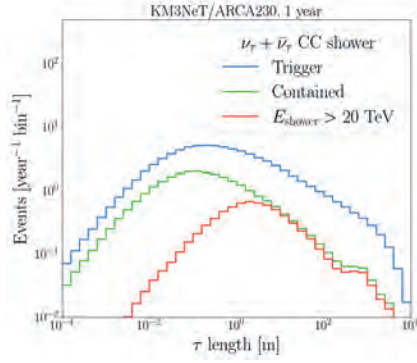

(a)

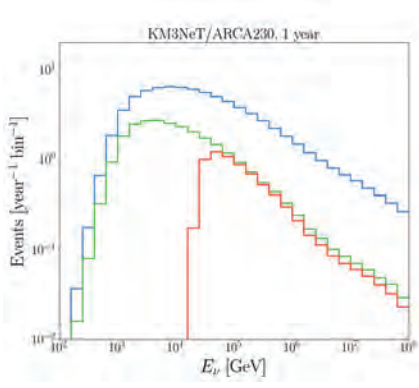

(b)

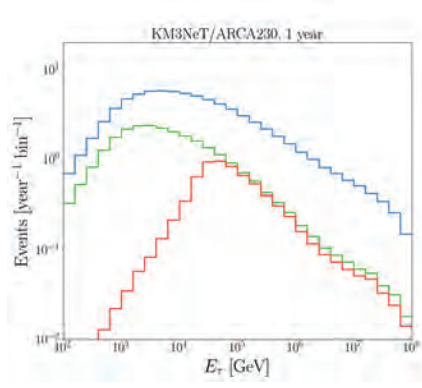

(c)

Figure 7.2: Tau length (a), true neutrino (b) and tau (c) energy distributions for ν_τ CC shower events using the full ARCA detector.

and tau lepton energy are shown in Figure 7.2 for the different selection requirements. All distributions are weighted with the same cosmic neutrino flux defined in Chapter 5.

In certain distributions of this chapter, an extra selection criterion on simulated quantities requires the containment of both the neutrino interaction and the tau decay vertex, which is denoted by *contained* ν, τ.

7.2 Single cascade reconstruction on double cascades

The Aashowerfit reconstruction algorithm for single showers is the first step in the reconstruction of double showers from simulated ν_τ CC shower events. The output from the procedure gives an estimate for the shower energy and direction, alongside a single vertex position and time. The performance of the vertex position fit is decomposed into a longitudinal ($D_\parallel$) and perpendicular component ($D_\perp$) with respect to the neutrino direction, as illustrated in Figure 4.6. The distribution of $D_\perp$ of the ν_τ CC shower sample can be seen in Figure 7.3 for all reconstructed events. The median and 68% quantiles are $0.4^{+0.3}_{-0.2}$

m.

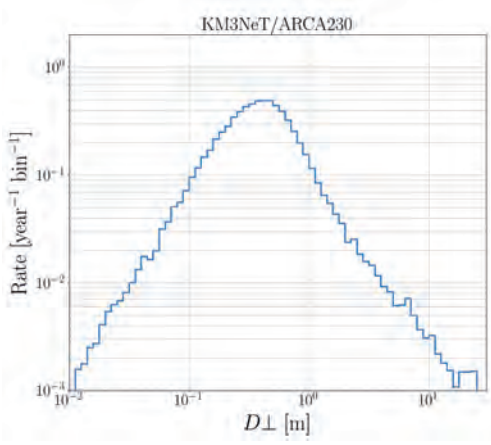

Figure 7.3: Perpendicular position deviation of the Aashowerfit vertex fit for all reconstructed ν_τ and $\bar{\nu}_\tau$ CC shower events that are reconstructed.

The longitudinal position deviation with respect to the neutrino vertex is divided by the tau length, which is shown in Figure 7.4a. The two peaks correspond to Aashowerfit positioning the vertex either at the neutrino interaction vertex (0) or at the tau decay vertex (1). When the tau length is less than a few meters, Aashowerfit fits the vertex ahead of both cascades, due to the elongated light profile of high-energy showers. This leads to the tail of events where the ratio $D_\parallel/\tau$ length exceeds 3 and is shown in Figure 7.4b.

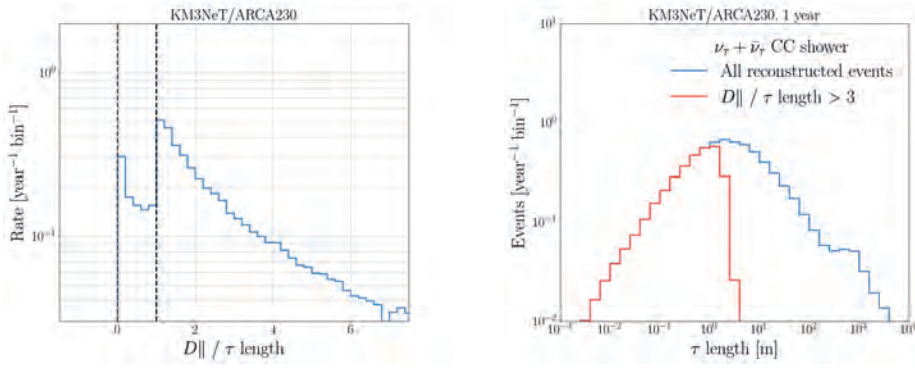

(a) (b)

Figure 7.4: Ratio of longitudinal position deviation and tau length of the Aashowerfit vertex fit for all reconstructed ν_τ and $\bar{\nu}_\tau$ CC shower events (a). The dotted line at zero represents the position of the neutrino interaction vertex, while the line at 1 covers the position of the tau decay vertex. Event rate as a function of the τ length for all reconstructed events and for events with $D_\parallel/\tau > 3$ (b).

The direction resolution of Aashowerfit for simulated and selected ν_τ CC shower events is shown in Figure 7.5. The median and 68% quantiles of the angular resolution are $2.0^{+1.7\circ}_{-1.1}$.

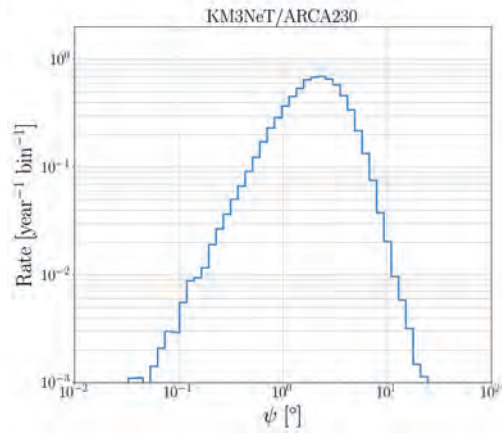

Figure 7.5: Angular deviation of Aashowerfit for all reconstructed ν_τ CC shower events.

The energy reconstruction performance is shown in Figure 7.6 for all reconstructed events and for events where both the neutrino interaction vertex and the tau decay vertex are contained. The reconstructed energy is divided by the visible energy in each event, which is the sum of the energies of particles that emit light. The median and 68% quantiles of both distributions is $0.98^{+0.06}_{-0.07}$, but the containment criterion rejects events where the reconstructed energy is much lower than the true visible energy.

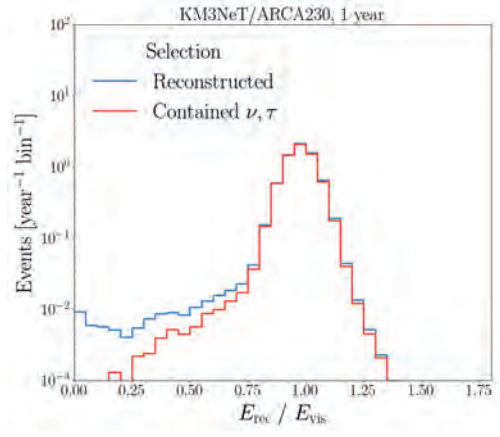

Figure 7.6: Ratio reconstructed energy and visible energy of Aashowerfit for all reconstructed ν_τ CC shower events (blue), and events where both the neutrino interaction vertex and the tau decay vertex are contained (red).

In summary, the Aashowerfit algorithm offers an estimate of the direction and position of either the first or second shower. This enables scanning along the estimated direction to locate the other shower. The tau length prefit facilitates this and obtains an estimate of the neutrino interaction vertex and tau decay vertex.

7.3 Tau length prefit

The tau length prefit conducts a likelihood scan along the direction estimation provided by Aashowerfit. All hits within a cylinder surrounding the Aashowerfit direction are selected

for this purpose, with the cylinder having a radius of 300 m and a height covering the borders of the instrumented volume.

As outlined in Section 4.4, the KM3NeT detector only provides accurate timing information on the first hit on a PMT. Two photons closely spaced in time will be combined into one hit with the time of the first hit and with an increased ToT. The presence of random background hits requires a time window in which hits are selected that starts briefly after the neutrino interaction, in order to maximise the number of first hits from the neutrino interaction instead of background hits.

The single shower reconstruction step provides an estimate for the time of one of the two showers, but it is not given that this shower resulted from the initial neutrino interaction. Therefore the event starting time remains unknown, leading to the utilisation of all recorded hits in the event to derive the estimate for the neutrino interaction and tau decay vertex. This time window is approximately 3.8 μs for the ARCA21 detector and 5.7 μs for the full detector. The subsequent step will have access to a good estimate of the event starting time and will use the first hits to attain the most precise result.

The following likelihood function is maximised:

$$\mathcal{L} = \prod_{\text{all hits}} \mathrm{P}_{\text{hit}} = \prod_{\text{all hits}} 1 - \mathrm{P}_{\text{no hit}} \tag{7.1}$$

$$\mathrm{P}_{\text{no hit}} = \exp[-n_1(\bar{x}, \Delta t) - n_2(\bar{x}, \Delta t) - R_{\text{bg}}] \tag{7.2}$$

$$\bar{x} = (E, D, \beta, \theta_{\text{PMT}}, \phi_{\text{PMT}}) \tag{7.3}$$

where R_{bg} is the expected background rate and n_i is the expected photon density per ns due to the first or second cascade, which is obtained from the PDF. The PDF parameters $\bar{x}$ are the same as described in Section 4.4.

The algorithm assumes two cascades with equal energy at the Aashowerfit vertex and proceeds to vary the position and time of both cascades along the Aashowerfit direction. The cascades are colinear and separated by the speed of light due to the highly relativistic kinematics of the tau lepton. The likelihood is maximised while varying two free variables: x_1 and x_2. They represent two offsets from the Aashowerfit vertex along the Aashowerfit direction. The time of the corresponding vertices ($t_{1,2}$) is calculated by modifying the fitted time of Aashowerfit (t_{shower}) using

$$t_{1,2} = t_{\text{shower}} + \frac{x_{1,2}}{c}. \tag{7.4}$$

The longitudinal light emission profile of Figure 2.3 is used to account for the elongated shape of cascades. The expected number of hits is sampled along the emission profile in order to calculate the integrated number of hits. Sampling points are chosen at positions that mark equal light yield contributions to the cascade. Increasing the number of sampling points enhances the model description of the shower but entails additional computational resources. More samples, in particular, improve the resolution of the vertex position, consequently enhancing the angular resolution of the event through the lever-arm effect. The double cascade reconstruction employs three sampling points for each cascade, striking a balance between computing resources and precision. This seems rather low, but improves upon the point-like emission model for the traditional single cascade reconstruction.

The tau length prefit results in an estimate of x_1 and x_2 which is translated to the neutrino interaction vertex and the tau decay vertex position.

7.4 Double cascade full fit

The starting values for the full event fit are derived from the single shower reconstruction and tau length prefit. This process involves simultaneously fitting two showers using the timing information of the first hits. The procedure obtains an estimate for the following free parameters:

- Neutrino interaction vertex (x,y,z,t)
- Event direction (θ, ϕ)
- Tau length (l_τ)
- Energy asymmetry $(\frac{\mathrm{E}_1-\mathrm{E}_2}{\mathrm{E}_1+\mathrm{E}_2})$.

The total energy remains constant at the value supplied by Aashowerfit, as the timing information utilised has limited sensitivity to the total energy of the shower. Aashowerfit covers the total energy estimate, as shown in Figure 7.6, and the double cascade reconstruction specifically addresses how the energy is distributed between the two cascades, employing energy asymmetry. The cascades are presumed to be colinear, and their collective direction is determined through θ and ϕ. The position and time of the tau decay vertex are constrained by the direction and travelling length of the tau (l_τ), assuming the tau lepton travels at the speed of light.

The likelihood function that is maximised is defined as

$$\mathcal{L}^{\mathrm{S+B}} = \sum_{\text{1st hits}} P_{\text{1st}}^{\mathrm{S+B}}(\bar{x}) \tag{7.5}$$

where $P_{\text{1st}}^{\mathrm{S+B}}(\bar{x})$ is the probability density function of the first hit time from background or due to the first or second cascade. This definition is similar to the definition of the track reconstruction in Equation 4.4, but it contains a signal contribution from two showers. The probability density function for the double cascade reconstruction is defined as

$$P_{\text{1st}}^{\mathrm{S+B}}(\bar{x}) = \frac{\exp\Big[-N_1(\bar{x}_1,\Delta t) - N_2(\bar{x}_2,\Delta t) - R_{bg}(t-t_{\min})\Big]\Big(n_1(\bar{x}_2,\Delta t) + n_2(\bar{x}_2,\Delta t) + R_{bg}\Big)}{\alpha} \tag{7.6}$$

$$\alpha = \exp[-N_1(\bar{x}_1,\Delta t_{\max}) - N_2(\bar{x}_2,\Delta t_{\max}) - R_{bg}(t_{\max}-t_{\min})] - 1 \tag{7.7}$$

where $n_i(\bar{x}_i,\Delta t)$ is the number of photons per ns at Δt due to cascade i and $N_i(\bar{x}_i,\Delta t)$ integrated number of photons up until Δt. The relative time window is defined by $[t_{\min}, t_{\max}] = [-20, 1900]$ ns and is motivated by Figure 7.7, which shows the time difference of the signal hits with respect to the neutrino interaction vertex time obtained by the tau length prefit. The defined time window encompasses nearly all signal hits, thereby narrowing the full time window that includes all hits and consequently decreasing the number of background hits in the selection process.

The first hits within the indicated time window and a cylinder surrounding the tau length prefit are selected. The 300 m radius is the same as for the hit selection for the tau length

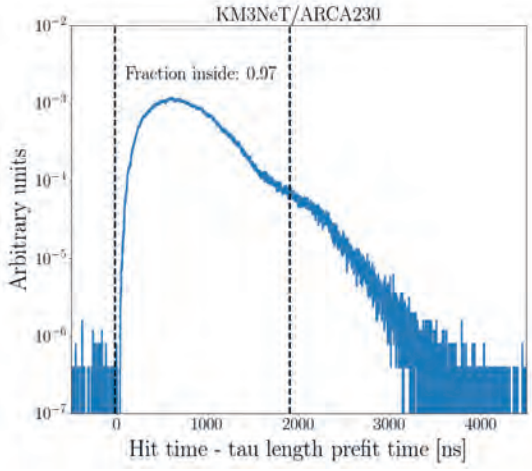

Figure 7.7: Time difference of signal hits with respect to the neutrino interaction vertex time fitted by the tau length prefit.

prefit, but the height of the cylinder spans -150 m from the neutrino interaction vertex and +150 m from the tau decay vertex.

The algorithm also performs a maximisation of the likelihood for a single cascade hypothesis. In this process, it adopts an identical hit selection employed in the final double cascade fit and uses the Aashowerfit prefit as the initial reference. The algorithm then shifts the fitted shower maximum of Aashowerfit to the neutrino vertex position, which serves as the starting point. This result is preserved for future use and can be employed later to differentiate between single and double showers.

7.5 Energy asymmetry fit

The full fit displays a tendency to maintain a starting energy asymmetry of 0, indicating an equal energy distribution for both the first and second shower. This highlights the limitation of relying solely on hit time information rather than incorporating both hit and no-hit data to assess energy. To enhance the performance in assessing energy asymmetry, a subsequent scan and maximisation of the likelihood were conducted after the full fit. However, in this iteration, only the energy asymmetry was retained as a free parameter.

7.6 Performance

The median and 68% quantiles of the angular deviation as a function of the true tau length of the double shower reconstruction is shown in Figure 7.8 for all reconstructed ν_τ CC shower events. The angular deviation of Aashowerfit is approximately 2° for all tau lengths. This performance is comparable with the performance for single cascades from ν_e CC or ν NC interactions. The double cascade reconstruction performance improves with increasing tau length and drops below 1° for lengths larger than 25 m. The decrease in angular deviation is the result of the lever-arm effect. The timing information constrains the vertices of both cascades along the direction of the neutrino and contributes to the improvement of angular deviation.

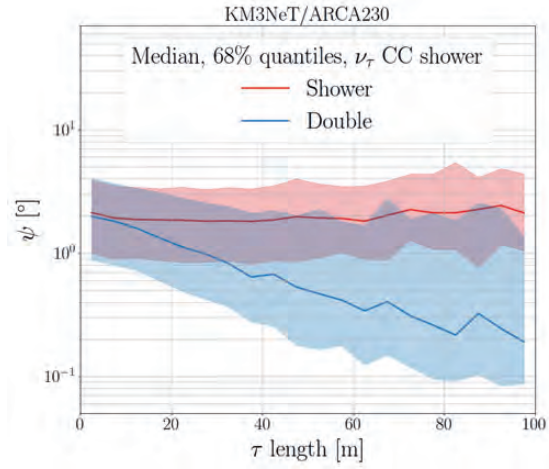

Figure 7.8: Angular deviation as a function of the true tau length for all reconstructed ν_τ CC shower events. The median and 68% quantiles are shown for Aashowerfit and the double cascade reconstruction.

The angular deviation as a function of the neutrino energy is shown in Figure 7.9. The performance for all reconstructed ν_τ CC shower events (a) improves with respect to Aashowerfit up to an energy of 20 PeV. At these energies, the tau lepton can cover substantial distances, leading to the occurrence of the first or second shower outside the detector. The performance for events with a contained neutrino and tau decay vertex (b) exhibits improvement across the entire energy range compared to Aashowerfit. The resolution deteriorates beyond 8 PeV because showers at these energies illuminate the entire detector, causing the tau length prefit to overlook one of the two showers, leading to a diminished angular resolution.

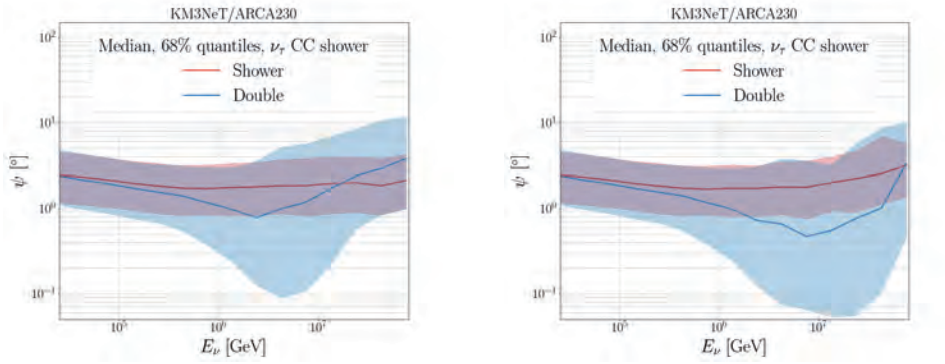

(a) (b)

Figure 7.9: Angular deviation versus true neutrino energy for all reconstructed ν_τ CC shower events (a) and events where both the neutrino interaction vertex and the tau decay vertex are contained (b). The median and 68% quantiles are plotted for Aashowerfit and the double cascade reconstruction.

The reconstructed length error is shown in Figure 7.10. The reconstructed length error

is defined as the reconstructed length minus the true length. For the prefit, the median and 68% quantiles stand at $1.2^{+1.9}_{-1.6}$ m, while for the final fit, they are $0.8^{+1.3}_{-1.5}$ m.

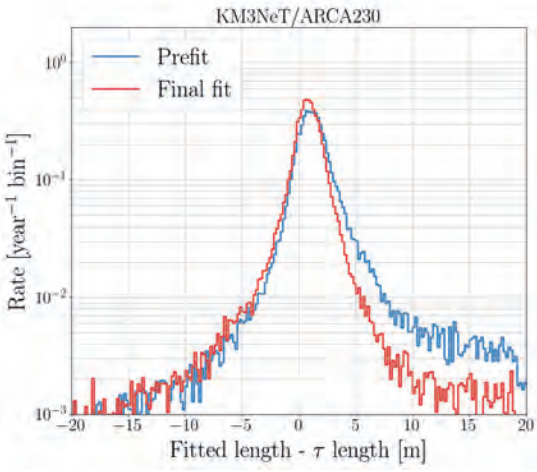

Figure 7.10: Reconstructed length error of the tau length prefit and the full fit for all reconstructed ν_τ CC shower events.

The perpendicular position deviation for both cascades is illustrated in Figure 7.11. The median and 68% quantiles for the neutrino interaction vertex (shower 1) are $0.3^{+0.3}_{-0.2}$ m, and for the tau decay vertex (shower 2), they are $0.2^{+0.2}_{-0.1}$ m. This is a 0.10-0.16 m improvement with respect to the position deviation from Aashowerfit for these events.

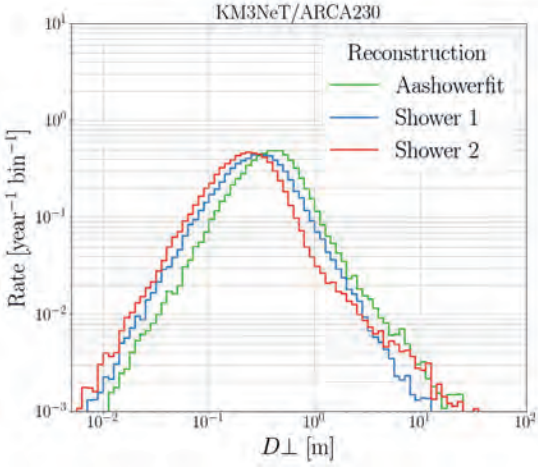

Figure 7.11: Perpendicular deviation for the neutrino interaction vertex (shower 1) and tau decay vertex (shower 2) for all reconstructed ν_τ CC shower events. The deviation is compared to the output from Aashowerfit for these events.

Figure 7.12 illustrates the longitudinal position deviation for both cascades. The median and 68% quantiles for the neutrino interaction vertex are $-0.7^{+0.9}_{-0.5}$ m, and for the tau decay vertex, they are $0.4^{+1.1}_{-1.0}$ m. The neutrino interaction vertex is placed before the true vertex, while the tau decay vertex is reconstructed behind the true decay vertex. This can be improved by employing a larger number of samples of the shower elongation profile, alongside additional computational costs.

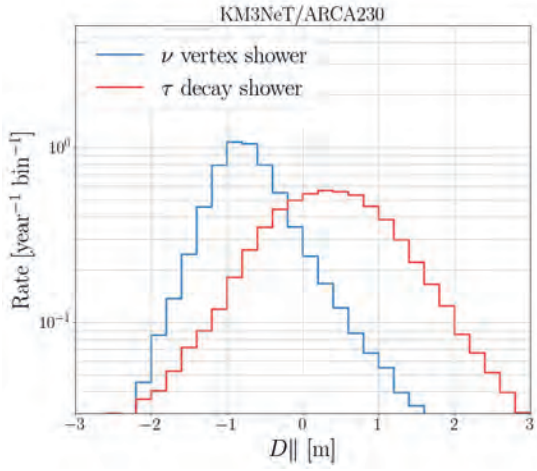

Figure 7.12: Longitudinal deviation for the ν interaction shower vertex and the τ decay shower vertex for all reconstructed ν_τ CC shower events.

The total energy resolution was presented in Figure 7.6. The energy from Aashowerfit is kept constant in the double cascade reconstruction, but the energy asymmetry is a free parameter. The reconstructed energy asymmetry as a function of the true energy asymmetry for all reconstructed (a) and events where both the neutrino interaction vertex and the tau decay vertex are contained (b) is shown in Figure 7.13. There is a population of events with all energy in the first shower (+1) or in the second shower (-1) where the reconstructed asymmetry stays at the starting value of 0. This occurs for small tau lengths and significant shower overlap, making it challenging to differentiate contributions from the individual showers. The performance improves significantly when selecting τ lengths > 20 m as shown in Figure 7.14. All events are reconstructed along the diagonal, except for some events were the true energy asymmetry is -1 and the reconstruction procedure attributes some energy to the first shower.

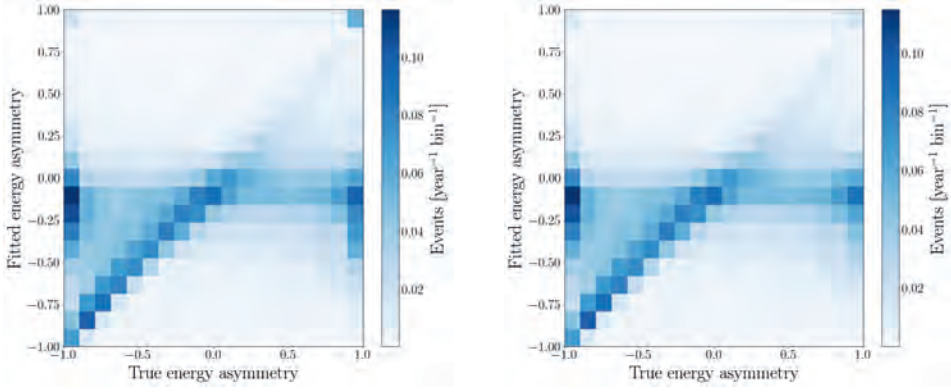

(a) (b)

Figure 7.13: Energy asymmetry for all reconstructed events (a) and events where both the neutrino interaction vertex and the tau decay vertex are contained (b).

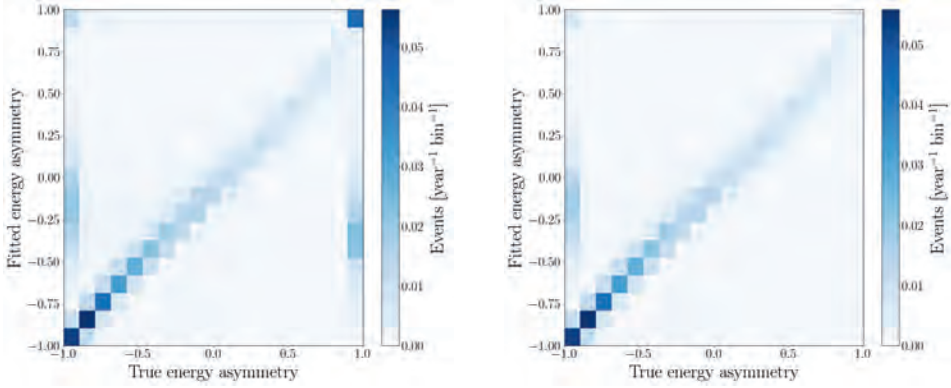

(a) (b)

Figure 7.14: Energy asymmetry for events with τ length > 20 m (a) and events where both the neutrino interaction vertex and the tau decay vertex are contained (b).

The reconstructed energy of the showers, divided by the visible energy, is depicted in Figure 7.15. The median and 68% quantiles for the neutrino interaction shower are $0.9^{+1.9}_{-0.5}$ and $1.0^{+2.6}_{-0.4}$ for the tau decay vertex. This is considerably worse than the total energy resolution shown in Figure 7.6, where the median is $1.0^{+0.1}_{-0.1}$. This underscores the challenge in attributing the detected light emission to the first or second shower. The energy resolution does not change for events where both the neutrino interaction vertex and the tau decay vertex are contained, but improves to $1.0^{+0.6}_{-0.1}$ and $1.00^{+0.2}_{-0.3}$ when selecting events with the τ length > 20 m.

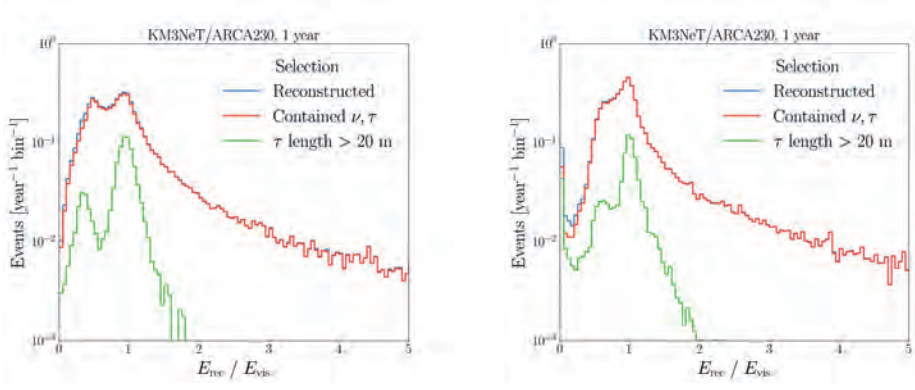

(a) (b)

Figure 7.15: Reconstructed energy divided by the visible energy for the first (a) and second (b) shower for all reconstructed ν_τ CC shower events, for events where both the neutrino interaction vertex and the tau decay vertex are contained and for events where the τ length is larger than 20 m.

This procedure demonstrates a significant improvement in vertex position and direction reconstruction compared to the Belle Starr algorithm presented in Reference [114]. The

Belle Starr algorithm determines the positions of both showers and translates these positions into a direction. The median position resolution is 2 m, resulting in an angular deviation of 1.5-7° for reconstructed τ lengths between 10 and 100 m. Notably, the angular deviation does not improve as a function of the τ length. In contrast, the procedure described in this thesis achieves perpendicular vertex position resolutions of 0.3 m and angular deviations below 1° for τ lengths greater than 25 m.

Chapter 8

Flavour ratio analysis

Discovering new neutrino sources will add crucial insights into the origins and acceleration mechanisms of cosmic rays. The observed energy spectrum will help constrain models for particle acceleration, but there is more that neutrinos can teach us. As discussed in Section 1.4.5, the flavour ratio $\nu_e : \nu_\mu : \nu_\tau$ measured at Earth relates to the flavour ratio at the source, indicating different scenarios for cosmic ray acceleration. This chapter combines the output from the new reconstruction procedure from the previous chapter with the event selections from Chapter 5 in order to study the potential of the full ARCA detector to measure the flavour ratio. The track and shower selections are modified and extended with a double shower observation channel in order to constrain the normalisation of the ν_τ flux. This analysis assumes the diffuse astrophysical neutrino flux from IceCube of ν_μ for all flavours i [42]:

$$\Phi^{\nu_i+\bar{\nu}_i} = \Phi_0 \times \left(\frac{E}{\text{GeV}}\right)^{-2.37}, \tag{8.1}$$

$$\Phi_0 = 1.44 \times 10^{-18}\ \text{GeV}^{-1}\ \text{cm}^{-2}\ \text{s}^{-1}\ \text{sr}^{-1}, \tag{8.2}$$

and studies the performance of the full ARCA detector using two methods: one involving the generation of pseudo-experiments and one using an Asimov dataset assuming Wilks' theorem [53]. Both methods require distributions of expected signal and background rates. The next section outlines the events chosen for the three observation channels (track, shower, double shower) and specifies the variables utilised to represent these channels.

8.1 Event selection

The track and shower samples selected in Chapter 5 contain different relative contributions of neutrino flavours. The track selection was optimised to identify muons from ν_μ CC events and ν_τ CC events where the tau decays into a muon. The shower selection focused on events without a muon and selects ν_e CC, ν NC and ν_τ CC events where the tau decays into a shower. The track selection mainly helps to constrain the normalisation of ν_μ, but the shower channel fails to distinguish ν_e from ν_τ. The track and shower channels are extended with a dedicated double shower selection procedure that maximises the number of astrophysical ν_τ events. Priority is given to the track channel followed by the double shower channel if events are selected in multiple observation channels.

8.1.1 Double shower selection

The selection procedure for the development of the double shower reconstruction algorithm includes a contained shower reconstruction vertex, a contained track reconstruction vertex and a reconstructed shower energy above 20 TeV. This selection was described in Section 7.1. This set of selection requirements is referred to as the Level-1 selection and served as the initial basis for the double shower selection. The event rate per year as a function of the reconstructed energy is shown in Figure 8.1a for events passing the Level-1 selection requirements. The BDT model that was trained to discriminate showers from background in Section 5.1.2 was used to reduce the number of atmospheric muons. Events were selected with shower score > 0.5 as shown in Figure 8.1b.

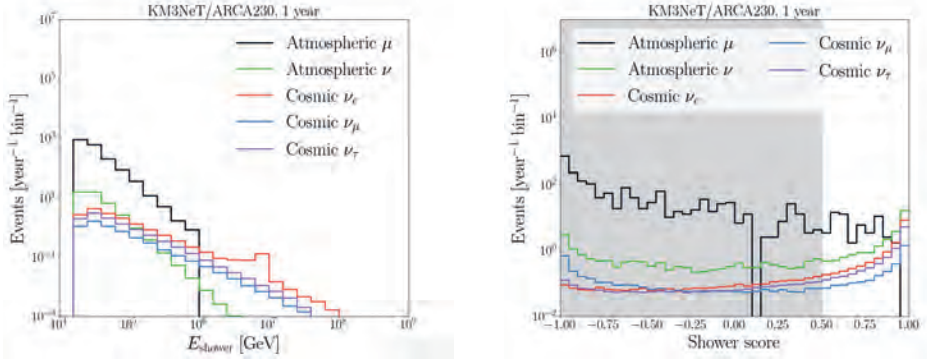

(a) (b)

Figure 8.1: Event rate per year as a function of the reconstructed shower energy (a) and the shower score (b) for events passing the Level-1 selection requirements. Events are selected with shower score > 0.5, as indicated by the shaded area.

The atmospheric background was further reduced by another selection requirement. This requirement is based on the double shower likelihood L_{dc} divided by the number of hits used in the reconstruction $N_{\text{hits}}^{\text{dc}}$. This variable is shown in Figure 8.2 and events were selected using $L_{\text{dc}}/N_{\text{hits}}^{\text{dc}} > -5.6$.

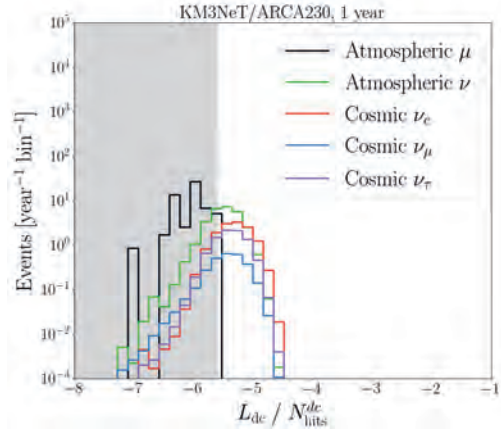

Figure 8.2: Event rate per year as a function of the double shower likelihood divided by the number of hits used in the reconstruction for events passing the Level-1 selection requirements and shower score > 0.5. Events are selected using $L_{\mathrm{dc}}/N^{\mathrm{dc}}_{\mathrm{hits}} > -5.6$, as indicated by the shaded area.

The purity of ν_τ is further improved using the reconstructed tau length. This quantity is shown in Figure 8.3 and events are selected with reconstructed tau length > 3 m.

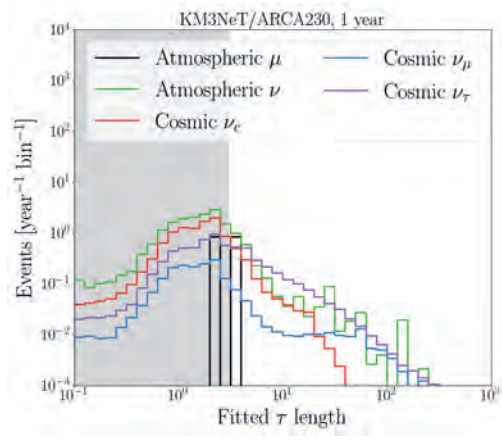

Figure 8.3: Event rate per year as a function of the reconstructed tau length for events passing the Level-1 selection requirements, shower score > 0.5 and $L_{\mathrm{dc}}/N^{\mathrm{dc}}_{\mathrm{hits}} > -5.6$. Events are selected with reconstructed τ length > 3 m, as indicated by the shaded area.

The variable to represent the double shower channel in the determination of the flavour ratio is the reconstructed single shower energy and the distribution is shown in Figure 8.4. The number of events per year for the double shower channel is shown in Table 8.1. The number of simulated events for the remaining atmospheric muons is very limited, as the final events are confined to a single bin. This implies that the precision of the atmospheric muon background estimate is inadequate, which could affect the findings discussed in the remainder of this chapter. Future efforts should extend the simulations while focusing on atmospheric muons events that mimic double shower events.

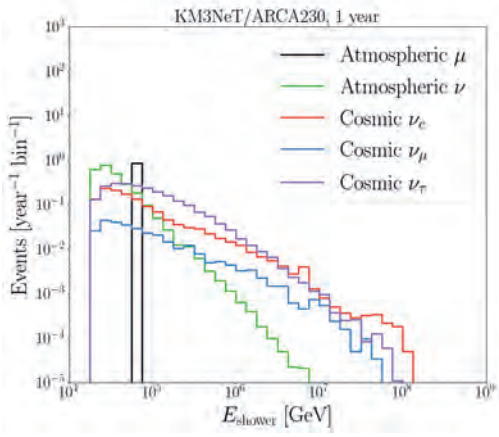

Figure 8.4: Event rate per year as a function of the reconstructed single shower energy for events that pass the double shower selection requirements.

8.1.2 Updated track and single shower selections

The basic selection criteria for tracks and showers using the full ARCA detector were described in Chapter 5. These selections were updated with additional reconstructed energy requirements. This increases the relative contribution from cosmic neutrinos in the data samples. The applied criterion for the track selection is $E_{\text{track}} > 10$ TeV and $E_{\text{shower}} > 10$ TeV for the shower selection.

The containment criteria for the shower channel:

- $Z_{\text{track}} < 650$ m,
- $Z_{\text{shower}} < 650$ m,

have been extended with the following more stringent containment requirements:

- $R_{\text{track}} = \sqrt{x^2_{\text{track}} + y^2_{\text{track}}} < 410$ m,
- $R_{\text{shower}} = \sqrt{x^2_{\text{shower}} + y^2_{\text{shower}}} < 410$ m.

in order to reduce the atmospheric muon background.

The final event rates as a function of the reconstructed energy are shown in Figure 8.5. These distributions are input to the flavour ratio analysis described in the following sections. The number of events per year for the ARCA detector is shown in Table 8.1.

Similar to the double cascade channel, the atmospheric muon distributions exhibit an insufficient number of events passing the selection. However, this is not likely to significantly affect the track channel, as the atmospheric muon background falls below that from atmospheric neutrinos at energies above 100 TeV. The lack of events will have a more pronounced impact on the shower channel, where there are no atmospheric muon events at PeV energies. The unexpected absence of events above several hundred TeV is anticipated to resolve with an extension of the simulations. These events might be rare, but could have an impact on the results.

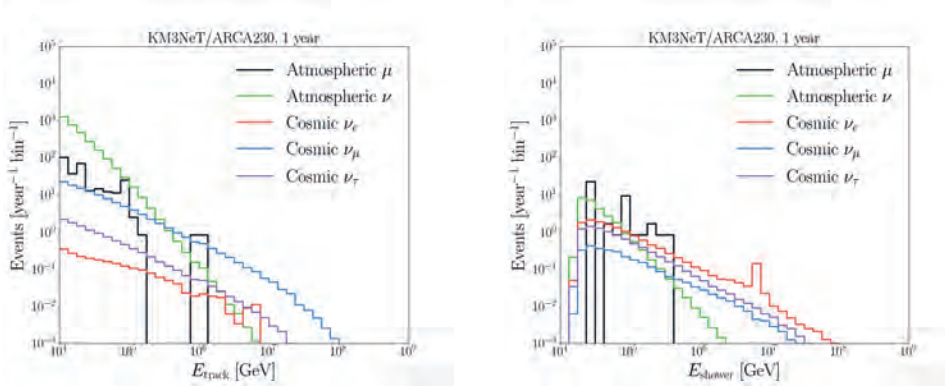

(a) (b)

Figure 8.5: Event rate per year as a function of the reconstructed track (a) and single shower (b) energy for events that pass the updated track and shower selections.

	Track [yr^{-1}]	Shower [yr^{-1}]	Double shower [yr^{-1}]
Atmospheric μ ($>$ 10 TeV)	144	19	0.4
Atmospheric ν	1560	12	1.3
Cosmic ν	63.0	10.6	1.9
Cosmic ν_e	1.1	6.1	0.6
Cosmic ν_μ	56.4	1.3	0.2
Cosmic ν_τ	5.5	3.2	1.1

Table 8.1: Number of events for the full ARCA detector after the updated selections for the track, shower and double shower channels.

8.2 Analysis method

The event distributions of the previous section are input to the study of the potential of the full ARCA detector to measure the flavour ratio of astrophysical neutrinos. The uncertainties of the measurement are obtained from throwing pseudo-experiments, but the final sensitivity is calculated using the Asimov distribution and Wilks' theorem. Both methods are discussed in the following sections.

8.2.1 Pseudo-experiments

The signal and background distributions from Figure 8.4, 8.5a and 8.5b are used to generate pseudo-experiments based on Poisson statistics. A pseudo-experiment contains the distribution for each observation channel. The expected signal S_i^c and background B_i^c for each bin i and channel c are used to generate the observed signal and background for that specific bin. The signal consists of the cosmic neutrinos, while the background is the sum of atmospheric μ and ν backgrounds. Pseudo-experiments are generated for a given set of neutrino flavour ratio and observation period of the full ARCA detector. For each pseudo-experiment, the following likelihood is evaluated

$$\ln \mathcal{L} = \sum_{i \in \text{bins}} \sum_{c \in \text{channels}} N_i^c \log(B_i^c + S_i^c) - B_i^c - S_i^c, \tag{8.3}$$

where N_i^c is the number of observed events in bin i for channel c.

The following likelihood ratio is minimised

$$\lambda = 2 \ln \frac{\mathcal{L}(\text{data}|\mu_{\text{H0}})}{\mathcal{L}(\text{data}|\mu_{\text{H1}})}, \tag{8.4}$$

while varying the alternate hypothesis μ_{H1} and keeping the μ_{H0} hypothesis fixed. The hypothesis contains the diffuse astrophysical neutrino flux normalisation of each neutrino flavour. The minimisation finds the best-fit solution of the flavour ratio for a given pseudo-experiment.

Example distributions of the reconstructed cosmic ν_e, ν_μ, ν_τ and background normalisations are shown in Figure 8.6 for a true flavour ratio of 1:1:1. A measured value of 1 in this Figure indicates the expected normalisation, which corresponds to the quoted IceCube flux normalisation of Equation 8.2 for ν_i.

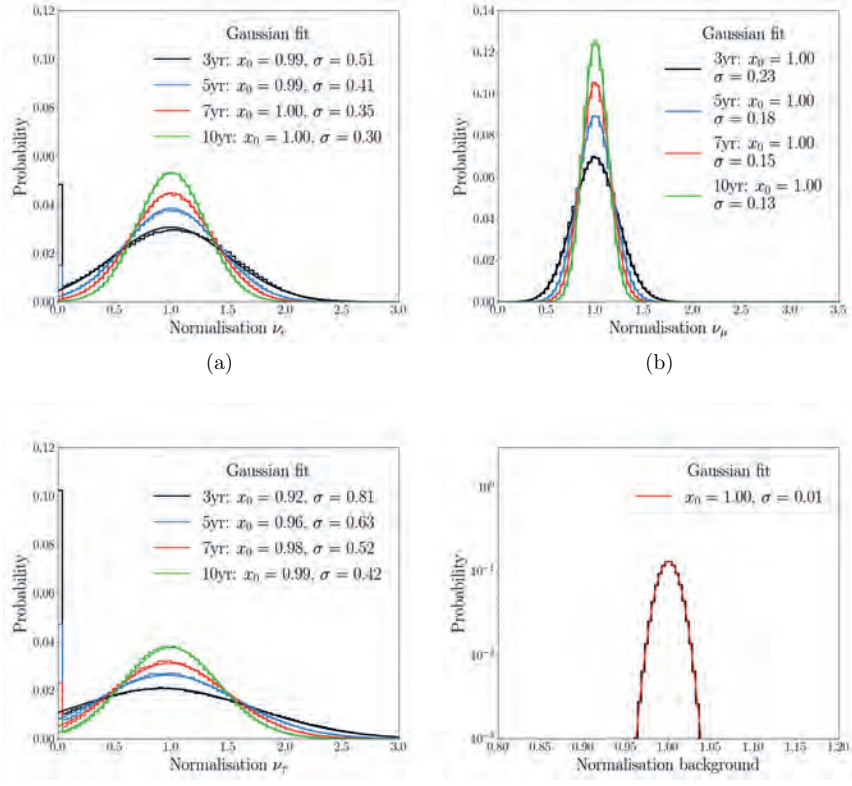

Figure 8.6: Example distributions of the reconstructed cosmic ν_e (a), ν_μ (b) and ν_τ (c) normalisations for varying years of full ARCA operation. The results from the pseudo-experiments are fitted using a Gaussian function, where x_0 is the mean and σ is the standard deviation. The background normalisation (d) is shown for 3 years of full ARCA operation.

The spread on the normalisations represents the uncertainty of the measurement. The normalisation of ν_μ is determined with the smallest spread, followed by ν_e and ν_τ. This is explained by the expected number of events per flavour shown in Table 8.1. The neutrino flavour normalisations are converted to a neutrino flavour ratio by dividing by the total flux normalisation. The spread on the normalisations decreases for increasing years of full ARCA operation, as is shown by the fitted Gaussian functions. The number of pseudo-experiments where the estimated normalisation of ν_e and ν_τ is zero increases for shorter data taking periods, which is not properly modelled by the Gaussian fit.

8.2.2 Asimov analysis

Wilks' theorem states that the distribution of the likelihood-ratio test statistic converges to a χ^2 distribution for a large number of pseudo-experiments. This can be used to calculate the median sensitivity using the Asimov distribution. The Asimov distribution is

a hypothetical dataset where the observed data matches the expectation. The likelihood ratio of Equation 8.4 corresponds to a χ^2 and can be calculated for different hypotheses containing an alternate astrophysical neutrino flavour ratio. The median p-value and confidence level for a given alternate hypothesis are calculated by integrating a χ^2 distribution with two degrees of freedom from the observed χ^2 to infinity. The total neutrino flux normalisation is fixed, leaving two free parameters for the ratios of two of the three neutrino flavours.

One important condition for Wilk's theorem is the absence of boundaries in the parameter space, which is not the case for this analysis. Neutrino flavour ratio contributions can not go below zero and the sum can never exceed one. For this reason, it is important to cross-check the results from the Asimov analysis using pseudo-experiments. One cross-check involves estimating the flavour ratio of the Asimov distribution. This procedure should retrieve the true flavour ratio values and the resulting covariance matrix provides an estimate for the error on the fit parameters. The comparison of the error from 10^6 pseudo-experiments with the Asimov distribution using 10 years of full ARCA observation is shown in Table 8.2 for a flavour ratio of 1:1:1. The errors from the pseudo-experiments are approximately 28% smaller than those obtained from the Asimov distribution. This indicates that the conditions for Wilks' theorem are not entirely satisfied. Consequently, the sensitivities derived from the Asimov distribution discussed in the subsequent sections are conservative when comparing with the method that employs pseudo-experiments. The Asimov method remains preferred because it facilitates a rapid exploration of the parameter space and enables the calculation of confidence level contours.

	Pseudo-experiment	Asimov
Normalisation ν_e	0.30	0.42
Normalisation ν_μ	0.13	0.18
Normalisation ν_τ	0.42	0.58

Table 8.2: Error on the flux normalisation of each neutrino flavour according to 10^6 pseudo-experiments and from the Asimov distribution using 10 years of full ARCA observation.

Limits on the flavour ratio are obtained by iterating over the possible neutrino flavour flux normalisations for a given true normalisation and calculating the χ^2. An example distribution of the χ^2 as a function of the relative ν_e and ν_μ normalisation is shown in Figure 8.7a for 10 years of ARCA operation and flavour ratio 1:1:1. A given normalisation of ν_e and ν_μ automatically determines the normalisation of ν_τ, given that the total normalisation is constant. The minimum is found at $\frac{1}{3}$:$\frac{1}{3}$:$\frac{1}{3}$. The χ^2 is converted to the number of standard deviations in a normal distribution, which is shown in 8.7b. Additionally, the limits for 68% and 90% are indicated.

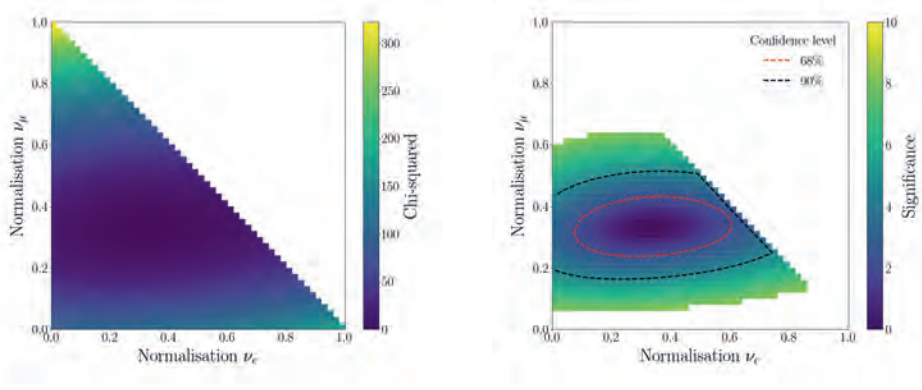

(a) (b)

Figure 8.7: Example distribution of the χ^2 as a function of the ν_e and ν_μ normalisation (a) for 10 years of ARCA operation. Corresponding number of standard deviations and contours (b).

8.3 Equal flavour ratio

The flux normalisation of IceCube from Equation 8.2 was determined for ν_μ, but this analysis assumes an equal contribution from ν_e and ν_τ. The contours from the previous section are illustrated on a ternary graph that displays all three flavour ratios, with the total sum fixed at one. The 68% and 90% contours for 10 years of ARCA operation are shown in Figure 8.8 where the red dot indicates the true flavour ratio of 1:1:1. The contours cover the regions of possible flavour ratios for a given confidence level.

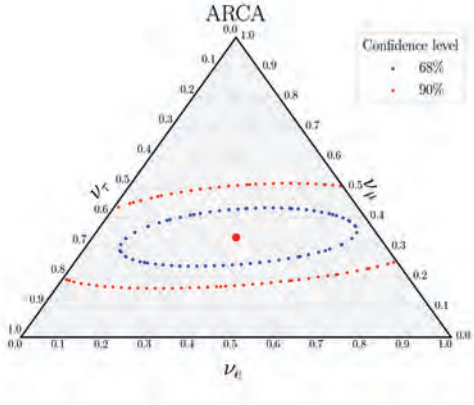

Figure 8.8: The contours for the astrophysical flavour ratio at Earth for a true flavour ratio of 1:1:1 using 10 years of ARCA data. The red dot represents the true flavour ratio and the contours cover the 68% and 90% confidence levels.

The 68% contours for different number of years of ARCA observation are shown in Figure 8.9. The size of the contour shrinks for increasing years of observation, which signifies an improved determination of the flavour ratio.

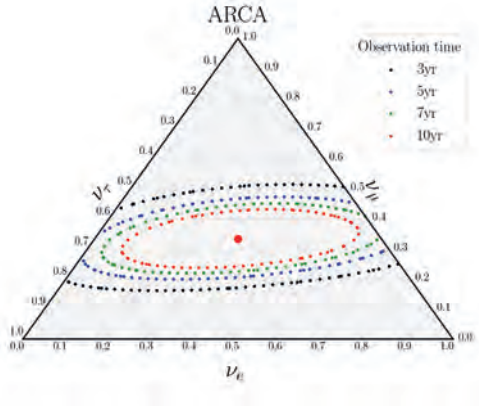

Figure 8.9: The contours for the astrophysical flavour ratio at Earth for a true flavour ratio of 1:1:1 using 3,5,7 and 10 years of ARCA data. The red dot represents the true flavour ratio and the contours cover the 68% confidence levels.

8.4 Impact of the flux intensity

The analysis from the IceCube collaboration estimated the flux normalisation at

$$\Phi_0 = 1.44^{+0.25}_{-0.26} \times 10^{-18}\ \text{GeV}^{-1}\ \text{cm}^{-2}\ \text{s}^{-1}\ \text{sr}^{-1}, \tag{8.5}$$

with an upper bound at +17% and a lower bound at -18% of the central value due to statistical and systematic uncertainties. The analysis was repeated for these bounds and the comparison of the 68% and 90% contours are shown in Figure 8.10 for 10 years of ARCA operation.

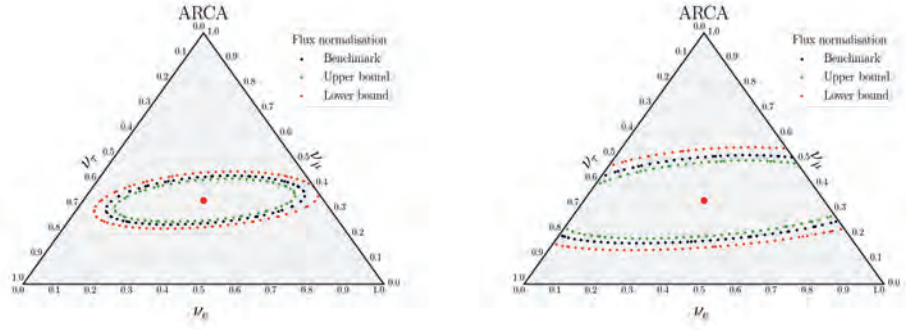

(a) (b)

Figure 8.10: The contours for the astrophysical flavour ratio at Earth for a true flavour ratio of 1:1:1 using 10 years of ARCA data. The red dot represents the true flavour ratio and the contours cover the 68% (a) and 90% (b) confidence levels. The results from the best flux normalisation of IceCube (benchmark) are compared with the upper bound and lower bound due to the statistical and systematic uncertainties.

8.5 Outlook

This chapter showed an estimate of the potential of ARCA to measure the flavour ratio of cosmic neutrinos. The influence of flux intensity on the results is minimal and is expected to decrease further in the future, especially due to the contribution of the ARCA detector in enhancing the flux normalisation measurements conducted by IceCube. Similar effects on the results are expected when studying the systematic uncertainties on the effective area of the detector. The full ARCA study of Chapter 5 varied the effective area with $\pm 5\%$ and $\pm 10\%$ to study the influence of the uncertainty on the PMT quantum efficiency and the water absorption length. These variations exert a smaller effect on the final outcome than the changes of the flux normalisation.

One important systematic uncertainty that is not covered in this analysis is the uncertainty on the muon background. Section 8.1.1 describes the double shower selection and Figure 8.1 shows an abrupt end to the atmospheric muon background for energies above 1 PeV. The lack of simulated events of the muon simulation leads to an underestimation of the muon background at high-energy. A similar trend is observed in both the track and shower selections.

The current selection effectively rejects muons to such an extent that, with the existing simulations, it is not feasible to estimate the muon contribution at high-energy. Consequently, it is assumed that atmospheric neutrinos will predominantly constitute the background. Given the numerous methods available to minimise the background from misreconstructed muons, this assumption is expected to be realistic, although a comprehensive validation can only be achieved by expanding the simulations in the future.

The analysis of the flavour ratio should be continued with the current ARCA detector which currently operates 28 detection lines. The first efforts for a shower selection can be extended with the first search for tau neutrinos. This would allow a similar study as described in this chapter, but with actual data collected by the ARCA detector. One important challenge lies in an improved simulation of the atmospheric muon background. The atmospheric muon events that mimic double shower events are relatively rare and require a separate simulation effort. This effort should increase the statistics of this background which is necessary in the determination of the astrophysical flavour ratio of neutrinos.

Chapter 9

Appendix

9.1 Gold parameter

The gold parameter used in Section 5.1 is inherited from an obsolete shower reconstruction algorithm named Dusj. This variable was calculated at the end of the reconstruction, but can be calculated with the hits and reconstructed vertex of any algorithm. The gold parameter is defined as

$$GP = \frac{1}{N} \sum_{i \in \text{hits}} \frac{1}{\sigma} e^{-\frac{\Delta t^2}{(2\sigma \cdot 1.5)^2}} \tag{9.1}$$

where Δt is the hit time residual, N is the total number of hits and σ the time resolution of a DOM.

9.2 Inertia ratio

The inertia ratio used in Section 5.1 was calculated at the end of the obsolete vertex reconstruction algorithm QStrategy. The hits and reconstructed vertex are used to fill the matrix

$$I^{k,l} = \sum_{i \in \text{hits}} A_i (\delta^{k,l} r_i^2 - r_i^k r_i^l) \tag{9.2}$$

where δ is the delta function, and r_i is the distance of a hit to the reconstructed vertex. The eigenvalues e_i of this matrix are used to calculate the inertia ratio according to

$$I_R = \frac{\min(e_i)}{\sum_i e_i}. \tag{9.3}$$

Linear hit patterns result in values close to 0, while spherical hit patterns approach $\frac{1}{3}$.

9.3 Point source candidates

Table obtained from Reference [68].

Name	Type	Right ascension	Declination	Size [°]	Comment
LMC N132D	SNR/Molec. Cloud	5h 24m 48s	-69°39'0"	0	TeVCat+hadronic
HESS J1356-645	PWN	13h 56m 0s	-64°30'0"	0.2	>0 events in ANTARES
SNR G318.2+00.1	SNR/Molec. Cloud	14h 57m 40.80s	-59°27'36"	0.31	TeVCat+hadronic
IC-hotspot South hemisphere	unknown	23h 20m 48s	-56°30'0"	0	IC most significant Southern hotspot
HESS J1614-518	Shell	16h 14m 9.60s	-51°52'12"	0.23	TeVCat+hadronic
PKS 2005-489	BLL	20h 9m 28.80s	-48°49'12"	0	>0 events in ANTARES
HESS J1640-465	Composite SNR	16h 40m 38.40s	-46°34'12"	0.11	TeVCat+hadronic
RX J0852.0-4622	Shell	8h 52m 0s	-46°22'12"	1	TeVCat+hadronic
HESS J1641-463	unknown	16h 41m 2.40s	-46°17'60"	0	>0 events in ANTARES
VelaX	PWN	8h 35m 0s	-45°36'0"	0.42	>0 events in ANTARES
PKS 0537-441	BLL	5h 38m 50.40s	-44°4'48"	0	>0 events in ANTARES and high radio VLBI max flux
CentaurusA	radio galaxy	13h 25m 26.40s	-43°1'12"	0	>0 events in ANTARES
PKS 1424-418	FSRQ	14h 27m 57.60s	-42°6'36"	0	active PKS in gamma and high radio VLBI max flux
J0106-4034	AGN	1h 6m 45.60s	-40°34'12"	0	High radio VLBI max flux
RX J1713.7-3946	Shell — SNR	17h 13m 26.40s	-39°46'12"	0.65	TeVCat+hadronic
CTB 37A	SNR/Molec. Cloud	17h 14m 14.40s	-38°31'12"	0	TeVCat+hadronic
PKS 1454-354	BLL	14h 57m 26.40s	-35°40'12"	0	>0 events in ANTARES
HESS J1741-302	unknown	17h 41m 0s	-30°11'60"	0	>0 events in ANTARES
J1924-2914	AGN	19h 24m 50.40s	-29°14'24"	0	High radio VLBI max flux
Galactic center	Galactic center	17h 45m 40.80s	-29°0'36"	0	Historical + Highest for ANTARES
J2258-2758	AGN	22h 58m 4.80s	-27°58'12"	0	High radio VLBI max flux
J1625-2527	AGN	16h 25m 48s	-25°27'36"	0	High radio VLBI max flux
NGC 253	Starburst	0h 47m 31.20s	-25°17'24"	0	TeVCat+hadronic
J0457-2324	AGN	4h 57m 2.40s	-23°24'36"	0	High radio VLBI max flux
J1833-210A	AGN	18h 33m 40.80s	-21°3'36"	0	High radio VLBI max flux

Table 9.1: Source candidates obtained from [68].

Name	Type	Right ascension	Declination	Size [°]	Comment
J0836-2016	AGN	8h 36m 38.40s	-20°16'48"	0	High radio VLBI max flux
J1911-2006	AGN	19h 11m 9.60s	-20°7'12"	0	High radio VLBI max flux
J0609-1542	AGN	6h 9m 40.80s	-15°42'36"	0	High radio VLBI max flux
SNR G015.4+00.1	Composite SNR	18h 18m 4.80s	-15°28'12"	0	TeVCat+hadronic
J2158-1501	AGN	21h 58m 7.20s	-15°1'12"	0	High radio VLBI max flux
LHAASO J1825-1326	unknown	18h 25m 48s	-13°26'60"	0	Latest LHAASO observation
QSO 1730-130	Quasar	17h 33m 12s	-13°5'60"	0	>0 events in ANTARES and high radio VLBI max flux
J1337-1257	AGN	13h 37m 40.80s	-12°57'36"	0	High radio VLBI max flux
J2246-1206	AGN	22h 46m 19.20s	-12°6'36"	0	High radio VLBI max flux
PKS 0727-11	Quasar	7h 30m 19.20s	-11°41'60"	0	>0 events in ANTARES and high radio VLBI max flux
TXS 1749-101	radio blazar	17h 52m 36s	-10°11'60"	0	Relevant alert in datataking period ARCA
HESS J1828-099	unknown	18h 28m 57.60s	-9°59'24"	0	>0 events in ANTARES
J1512-0905	AGN	15h 12m 50.40s	-9°5'60"	0	High radio VLBI max flux
J0607-0834	AGN	6h 7m 60s	-8°34'48"	0	High radio VLBI max flux
QSO 2022-077	BLL	20h 25m 36s	-7°35'60"	0	>0 events in ANTARES
RS Ophiuchi	nova	17h 50m 12s	-6°42'36"	0	TeVCat+hadronic
J0006-0623	AGN	0h 6m 14.40s	-6°23'24"	0	High radio VLBI max flux
3C279	Blazar	12h 56m 12s	-5°47'24"	0	>0 events in ANTARES and high radio VLBI max flux
LHAASO J1839-0545	unknown	18h 39m 48s	-5°44'60"	0	Latest LHAASO observation
J2225-0457	AGN	22h 25m 48s	-4°57'0"	0	High radio VLBI max flux
4FGL J0307.8-0419	blazar	3h 7m 48s	-4°19'48"	0	IC alert
PKS 1741-038	radio blazar	17h 44m 0s	-3°49'48"	0	IC alert + high radio VLBI max flux
LHAASO J1843-0338	unknown	18h 42m 60s	-3°38'60"	0	Latest LHAASO observation
J0339-0146	AGN	3h 39m 31.20s	-1°46'48"	0	High radio VLBI max flux

Table 9.1: Source candidates obtained from [68].

Name	Type	Right ascension	Declination	Size [°]	Comment
J0423-0120	AGN	4h 23m 16.80s	-1°20'24"	0	High radio VLBI max flux
J0725-0054	AGN	7h 25m 50.40s	0°55'12"	0	High radio VLBI max flux
LHAASO J1849-0003	unknown	18h 49m 24s	0°3'0"	0	Latest LHAASO observation
NGC 1068	SBG	2h 42m 40.80s	0°0'36"	0.12	Intereresting for IceCube
J2136+0041	AGN	21h 36m 38.40s	0°42'0"	0	High radio VLBI max flux
J1058+0133	AGN	10h 58m 28.80s	1°34'12"	0	High radio VLBI max flux
J0108+0135	AGN	1h 8m 38.40s	1°34'48"	0	High radio VLBI max flux
PKS 0215+015	blazar	2h 17m 48s	1°45'0"	0	IC alert
J1229+0203	AGN	12h 29m 7.20s	2°2'60"	0	High radio VLBI max flux
TXS 0310+022	blazar	3h 13m 12s	2°30'0"	0	IC alert
3C403	radio galaxy	19h 52m 16.80s	2°30'36"	0	Promising from ANTARES
CGCG 420-015	Seyfert	4h 53m 25.44s	4°3'41.76"	0	plocal=2e-4
J0433+0521	AGN	4h 33m 12s	5°20'60"	0	High radio VLBI max flux
TXS 0506+056	BLL	5h 9m 24s	5°42'0"	0	promising from IC, ANTARES + combined
HESS J0632+057	binary	6h 32m 57.60s	5°48'36"	0	promising from IC ANTARES combined
LHAASO J1908+0621	unknown	19h 8m 12s	6°20'60"	0	Latest LHAASO observation
PKS 2145+067	blazar	21h 48m 4.80s	6°57'36"	0	High radio VLBI max flux
W 49B	SNR/Molec. Cloud	19h 11m 7.20s	9°5'24"	0	TeVCat+hadronic
OT 081	BLL	17h 51m 33.60s	9°39'0"	0	>0 events in ANTARES and High radio VLBI..
PKS 1502+106	blazar	15h 4m 24s	10°29'24"	0	brightest flare coincident with IC
J0242+1101	blazar	2h 42m 28.80s	11°1'12"	0	promising from ANTARES
J2232+1143	AGN	22h 32m 36s	11°43'48"	0	High radio VLBI max flux
J0121+1149	AGN	1h 21m 40.80s	11°49'48"	0	High radio VLBI max flux
J1230+1223	AGN	12h 30m 50.40s	12°23'24"	0	High radio VLBI max flux
J0750+1231	AGN	7h 50m 52.80s	12°31'12"	0	High radio VLBI max flux
PKS 1413+135	blazar	14h 16m 7.20s	13°20'60"	0	IC alert

Table 9.1: Source candidates obtained from [68].

Name	Type	Right ascension	Declination	Size [°]	Comment
J0530+1331	AGN	5h 30m 57.60s	13°31'48"	0	High radio VLBI max flux
W 51	SNR/Molec. Cloud	19h 22m 60s	14°8'24"	0.12	TeVCat+hadronic
J2253+1608	AGN	22h 53m 57.60s	16°8'60"	0	High radio VLBI max flux
PKS 0735+178	blazar	7h 38m 7.20s	17°42'36"	0	IC alert
LHAASO J1929+1745	unknown	19h 29m 0s	17°45'0"	0	Latest LHAASO observation
J0854+2006	AGN	8h 54m 48s	20°6'36"	0	High radio VLBI max flux
RGB J2243+203	BLL	22h 43m 55.20s	20°21'0"	0	>0 events in ANTARES
LHAASO J0534+2202	PWN	5h 34m 12s	22°3'0"	0	Latest LHAASO observation
IC 443	Shell	6h 16m 50.40s	22°30'0"	0.16	TeVCat+hadronic
PKS 1424+240	BLL	14h 27m 2.40s	23°47'60"	0	promising from IC
MG3 J225517+2409	blazar/BLL	22h 55m 16.80s	24°11'24"	0	promising from ANTARES
2HWC J1949+244	unknown	19h 49m 40.80s	24°27'36"	1	>0 events in ANTARES
LHAASO J1956+2845	unknown	19h 56m 12s	28°45'0"	0	Latest LHAASO observation
J0237+2848	AGN	2h 37m 52.80s	28°48'0"	0	High radio VLBI max flux
J1310+3220	AGN	13h 10m 28.80s	32°21'0"	0	High radio VLBI max flux
J1613+3412	AGN	16h 13m 40.80s	34°12'36"	0	High radio VLBI max flux
LHAASO J2018+3651	unknown	20h 18m 60s	36°51'0"	0	Latest LHAASO observation
J2015+3710	AGN	20h 15m 28.80s	37°10'48"	0	High radio VLBI max flux
MGRO J2019+37	unknown	20h 19m 60s	37°59'60"	0.75	>0 events in ANTARES
Mkn 421	Superbright blazar	11h 4m 26.40s	38°12'36"	0	nearby γ-ray emiters
J0927+3902	AGN	9h 27m 2.40s	39°2'24"	0	High radio VLBI max flux
NGC 4151	Seyfert 1	12h 10m 31.20s	39°24'36"	0	promising from IC
Mkn 501	Superbright blazar	16h 53m 52.80s	39°45'36"	0	nearby γ-ray emiters
J1642+3948	AGN	16h 42m 60s	39°48'36"	0	High radio VLBI max flux
J0555+3948	AGN	5h 55m 31.20s	39°48'36"	0	High radio VLBI max flux
LHAASO J2032+4102	unknown	20h 32m 12s	41°2'60"	0	Latest LHAASO observation — >0 events in ANTARES

Table 9.1: Source candidates obtained from [68].

Bibliography

[1] V. Hess (translation from A. De Angelis). On the observations of the penetrating radiation during seven balloon flights. *arXiv preprint arXiv:1808.02927*, 2018.

[2] B. Breisky. On its centenary, celebrating a ride that advanced physics. `https://www.nytimes.com/2012/08/07/science/space/when-victor-hess-discovered-cosmic-rays-in-a-hydrogen-balloon.html`, 2012. Accessed: 03-06-2024.

[3] M. Thomson. *Modern particle physics*. Cambridge University Press, 2013.

[4] T. Gaisser et al. *Cosmic rays and particle physics*. Cambridge University Press, 2016.

[5] K. Greisen. End to the cosmic-ray spectrum? *Physical Review Letters*, 16(17):748, 1966.

[6] G. T. Zatsepin and V.A. Kuz'min. Upper limit of the spectrum of cosmic rays. *Soviet Journal of Experimental and Theoretical Physics Letters*, 4:78, 1966.

[7] E. Fermi. On the origin of the cosmic radiation. *Physical Review*, 75(8):1169, 1949.

[8] A.M. Bykov et al. Cosmic ray production in supernovae. *Space Science Reviews*, 214:1–34, 2018.

[9] K.W. Melis. Studying the universe from -3000m N.A.P. 2021. PhD thesis, University of Amsterdam, `https://hdl.handle.net/11245.1/418ff3d6-d028-4891-a5eb-7cd144316e56`.

[10] A. M. Hillas. The origin of ultra-high-energy cosmic rays. *Annual review of astronomy and astrophysics*, 22(1):425–444, 1984.

[11] E.G. Berezhko and H.J. Völk. Spectrum of cosmic rays produced in supernova remnants. *The Astrophysical Journal*, 661(2):L175, 2007.

[12] E.G. Berezhko. Cosmic rays from active galactic nuclei. *The Astrophysical Journal*, 684(2):L69, 2008.

[13] J.K. Becker. High-energy neutrinos in the context of multimessenger astrophysics. *Physics Reports*, 458(4-5):173–246, 2008.

[14] Y. Fukuda et al. Evidence for oscillation of atmospheric neutrinos. *Physical Review Letters*, 81(8):1562, 1998.

[15] Q.R. Ahmad et al. Direct evidence for neutrino flavor transformation from neutral-

current interactions in the Sudbury Neutrino Observatory. *Physical Review Letters*, 89(1):011301, 2002.

[16] S. Fukuda et al. Solar ^{8}B and hep Neutrino Measurements from 1258 Days of Super-Kamiokande Data. *Physical Review Letters*, 86(25):5651, 2001.

[17] L. Pasquali and M.H. Reno. Tau neutrino fluxes from atmospheric charm. *Physical Review D*, 59(9):093003, 1999.

[18] H. Athar et al. Effects of neutrino mixing on high-energy cosmic neutrino flux. *Physical Review D*, 62(10):103007, 2000.

[19] E. Waxman, J., and Bahcall. High energy neutrinos from astrophysical sources: An upper bound. *Physical Review D*, 59(2):023002, 1998.

[20] M. Kowalski. Status of high-energy neutrino astronomy. *Journal of Physics: Conference Series*, 632(1):012039, 2015.

[21] T. Gaisser. Spectrum of cosmic-ray nucleons, kaon production, and the atmospheric muon charge ratio. *Astroparticle Physics*, 35(12):801–806, 2012. `https://doi.org/10.1016/j.astropartphys.2012.02.010`.

[22] Wikipedia, Active Galactic nucleus. `https://en.wikipedia.org/wiki/Active_galactic_nucleus`. Accessed: 09-04-2024.

[23] E. Massaro et al. The 5th edition of the Roma-BZCAT. A short presentation. *Astrophysics and Space Science*, 357:1–4, 2015.

[24] M.G. Aartsen et al. (The IceCube Collaboration). The contribution of FERMI-2LAC blazars to diffuse TeV–PeV neutrino flux. *The Astrophysical Journal*, 835(1):45, 2017. `http://dx.doi.org/10.3847/1538-4357/835/1/45`.

[25] F.W. Stecker and M.H. Salamon. High energy neutrinos from quasars. *Space Science Reviews*, 75(1):341–355, 1996.

[26] K.S. Hirata al al. Observation in the Kamiokande-II detector of the neutrino burst from supernova SN1987A. *Physical Review D*, 38(2):448, 1988.

[27] R.M. Bionta et al. Observation of a neutrino burst in coincidence with supernova 1987A in the Large Magellanic Cloud. *Physical Review Letters*, 58(14):1494, 1987.

[28] E.N. Alexeyev et al. Detection of the neutrino signal from SN1987a using the INR Baksan underground scintillation telescope. In *Neutrino Physics: Proceedings of an International Workshop Held in Heidelberg, October 20–22, 1987*, pages 288–298. Springer, 1988.

[29] M. Aglietta et al. On the event observed in the Mont Blanc Underground Neutrino observatory during the occurrence of Supernova 1987a. *Europhysics Letters*, 3(12):1315, 1987.

[30] N. Valtonen-Mattila and E. O'Sullivan. Prospects for extending the core-collapse supernova detection horizon using high-energy neutrinos. *The Astrophysical Journal*, 945(2):98, 2023.

[31] A. Kheirandish and K. Murase. Detecting high-energy neutrino minibursts from

local supernovae with multiple neutrino observatories. *The Astrophysical Journal Letters*, 956(1):L8, 2023.

[32] K. Murase. New prospects for detecting high-energy neutrinos from nearby supernovae. *Physical Review D*, 97(8):081301, 2018.

[33] R.W. Klebesadel et al. Observations of gamma-ray bursts of cosmic origin. *Astrophysical Journal, vol. 182, p. L85*, 182:L85, 1973.

[34] E. Waxman and J. Bahcall. High energy neutrinos from cosmological gamma-ray burst fireballs. *Physical Review Letters*, 78(12):2292, 1997.

[35] C. Evoli et al. Diffuse Neutrino and Gamma-ray Emissions of the Galaxy above the TeV. *Journal of Cosmology and Astroparticle Physics*, 2007(06):003, 2007.

[36] R. Wendell and K. Okumura. Recent progress and future prospects with atmospheric neutrinos. *New Journal of Physics*, 17(2):025006, 2015.

[37] R. Enberg et al. Prompt neutrino fluxes from atmospheric charm. *Physical Review D*, 78(4):043005, 2008. https://doi.org/10.1103/PhysRevD.78.043005.

[38] M.G. Aartsen et al. (The IceCube Collaboration). The IceCube Neutrino Observatory: instrumentation and online systems. *Journal of Instrumentation*, 12(03):P03012, 2017.

[39] M. Ageron et al. (The ANTARES Collaboration). ANTARES: the first undersea neutrino telescope. *Nuclear Instruments and Methods in Physics Research Section A: Accelerators, Spectrometers, Detectors and Associated Equipment*, 656(1):11–38, 2011.

[40] M.G. Aartsen et al. (The IceCube Collaboration). Evidence for high-energy extraterrestrial neutrinos at the IceCube detector. *Science*, 342(6161):1242856, 2013. https://doi.org/10.1126/science.1242856.

[41] R. Abbasi et al. Characterization of the Astrophysical Diffuse Neutrino Flux using Starting Track Events in IceCube. *arXiv preprint arXiv:2402.18026*, 2024.

[42] M.G. Aartsen et al. (The IceCube Collaboration). Improved characterization of the astrophysical muon-neutrino flux with 9.5 years of IceCube data. *The Astrophysical Journal*, 928(1):50, 2022. https://doi.org/10.3847/1538-4357/ac4d29.

[43] M.G. Aartsen et al. (The IceCube Collaboration). Characteristics of the diffuse astrophysical electron and tau neutrino flux with six years of IceCube high energy cascade data. *Physical Review Letters*, 125(12):121104, 2020.

[44] M.G. Aartsen et al. (The IceCube Collaboration). Observation of high-energy neutrinos from the Galactic plane. *Science*, 380(6652):1338–1343, 2023. https://doi.org/10.1126/science.adc9818.

[45] The IceCube, MAGIC and other Collaborations. Multimessenger observations of a flaring blazar coincident with high-energy neutrino IceCube-170922A. *Science*, 361(6398):eaat1378, 2018.

[46] M.G. Aartsen et al. (The IceCube Collaboration). Neutrino emission from the direction of the blazar TXS 0506+056 prior to the IceCube-170922A alert. *Science*, 361(6398):147–151, 2018. https://doi.org/10.1126/science.aat2890.

[47] Y.T. Tanaka, S. Buson, and D. Kocevsk. Fermi-LAT detection of increased gamma-ray activity of TXS 0506+056, located inside the IceCube-170922A error region. *The Astronomer's Telegram*, 10791:1, 2017.

[48] C. Baixeras et al. (The MAGIC Collaboration). The MAGIC telescope. *Nuclear Physics B-Proceedings Supplements*, 114:247–252, 2003.

[49] D. Dornic and A. Coleiro. Search for counterpart to IceCube-170922A with ANTARES. *The Astronomer's Telegram*, 10773:1, 2017.

[50] M.G. Aartsen et al. (The IceCube Collaboration). Evidence for neutrino emission from the nearby active galaxy NGC 1068. *Science*, 378(6619):538–543, 2022. `https://doi.org/10.1126/science.abg3395`.

[51] R. Abbasi et al. (The IceCube Collaboration). Detection of astrophysical tau neutrino candidates in IceCube. 82(11):1031, 2022.

[52] R. Abbasi et al. (The IceCube Collaboration). Observation of Seven Astrophysical Tau Neutrino Candidates with IceCube. 132(15):151001, 2024.

[53] S. Wilks. The large-sample distribution of the likelihood ratio for testing composite hypotheses. *The annals of mathematical statistics*, 9(1):60–62, 1938.

[54] M.Y. Wing et al. (The IceCube Collaboration). Physics Potential of the IceCube Upgrade. In *Journal of Physics: Conference Series*, volume 1468, page 012169. IOP Publishing, 2020.

[55] A. Avrorin et al. (The Baikal-GVD Collaboration). The Baikal neutrino experiment. *Nuclear Instruments and Methods in Physics Research Section A: Accelerators, Spectrometers, Detectors and Associated Equipment*, 626:S13–S18, 2011.

[56] V.M. Aynutdinov et al. (The Baikal-GVD Collaboration). Large neutrino telescope Baikal-GVD: recent status. *arXiv:2309.16310*, 2023.

[57] J.P. Twagirayezu et al. Performance of the Pacific Ocean Neutrino Experiment. 38th ICRC, July 2023, Nagoya, Japan. PoS(ICRC2023)1175, `https://pos.sissa.it/444/1175/pdf`.

[58] Q. Chang et al. Optimizing the optical array geometry for TRIDENT. 38th ICRC, July 2023, Nagoya, Japan. PoS(ICRC2023)1203, `https://pos.sissa.it/444/1203/pdf`.

[59] T. Huang et al. Proposal for the High Energy Neutrino Telescope. 38th ICRC, July 2023, Nagoya, Japan. PoS(ICRC2023)1080, `https://pos.sissa.it/444/1080/pdf`.

[60] A. Candido et al. Neutrino structure functions from GeV to EeV energies. *Journal of High Energy Physics*, 2023(5):1–78, 2023.

[61] S.L. Glashow. Resonant scattering of antineutrinos. *Physical Review*, 118(1):316, 1960. `https://doi.org/10.1103/PhysRev.118.316`.

[62] I. Frank and I. Tamm. Coherent visible radiation of fast electrons passing through matter. In *Selected Papers*, pages 29–35. Springer, 1991.

[63] M. Gupta. Calculation of radiation length in materials. 2010. https://cds.cern.ch/record/1279627.

[64] R. Mirani. Parametrisation of EM-showers in the ANTARES detector-volume. 2002. Master's thesis, University of Amsterdam.

[65] C. Kopper at al. (The KM3NeT Collaboration). Performance studies for the KM3NeT neutrino telescope. *Nuclear Instruments and Methods in Physics Research Section A: Accelerators, Spectrometers, Detectors and Associated Equipment*, 692:188–191, 2012.

[66] S.I. Klimushin et al. Precise parametrizations of muon energy losses in water. 27th ICRC, August 2001, Hamburg, Germany. https://arxiv.org/pdf/hep-ph/0106010.pdf.

[67] M. Tanabashi et al. Particle data group. *Phys. Rev. D*, 98(3):030001, 2018.

[68] R. Muller. Getting to the point: First cosmic neutrino source search with the KM3NeT/ARCA detector. 2023. PhD thesis, University of Amsterdam, https://pure.uva.nl/ws/files/129586496/Thesis.pdf.

[69] S. Adrián-Martínez et al. (The KM3NeT Collaboration). Letter of intent for KM3NeT 2.0. *Journal of Physics G: Nuclear and Particle Physics*, 43(8):084001, 2016. https://doi.org/10.1088/0954-3899/43/8/084001.

[70] R. Muller and T.J. van Eeden (The KM3NeT Collaboration). Search for cosmic neutrino point sources and extended sources with 6-21 lines of KM3NeT/ARCA. 38th ICRC, July 2023, Nagoya, Japan. PoS(ICRC2023)1018, https://doi.org/10.22323/1.444.1018.

[71] V. Tsourapis et al. (The KM3NeT Collaboration). Search for a diffuse astrophysical neutrino flux with KM3NeT/ARCA using data of 2021-2022. 38th ICRC, July 2023, Nagoya, Japan. PoS(ICRC2023)1195, https://doi.org/10.22323/1.444.1195.

[72] F. Fillipini et al. (The KM3NeT Collaboration). Search for a diffuse astrophysical neutrino flux from the Galactic Ridge using KM3NeT/ARCA data. 38th ICRC, July 2023, Nagoya, Japan. PoS(ICRC2023)1190, https://doi.org/10.22323/1.444.1190.

[73] S. Aiello et al. (The KM3NeT Collaboration). The KM3NeT multi-PMT optical module. *Journal of Instrumentation*, 17(07):P07038, 2022. https://doi.org/10.1088/1748-0221/17/07/P07038.

[74] S. O. Flyckt. *Photomultiplier tubes: principles and applications*. Photonis, 2002.

[75] Hamamatsu Photonics. Photomultiplier tubes: Basics and applications. *Edition 3a*, 310, 2007.

[76] S. Aiello et al. (The KM3NeT Collaboration). Characterisation of the Hamamatsu photomultipliers for the KM3NeT Neutrino Telescope. *Journal of Instrumentation*, 13(05):P05035, 2018.

[77] J. Serrano et al. The white rabbit project. 2013. https://cds.cern.ch/record/1743073.

[78] R. Bruijn et al. (The KM3NeT Collaboration). The KM3NeT Digital Optical Module and Detection Unit, 2019.

[79] M. Ageron et al. (The KM3NeT Collaboration). Dependence of atmospheric muon flux on seawater depth measured with the first KM3NeT detection units. *The European Physical Journal C*, 80(2):1–11, 2020. https://doi.org/10.1140/epjc/s10052-020-7629-z.

[80] B. Ó Fearraigh. Following the light. Novel event reconstruction techniques for neutrino oscillation analyses in KM3NeT/ORCA. 2024. PhD thesis, University of Amsterdam, https://pure.uva.nl/ws/files/155195983/Thesis.pdf.

[81] K. Melis et al. (The KM3NeT Collaboration). In-situ calibration of KM3NeT. 35th ICRC, July 2017, Busan, Korea. PoS(ICRC2017)1059, https://doi.org/10.22323/1.301.1059.

[82] S. Aiello et al. (The KM3NeT Collaboration). Nanobeacon: A time calibration device for the KM3NeT neutrino telescope. *Nuclear Instruments and Methods in Physics Research Section A: Accelerators, Spectrometers, Detectors and Associated Equipment*, 1040:167132, 2022.

[83] L. Bailly-Salins et al. (The KM3NeT Collaboration). Time, position and orientation calibration using atmospheric muons in KM3NeT. 38th ICRC, July 2023, Nagoya, Japan. PoS(ICRC2023)218, https://doi.org/10.22323/1.444.0218.

[84] A. S. Sánchez Losa et al. (The KM3NeT Collaboration). KM3NeT Time calibration with Nanobeacons. 38th ICRC, July 2023, Nagoya, Japan. PoS(ICRC2023)1062, https://doi.org/10.22323/1.444.1062.

[85] C. Gatius Oliver et al. (The KM3NeT Collaboration). Dynamical position and orientation calibration of the KM3NeT telescope. 38th ICRC, July 2023, Nagoya, Japan. PoS(ICRC2023)1033, https://doi.org/10.22323/1.444.1033.

[86] S. Aiello et al. (The KM3NeT Collaboration). First observation of the cosmic ray shadow of the Moon and the Sun with KM3NeT/ORCA. *The European Physical Journal C*, 83(4):344, 2023. https://doi.org/10.1140/epjc/s10052-023-11401-5.

[87] S. Aiello et al. (The KM3NeT Collaboration). gSeaGen: the KM3NeT GENIE-based code for neutrino telescopes. *Computer Physics Communications*, 256:107477, 2020. https://doi.org/10.1016/j.cpc.2020.107477.

[88] A. Garcia Soto and C. Distefano. Upgrading gSeaGen: from MeV to PeV neutrinos. *Journal of Instrumentation*, 16(09):C09008, 2021.

[89] A.M. Dziewonski and D.L. Anderson. Preliminary reference Earth model. *Physics of the earth and planetary interiors*, 25(4):297–356, 1981.

[90] M. Honda et al. Calculation of atmospheric neutrino flux using the interaction model calibrated with atmospheric muon data. *Physical Review D*, 75(4):043006, 2007. https://doi.org/10.1103/PhysRevD.75.043006.

[91] G. Carminati et al. Atmospheric MUons from PArametric formulas: a fast GEnerator for neutrino telescopes (MUPAGE). *Computer Physics Communications*, 179(12):915–923, 2008. https://doi.org/10.1016/j.cpc.2008.07.014.

[92] M. de Jong and E. van Campenhout. The probability density function of the arrival time Cherenkov light. *arXiv*, 2023. https://doi.org/10.48550/arXiv.2305.19626.

[93] K. Melis et al. (The KM3NeT Collaboration). KM3NeT/ARCA event reconstruction algorithms. 35th ICRC, July 2017, Busan, Korea. PoS(ICRC2017)950, https://doi.org/10.22323/1.301.0950.

[94] T.J. van Eeden and J. Seneca (The KM3NeT Collaboration). High-energy reconstruction for single and double cascades using the KM3NeT detector. 37th ICRC, July 2021, Berlin, Germany. PoS(ICRC2021)1089, https://doi.org/10.22323/1.395.1089.

[95] S. Aiello et al. (The KM3NeT Collaboration). Astronomy potential of KM3NeT/ARCA. *The European Physical Journal C*, 84(9):885, 2024. https://doi.org/10.1140/epjc/s10052-024-13137-2.

[96] H. Voss et al. TMVA, the toolkit for multivariate data analysis with ROOT. XI ACAT, April 2007, Amsterdam, Netherlands. PoS(ACAT)040, https://doi.org/10.22323/1.050.0040.

[97] S. Alves et al. (The ANTARES Collaboration). Searches for point-like sources of cosmic neutrinos with 15 years of ANTARES data. 38th ICRC, July 2023, Nagoya, Japan. PoS(ICRC2023)1128, https://doi.org/10.22323/1.444.1128.

[98] M.G. Aartsen et al. (The IceCube Collaboration). All-sky search for time-integrated neutrino emission from astrophysical sources with 7 yr of IceCube data. *The Astrophysical Journal*, 835(2):151, 2017. https://doi.org/10.3847/1538-4357/835/2/151.

[99] M.G. Aartsen et al. (The IceCube Collaboration). Time-integrated neutrino source searches with 10 years of IceCube data. *Physical Review Letters*, 124(5):051103, 2020. https://doi.org/10.1103/PhysRevLett.124.051103.

[100] G. Riccobene et al. (The KM3NeT Collaboration). Deep seawater inherent optical properties in the Southern Ionian Sea. *Astroparticle Physics*, 27(1):1–9, 2007. https://doi.org/10.1016/j.astropartphys.2006.08.006.

[101] C. M. Hugon. GEANT4 simulation of optical modules in neutrino telescopes. 34th ICRC, July 2015, The Hague, Netherlands. PoS(ICRC2015)1106, https://doi.org/10.22323/1.236.1106.

[102] S. Adrián-Martínez et al. (The KM3NeT Collaboration). The prototype detection unit of the KM3NeT detector: KM3NeT Collaboration. *The European Physical Journal C*, 76:1–12, 2016.

[103] G. Illuminati et al. (The ANTARES Collaboration). Searches for point-like sources of cosmic neutrinos with 13 years of ANTARES data. 37th ICRC, July 2021, Berlin, Germany. PoS(ICRC2021)1161, https://doi.org/10.22323/1.395.1161.

[104] A. Albert et al. (The ANTARES and IceCube Collaborations). ANTARES and IceCube combined search for neutrino point-like and extended sources in the southern sky. *The Astrophysical Journal*, 892(2):92, 2020.

[105] S. Abdollahi et al. Incremental Fermi Large Area Telescope Fourth Source Catalog. *The Astrophysical Journal Supplement Series*, 260(2):53, 2022.

[106] Z. Cao et al. Ultrahigh-energy photons up to 1.4 petaelectronvolts from 12 γ-ray Galactic sources. *Nature*, 594(7861):33–36, 2021.

[107] S.P. Wakely and D. Horan. TeVCat: an online catalog for Very High Energy Gamma-ray Astronomy. In *International Cosmic Ray Conference*, volume 3, pages 1341–1344, 2008.

[108] M. Boettcher et al. Multiwavelength and Multimessenger Observations of Blazars and Theoretical Modeling: Blazars as Astrophysical Neutrino Sources. *arXiv preprint arXiv:2204.12242*, 2022.

[109] A. Plavin. Growing evidence for high-energy neutrinos originating in radio blazars. *Monthly Notices of the Royal Astronomical Society*, 523(2):1799–1808, 2023.

[110] L. Petrov et al. Radio Fundamental Catalogue. `http://astrogeo.org/rfc/`. Accessed: March 2023.

[111] T.J. van Eeden et al. (The KM3NeT Collaboration). Event reconstruction and neutrino selection with KM3NeT/ARCA230. 38th ICRC, July 2023, Nagoya, Japan. PoS(ICRC2023)1074, `https://doi.org/10.22323/1.444.1074`.

[112] K. Gorski et al. HEALPix: A framework for high-resolution discretization and fast analysis of data distributed on the sphere. *The Astrophysical Journal*, 622(2):759, 2005.

[113] F. Aharonian et al. Observations of Mkn 421 in 2004 with HESS at large zenith angles. *Astronomy & Astrophysics*, 437(1):95–99, 2005.

[114] R. Bormuth. Chasing cosmic tau neutrinos in the abyss. 2017. PhD thesis, University of Leiden, `https://scholarlypublications.universiteitleiden.nl/access/item%3A2949392/download`.

English summary

Looking at the stars

Throughout history, humanity has looked to the stars. Our journey through the cosmos has been a tale of constant discovery. Early societies used the naked eye to track celestial patterns and navigate the world. This knowledge eventually led to the creation of the first observatories, where humans studied the skies to mark the changing seasons and guide agricultural cycles. Our understanding of the universe has been shaken multiple times. Moving the center of the universe from the Earth, to the Sun, to having no center at all. Embracing this new knowledge wasn't easy, but the development of the telescope helped to make it undeniable. Since then, we have expanded our view of the universe by taking advantage of the entire electromagnetic spectrum. Increasingly advanced telescopes revealed the vastness and complexity of the cosmos using electromagnetic waves ranging from radio to high-energy gamma-rays. This is illustrated in Figure E.1, which presents a cluster of stars captured in visible light and infrared. Is this where the story ends? Or are there more ways to explore and understand the universe?

Figure E.1: The Pillars of Creation in the Eagle Nebula: the left image was captured in visible light, while the right was taken in infrared. Image credit: NASA, ESA/Hubble.

Cosmic rays

The rest of this story moves beyond photons as the messengers from our universe. The Earth is bombarded with energetic particles coming from outer space. These particles are charged and they are called cosmic rays. They can reach energies up to a million times more than produced in Earth's most powerful particle accelerator: the Large Hadron Collider at CERN in Geneva. The astonishing energies drive scientists worldwide to uncover the origin of cosmic rays and unravel the mechanisms behind them.

The origin of these energetic particles has remained elusive, even after a century of research. Their paths through the universe are curved due to deflections by magnetic fields, which makes pinpointing their sources challenging. The production of cosmic rays could be accompanied by gamma-rays, but the detection of these photons is challenging due to their inability to traverse dense regions of space due to absorption. Scientists have no intention of giving up. Finding the origin of cosmic rays is an important step in understanding the acceleration mechanisms and the environments that produce them.

Is there a way to peer into the densest and most violent regions of our universe? Enter the most elusive particle known to humanity: the neutrino. They traverse our universe in straight lines and rarely interact with matter, making them perfect messengers from distant mysterious objects.

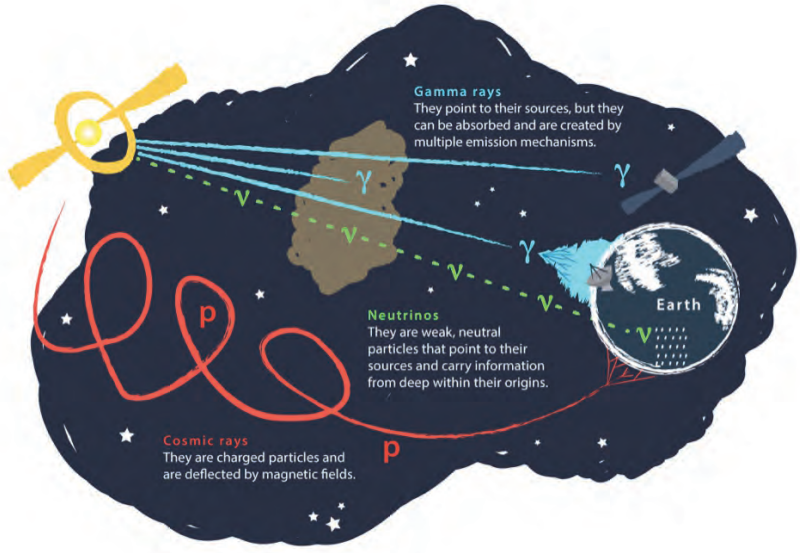

Figure E.2: Cosmic messengers that travel through the universe. Image credit: IceCube.

Neutrinos

Neutrinos are elementary particles that are described by the Standard Model. The Standard Model is a theory in physics that explains the basic building blocks of the universe and how they interact. It describes all known particles and the forces that act on them, as shown in the overview in Figure E.3.

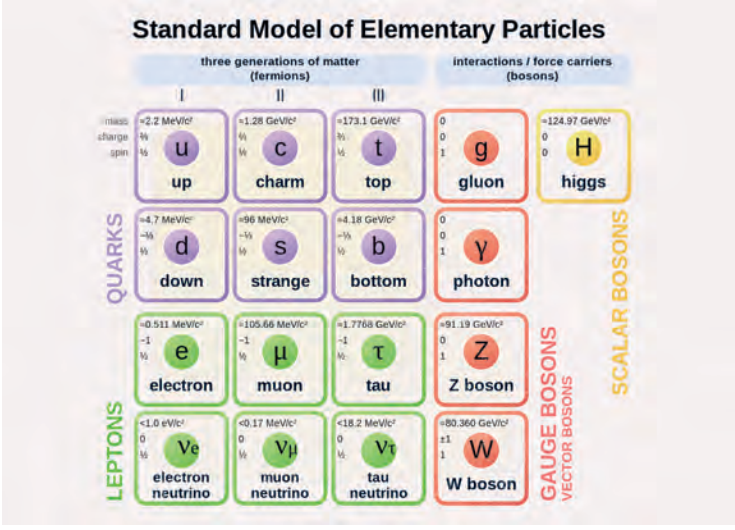

Figure E.3: The Standard Model of elementary particles. Image credit: Wikipedia.

The matter around us is composed of protons, neutrons, and electrons. Electrons are elementary particles, meaning they cannot be broken down into smaller components. Protons and neutrons, however, are made up of up and down quarks, completing the first generation of matter, or fermions, which also includes the electron and the electron neutrino. In addition to fermions, there are bosons, which act as the force carriers controlling the fundamental forces of nature that dictate how fermions interact. There are three known generations of fermions, each associated with a different type of neutrino, or 'flavour': electron, muon, and tau. The flavour of a neutrino determines which elementary particle it can produce when it interacts.

These interactions are rare, and neutrinos are the only fermions without electric charge. They are the second most abundant particle in the universe, just after photons. The mass of a neutrino is incredibly tiny — so tiny that it was thought to be zero. They are produced in a variety of processes, including nuclear reactions in stars and radioactive decays. The Sun showers the Earth with billions of neutrinos, but the vast majority passes straight through the planet without interacting at all. These characteristics have earned neutrinos the nickname 'ghost particles'. They are present, but we can't see them.

Neutrinos are not only produced inside our Solar System, but throughout the entire universe. Astroparticle physics theory predicts that cosmic rays and gamma-rays are accompanied by energetic neutrinos that point straight back to their source. These particles carry insights on regions hidden from view when detecting light. But how are these messengers understood when they are infamous for their elusiveness?

The KM3NeT detector

Figure E.4: The KM3NeT optical module containing sensitive light detectors.

To overcome the rarity of neutrino interactions, a massive telescope is being constructed in order to catch as many neutrinos as possible. This challenge is taken on by KM3NeT, which stands for the Cubic Kilometre Neutrino Telescope. The KM3NeT telescope is not situated at the surface of the Earth or in space, but at the bottom of the Mediterranean Sea. When neutrinos interact with seawater, they create charged particles that generate light. This faint light is captured by sensitive detectors housed in glass spheres, which shield them from salt water and high pressure. These assemblies are called optical modules and an example is shown in Figure E.4.

The KM3NeT detector will comprise of thousands of optical modules, placed along vertical strings that are mounted to the seabed. An illuminated representation is shown in Figure E.5, as the actual surroundings are pitch dark several kilometers below the surface. The detector is divided into two sections: the ORCA detector focuses on low-energy neutrinos to study their properties, while the ARCA detector targets high-energy neutrinos for doing neutrino astronomy. The analyses in this thesis focus on the ARCA detector.

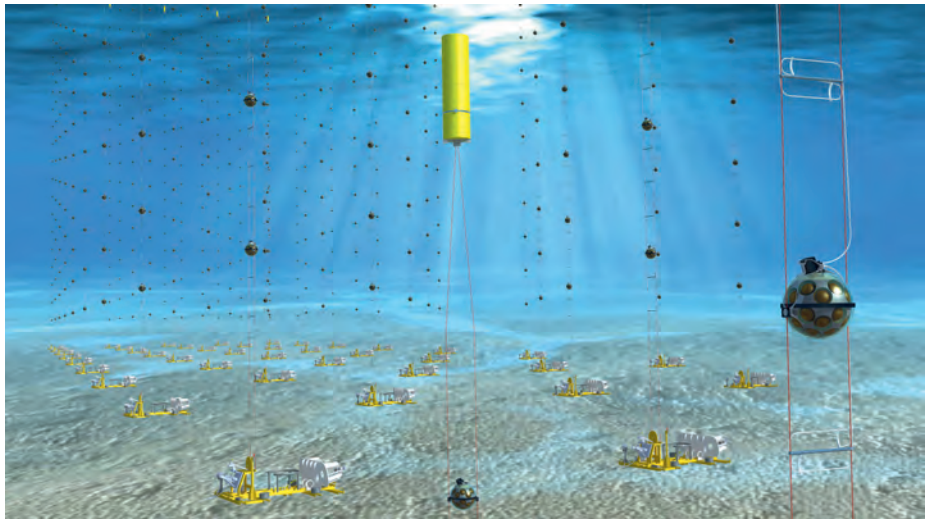

Figure E.5: The KM3NeT detector at the bottom of the Mediterranean Sea.

The light patterns generated by neutrino interactions are used to determine their energy, flavour and direction, which reveal their origin. Welcome to the emerging field of neutrino astronomy.

Translating the light patterns

Key challenges of this experiment are distinguishing neutrinos from background signals and the translation of light patterns to the properties of the neutrinos. This thesis introduces a new method focused on a promising light pattern produced by one type of neutrino: the tau neutrino.

The interaction of a tau neutrino with water produces a cascade of secondary particles and radiation as shown in Figure E.6. Alongside this cascade, a tau particle is created, which quickly decays into a subsequent cascade. This light pattern is known as a 'double cascade' and it offers a significant advantage in identifying neutrino sources due to its absence of background noise. The primary background source in neutrino astronomy originates from the interaction of cosmic rays with our atmosphere. This process also generates neutrinos, but the expected number of tau neutrinos is virtually zero.

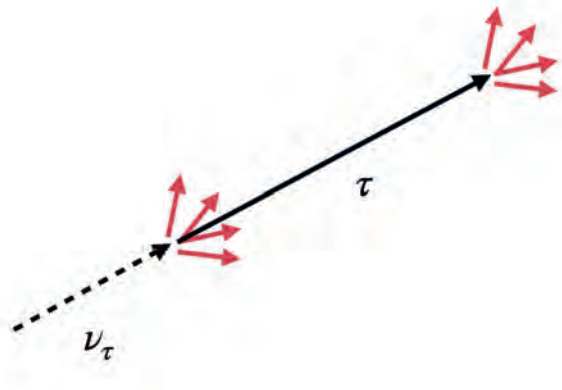

Figure E.6: The double cascade pattern produced by a tau neutrino.

The method described in this work was developed using simulations of tau neutrino interactions. It identifies the neutrino properties that most closely match the observed light pattern. The result is an estimate of the energy and the direction of the neutrino that can be compared to the simulated properties. This work led to a significant improvement in the direction estimation, achieving even greater accuracy for larger distances between the two cascades as shown in Figure E.7. The results show great promise for transitioning from simulations to applying this procedure to actual data from the sea in the near future.

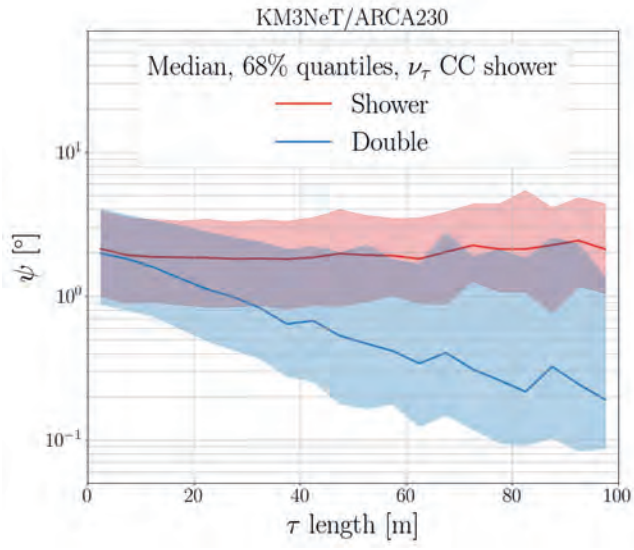

Figure E.7: Angle between the estimated and true direction of the neutrino (ψ) as a function of the distance between the particle cascades (τ length). The new method (blue) is compared to the standard procedure (red).

The search for neutrino sources

One of the primary analyses in this thesis involves searching for neutrino sources in the latest data collected by the ARCA detector. The detector is still under construction, but neutrinos are already detected. Over a year of data using various detector configurations was filtered in order to increase the ratio of neutrino detections to background events. This dataset was used to investigate whether a set of astrophysical objects emits neutrinos. The astrophysical objects were chosen for their likelihood of generating high-energy neutrinos.

Cosmic neutrinos are pointing to the vicinity of their origin and they are typically detected with higher energies compared to background events. This information is used to calculate the likelihood that a detection was caused by a neutrino from a candidate source. For all candidate sources, the data are compatible with background, meaning no new neutrino sources were discovered.

The analysis places upper limits on the flux of neutrinos from each source, which are significantly lower than the previous analyses as shown in Figure E.8. A dot indicates the maximum possible neutrino flux from a candidate source; if the flux had been higher, we would have detected it. The lowering of the limits represents our enhanced ability to detect lower neutrino fluxes. This is due to the increasing size of the dataset and the detector, alongside improved neutrino selection procedures and reconstruction performances. The initial analysis used 92 days of data taken with 6 detection strings (ARCA6), whereas this work incorporates 421 days of data taken with up to 21 strings (ARCA6-21).

The sensitivity ARCA is nearing that of ANTARES, KM3NeT's predecessor, which required 15 years of data to achieve its results. Future versions of this analysis are particularly promising in the Southern Sky ($\sin(\delta) < 0$), where the leading neutrino astronomy experiment called IceCube is less sensitive.

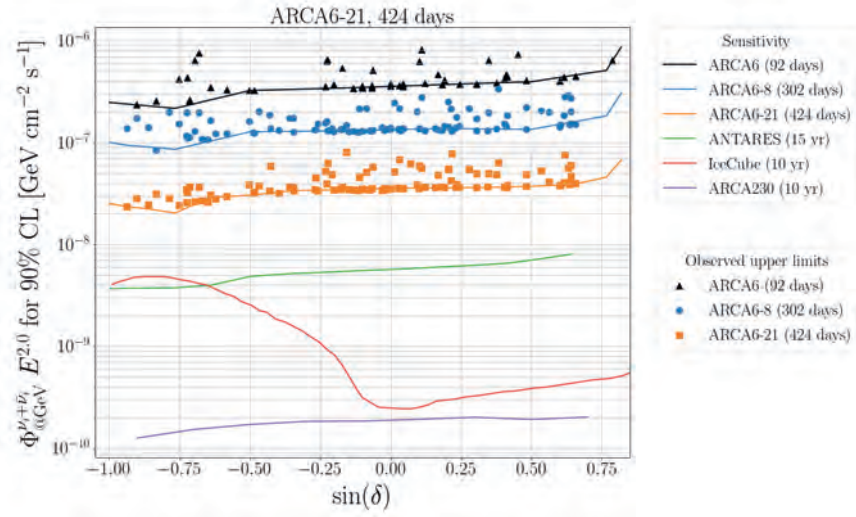

Figure E.8: Comparison of the observed limits (dots) and sensitivity (lines) of the neutrino flux Φ as a function of the declination δ. The results are compared with earlier presented results of the full ANTARES dataset, 10 years of IceCube data and after 10 years using the complete ARCA detector.

The potential of the complete detector

The study of the current data of the ARCA detector is accompanied by predictions for the full detector performance. The completion of the construction of the ARCA detector is foreseen in the upcoming years, and this thesis provides the updated sensitivity. The sensitivity to neutrino point sources using 10 years of data is shown in Figure E.8. Once completed, the detector will be capable of detecting neutrino fluxes that are beyond the reach of current neutrino observatories over the full sky.

Another benchmark for assessing the potential of ARCA is the re-discovery of the diffuse neutrino flux. This isotropic neutrino flux was the definitive evidence of cosmic neutrinos, discovered by the IceCube Collaboration in 2013. The ARCA detector can re-discover this neutrino flux within half a year of operation as shown in Figure E.9. By taking advantage of data from the current growing detector, such re-discovery can happen earlier.

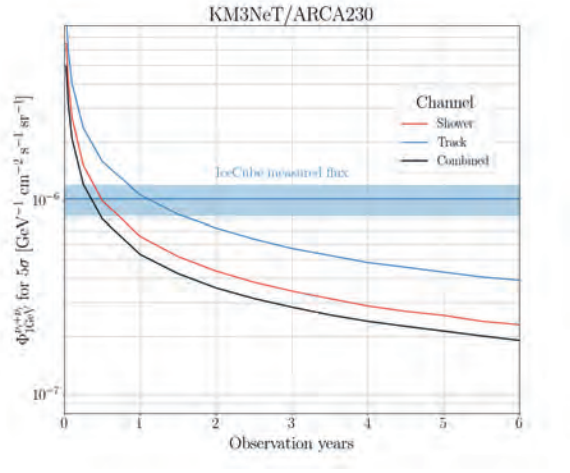

Figure E.9: The neutrino flux Φ that produces a discovery as a function of increasing years of observation. The blue lines represent the estimated flux normalisation obtained from IceCube including their uncertainties. The intersection indicates an estimation of the amount of time needed to re-discover the neutrino flux from IceCube.

A wealth of information about the environment around a neutrino source is contained in the flavour of the neutrinos. The relative contribution of each flavour to the total flux indicates different scenarios for cosmic ray acceleration according to theory. This work studied the capability of ARCA to measure the flavour ratio of neutrinos for different years of observation time, as shown in Figure E.10. The detector performance offers promising potential in distinguishing between the three neutrino flavours. The study of the flavour ratio of neutrinos will be continued with the current ARCA detector and data.

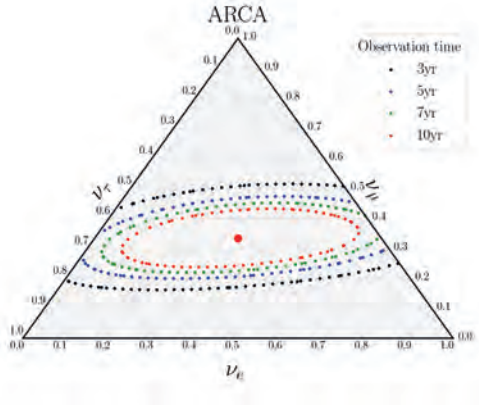

Figure E.10: Ternary graph with the relative contribution of electron, muon and tau neutrinos on each axis. The total sum always adds up to 1. The lines represent the capability of ARCA to measure the flavour ratio when the true ratio is 1/3:1/3:1/3 (red dot) using 3,5,7 and 10 years of ARCA data. The decreasing size of the contours represent a better measurement of the neutrino flavour ratio.

Nederlandse samenvatting

Kijken naar de sterren

Sterrenkunde is zo oud als de mensheid zelf. Onze verkenning van het heelal is een verhaal van voortdurende ontdekkingen. De eerste samenlevingen gebruikten het blote oog om sterrenbeelden te volgen en voor navigatie te gebruiken. Deze kennis leidde uiteindelijk tot de eerste sterrenwachten, waar mensen de hemel bestudeerden om de veranderende seizoenen te markeren, wat cruciaal was voor de landbouw. Ons begrip van het heelal is meerdere keren op de proef gesteld. Het centrum van het universum werd verplaatst van de aarde naar de zon, naar een plek die niet kan worden vastgesteld. Het omarmen van deze nieuwe kennis was niet gemakkelijk, maar de ontwikkeling van de telescoop hielp om dit overduidelijk te maken. Sindsdien hebben we onze kijk op het heelal uitgebreid door gebruik te maken van het hele elektromagnetische spectrum. Steeds geavanceerdere telescopen onthulden de uitgestrektheid en complexiteit van de kosmos door gebruik te maken van elektromagnetische golven die variëren van radio tot gammastraling. Dit is geïllustreerd in Figuur N.1, die een groep van sterren afbeeldt, vastgelegd in zichtbaar licht en infrarood. Is dit waar het verhaal eindigt? Of zijn er meer manieren om het heelal te verkennen en te begrijpen?

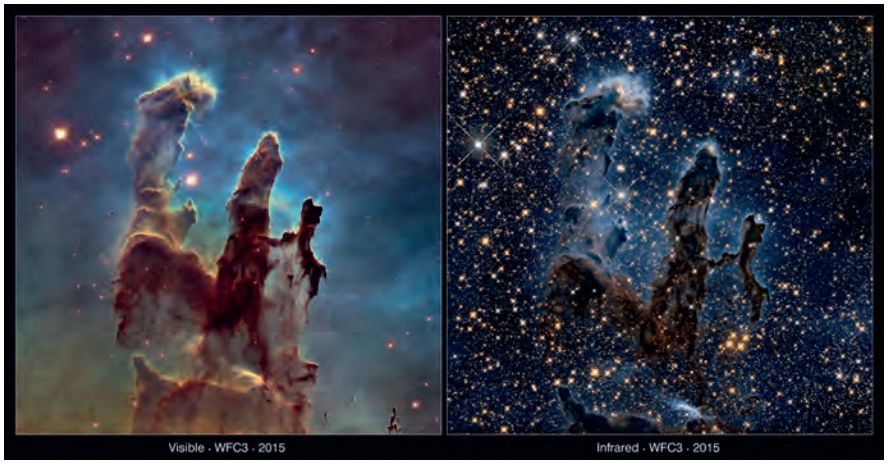

Figure N.1: De Pilaren der Creatie in de Adelaarsnevel: De linker afbeelding is gemaakt in zichtbaar licht, de rechter in infrarood. Afbeelding van: NASA, ESA/Hubble.

Kosmische straling

De rest van dit verhaal beweegt weg van fotonen als de boodschappers van ons universum. De aarde wordt gebombardeerd met energetische deeltjes uit de ruimte. Deze deeltjes zijn geladen en worden kosmische straling genoemd. Ze kunnen energieën bereiken die tot een miljoen keer hoger zijn dan de energie die wordt geproduceerd in de krachtigste deeltjesversneller op aarde: de Large Hadron Collider bij CERN in Genève. De verbazingwekkende energieën drijven wetenschappers van over de hele wereld om de oorsprong van kosmische straling te achterhalen en de mechanismen erachter te ontrafelen.

De oorsprong van deze energetische deeltjes blijft, zelfs na een eeuw onderzoek, onduidelijk. Hun paden door het heelal volgen geen rechte lijn als gevolg van afbuiging door magnetische velden, wat het vinden van de bronnen enorm moeilijk maakt. De productie van kosmische straling kan gepaard gaan met gammastraling, maar de detectie van deze fotonen is een uitdaging omdat ze geabsorbeerd kunnen worden door materie tussen de bron en de aarde. Wetenschappers zijn niet van plan om het op te geven. Het vinden van de oorsprong van kosmische straling is een belangrijke stap in het begrijpen van de versnellingsmechanismen en de omgevingen die deze straling produceren.

Is er een manier om naar de meest gewelddadige delen van ons universum te kijken? Maak kennis met het meest ongrijpbare deeltje dat de mensheid kent: de neutrino. Ze doorkruisen ons universum in een rechte lijn en hebben zelden interacties met materie, waardoor ze perfecte boodschappers zijn van verre mysterieuze objecten.

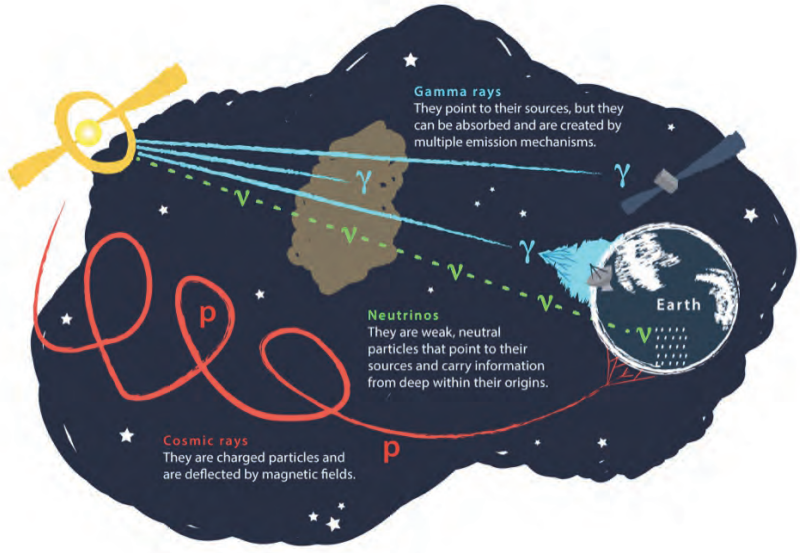

Figure N.2: Kosmische boodschappers die door het heelal reizen. Afbeelding van: IceCube.

Neutrino's

Neutrino's zijn elementaire deeltjes die worden beschreven door het Standaardmodel. Het Standaardmodel is een natuurkundige theorie die de bouwstenen van het universum en hun onderlinge wisselwerking verklaart. Het beschrijft alle bekende deeltjes en de krachten die erop inwerken, zoals te zien is in het overzicht in Figuur N.3.

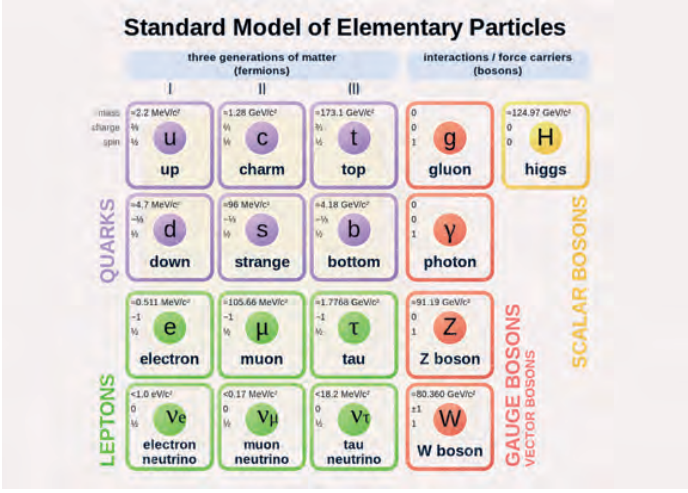

Figure N.3: Het Standaardmodel van elementaire deeltjes. Afbeelding van: Wikipedia.

De materie om ons heen bestaat uit protonen, neutronen en elektronen. Elektronen zijn elementaire deeltjes, wat betekent dat ze niet kunnen worden opgesplitst in kleinere componenten. Protonen en neutronen zijn echter opgebouwd uit up en down quarks, die samen met het elektron en het elektron neutrino de eerste generatie materie (fermionen) compleet maakt. Naast fermionen zijn er bosonen, die fungeren als de krachtdragers die de fundamentele natuurkrachten bepalen tussen fermionen. Er zijn drie generaties fermionen, die elk geassocieerd zijn met een ander type neutrino, of 'smaak': elektron, muon en tau. De smaak van een neutrino bepaalt welk elementair deeltje het kan produceren bij een interactie.

Deze interacties zijn zeldzaam, en neutrino's zijn de enige fermionen zonder elektrische lading. Ze zijn het op één na meest voorkomende deeltje in het heelal, net na fotonen. De massa van een neutrino is ongelooflijk klein - zo klein dat men lang dacht dat hij nul was. Ze worden in verschillende processen geproduceerd, waaronder kernreacties in sterren en radioactief verval. De zon overspoelt de aarde met miljarden neutrino's, maar de overgrote meerderheid gaat dwars door de planeet heen zonder dat we het doorhebben. Deze eigenschappen hebben neutrino's de bijnaam 'spookdeeltjes' opgeleverd. Ze zijn aanwezig, maar we kunnen ze niet zien.

Neutrino's worden niet alleen in ons zonnestelsel geproduceerd, maar in het hele universum. De theorie van de astrodeeltjesfysica voorspelt dat kosmische straling en gammastralen vergezeld gaan met energetische neutrino's die rechtstreeks naar hun bron wijzen. Deze deeltjes dragen inzichten over gebieden die bij het detecteren van licht onzichtbaar zouden zijn. Maar hoe worden deze boodschappers begrepen als ze berucht zijn om hun ongrijpbaarheid?

De KM3NeT detector

Figure N.4: De KM3NeT optische module met gevoelige lichtdetectoren.

Om de zeldzaamheid van neutrino interacties te overwinnen, wordt er een enorme telescoop gebouwd om zoveel mogelijk neutrino's te vangen. Deze uitdaging wordt aangegaan door KM3NeT, wat staat voor Cubic Kilometre Neutrino Telescope. Deze telescoop bevindt zich niet op het aardoppervlak of in de ruimte, maar op de bodem van de Middellandse Zee. Wanneer neutrino's een interactie aangaan in het zeewater, creëren ze geladen deeltjes die licht genereren. Dit zwakke licht wordt opgevangen door gevoelige detectoren in glazen bollen, die ze afschermen van het zoute water en de hoge druk. Deze apparaten worden optische modules genoemd en een voorbeeld is te zien in Figuur N.4.

De KM3NeT detector bestaat uit duizenden optische modules die langs verticale lijnen op de zeebodem worden geplaatst. Een verlichte weergave wordt getoond in Figuur N.5, aangezien de werkelijke omgeving enkele kilometers onder het oppervlak pikdonker is. De detector is verdeeld in twee secties: de ORCA detector richt zich op neutrino's met lage energie om neutrino eigenschappen te bestuderen, terwijl de ARCA detector zich richt op neutrino's met hoge energie voor het doen van neutrino astronomie. Het onderzoek in dit proefschrift richt zich op de ARCA detector.

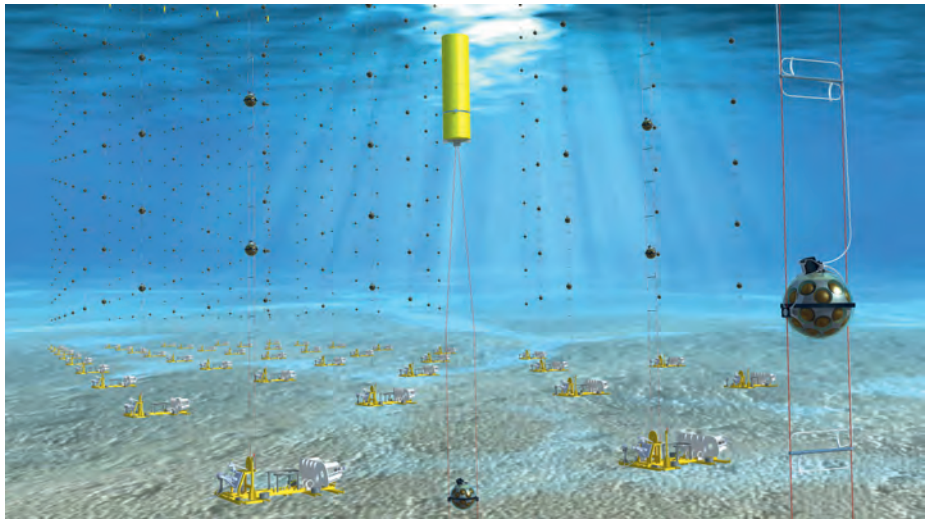

Figure N.5: De KM3NeT detector op de bodem van de Middellandse Zee.

De lichtpatronen die worden geproduceerd door neutrino interacties worden gebruikt om de energie, smaak en richting te bepalen, wat hun oorsprong onthult. Welkom in de opkomende wereld van de neutrino astronomie.

De vertaling van de lichtpatronen

De belangrijkste uitdagingen van dit experiment zijn het onderscheiden van neutrino's van achtergrondsignalen en het vertalen van lichtpatronen naar de eigenschappen van de neutrino's. Dit proefschrift introduceert een nieuwe methode die zich richt op een veelbelovend lichtpatroon dat door één type neutrino wordt geproduceerd: het tau neutrino.

De interactie van een tau neutrino met water produceert een cascade van secundaire deeltjes en straling, zoals te zien is in Figuur E.6. Naast deze cascade wordt een tau deeltje gecreëerd dat snel vervalt in een tweede cascade. Dit lichtpatroon staat bekend als een 'dubbele cascade' en biedt een belangrijk voordeel bij het identificeren van neutrino bronnen door de afwezigheid van achtergrondruis. De primaire achtergrondbron in neutrino astronomie is afkomstig van de interactie van kosmische straling met onze atmosfeer. Dit proces genereert ook neutrino's, maar het verwachte aantal tau neutrino's is vrijwel nul.

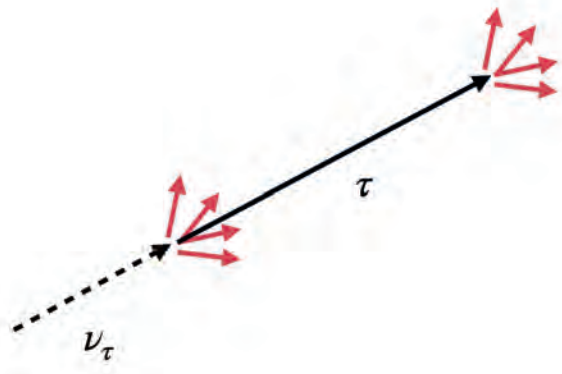

Figure N.6: Het dubbele cascade licht patroon geproduceerd door een tau neutrino.

De methode die in dit werk wordt beschreven, is ontwikkeld met behulp van simulaties van tau neutrino interacties. De methode identificeert de neutrino eigenschappen die het best overeenkomen met het waargenomen lichtpatroon. Het resultaat is een schatting van de energie en de richting van het neutrino die vergeleken kan worden met de gesimuleerde eigenschappen. Dit werk leidde tot een aanzienlijke verbetering in de afschatting van de richting, die nog nauwkeuriger is voor grotere afstanden tussen de twee cascades, zoals getoond in Figuur N.7. De resultaten zijn veelbelovend voor de overgang van simulaties naar toepassing op data uit de zee in de nabije toekomst.

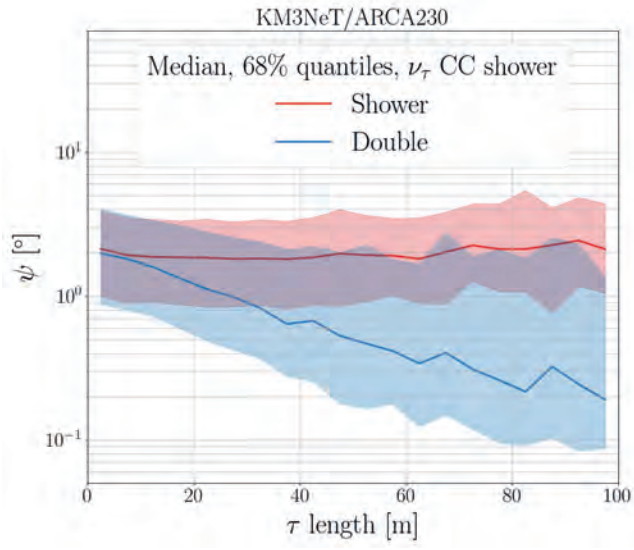

Figure N.7: Hoek tussen de geschatte en de werkelijke richting van de neutrino (ψ) als functie van de afstand tussen de cascades (τ length). De nieuwe methode (blauw) wordt vergeleken met de standaardprocedure (rood).

De zoektocht naar neutrino bronnen

Een van de primaire analyses in dit proefschrift betreft het zoeken naar neutrino bronnen in de nieuwste data die door de ARCA detector zijn verzameld. Ondanks dat de detector nog in aanbouw is, worden er nu al neutrino's gedetecteerd. Meer dan een jaar aan gegevens met verschillende detector configuraties werd gefilterd om de verhouding tussen neutrino detecties en achtergrondsignalen te vergroten. Deze dataset werd gebruikt om te onderzoeken of een set van astrofysische objecten neutrino's uitzendt. De set van astrofysische objecten werd gekozen vanwege hun waarschijnlijkheid om energetische neutrino's te genereren.

Kosmische neutrino's wijzen naar de omgeving van hun bron en ze worden meestal gedetecteerd met hogere energieën in vergelijking met achtergrondsignalen. Deze informatie wordt gebruikt om de waarschijnlijkheid te berekenen dat een waarneming werd veroorzaakt door een neutrino van een astrofysische bron. Voor alle onderzochte bronnen zijn de verzamelde gegevens compatibel met de achtergrond, wat betekent dat er geen nieuwe neutrino bronnen zijn ontdekt.

De analyse stelt bovengrenzen aan de stroom van neutrino's van elke bron, die aanzienlijk lager zijn dan de vorige analyses, zoals te zien is in Figuur N.8. Een punt geeft de maximaal mogelijke neutrino stroom van een mogelijke bron aan; als de neutrino stroom hoger was geweest, dan hadden we hem gedetecteerd. De lagere lijnen en punten geven aan dat we beter in staat zijn om lagere neutrino stromen te meten. Dit komt door de toenemende omvang van de dataset en de detector, naast verbeterde neutrino selectieprocedures en prestaties van de vertaling van de lichtpatronen. De eerste analyse gebruikte 92 dagen aan gegevens die waren gemeten met 6 detectie lijnen (ARCA6), terwijl dit werk 421 dagen aan gegevens gebruikt die zijn opgenomen die met maximaal 21 lijnen (ARCA6-21).

De gevoeligheid van het experiment komt steeds dichterbij die van ANTARES, de voorganger van KM3NeT, die 15 jaar aan gegevens heeft gebruikt om zijn resultaten te bereiken. Toekomstige versies van deze analyse zijn vooral veelbelovend aan de zuidelijke hemel ($\sin(\delta) < 0$), waar het toonaangevende neutrino astronomie experiment IceCube minder gevoelig is.

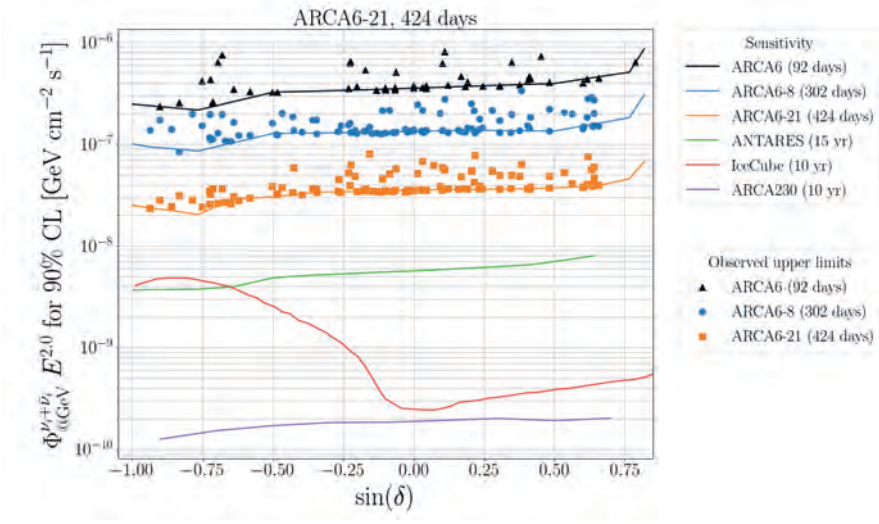

Figure N.8: Vergelijking van de bovengrenzen (stippen) en gevoeligheid (lijnen) van de neutrino stroom Φ als functie van de declinatie δ. De resultaten worden vergeleken met eerder gepresenteerde resultaten van de volledige ANTARES dataset, 10 jaar IceCube gegevens en na 10 jaar met de volledige ARCA detector.

Het potentieel van de volledige detector

De studie uit de vorige sectie gaat gepaard met voorspellingen van de prestaties van de volledige detector. De voltooiing van de bouw van de detector is voorzien voor de komende jaren en dit proefschrift geeft de bijgewerkte gevoeligheid. De gevoeligheid voor neutrino bronnen met 10 jaar aan data wordt getoond in Figuur N.8. Zodra de ARCA detector klaar is, zal deze in staat zijn neutrino stromen te detecteren die buiten het bereik liggen van de huidige neutrino observatoria.

Een ander ijkpunt voor het beoordelen van het potentieel van ARCA is de herontdekking van de diffuse neutrino stroom. Deze isotrope neutrino stroom was het definitieve bewijs van kosmische neutrino's, ontdekt door het IceCube experiment in 2013. De volledige ARCA detector kan deze neutrino stroom binnen een half jaar opnieuw ontdekken, zoals te zien is in Figuur N.9. Door gebruik te maken van de data van de huidige groeiende detector, kan een dergelijke herontdekking eerder plaatsvinden.

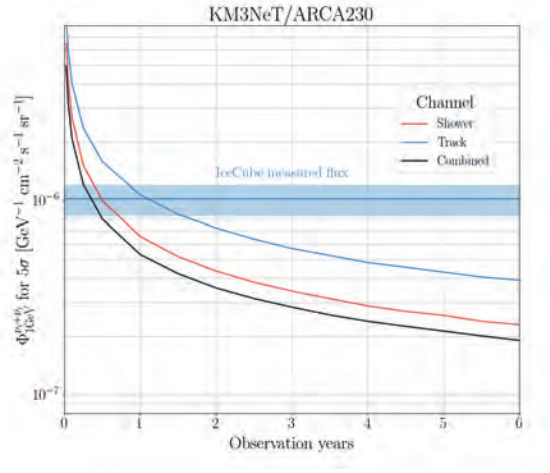

Figure N.9: De neutrino stroom Φ die een ontdekking oplevert als functie van het aantal jaren aan data. De blauwe lijnen vertegenwoordigen de geschatte normalisatie van de neutrino stroom verkregen van IceCube, inclusief hun onzekerheden. Het snijpunt geeft een schatting van de hoeveelheid tijd die nodig is om de neutrino stroom van IceCube te herontdekken.

De smaak van neutrino's bevat een schat aan informatie over de omgeving rond een neutrino bron. De relatieve bijdrage van elke smaak aan de totale stroom geeft verschillende scenario's aan voor het versnellen van kosmische straling. In dit werk is het vermogen van ARCA bestudeerd om de verhouding van neutrino smaak te meten voor verschillende groottes van de toekomstige dataset, zoals weergegeven in Figuur N.10. De prestaties van de ARCA detector bieden veelbelovende mogelijkheden om onderscheid te maken tussen de drie neutrino smaken. Het onderzoek naar de verhouding van neutrino smaak zal worden voortgezet met de huidige ARCA detector en gegevens.

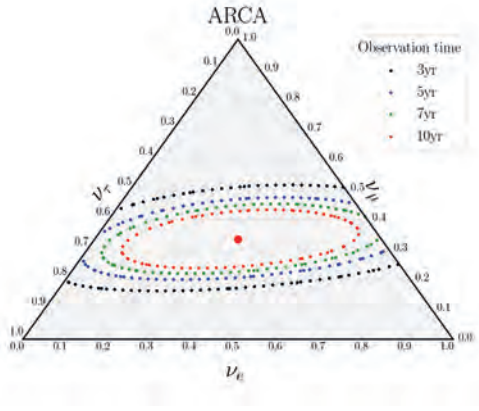

Figure N.10: Driehoek grafiek met de relatieve bijdrage van elektron, muon en tau neutrino's op elke as. De totale som is altijd 1. De lijnen geven het vermogen van ARCA weer om de verhouding van neutrino smaak te meten wanneer de werkelijke verhouding 1/3:1/3:1/3 is (rode stip) met behulp van 3,5,7 en 10 jaar ARCA data. De afnemende grootte van de lijnen staat voor een betere meting van de verhouding waarin neutrino smaken voorkomen.

Acknowledgements

After a summer of wrestling with the question, 'Should I take this PhD position or not?', I walked into Aart's office. The moment I sat down, I confessed my uncertainty. You looked at me, and for a brief second, I saw a flicker of disappointment cross your face. But then you smiled and said, 'Give it a try. If you hate it, just quit.' It's an obvious statement, but it was the little push that I needed. I want to thank you for your forthrightness and excellent supervision. Your door was always open, and when I entered I saw an embodiment of 'The Big Lebowski'. Balancing expertise with a calm 'the dude abides' or a playful 'shut the #&$ up, Donny'.

I was welcomed by my promotor and group leader Paul, whose guidance was invaluable particularly in the final stages of writing this thesis. Your clear insights and direction helped shape the work into its final form. The same gratitude extends to Dorothea, our current group leader. Her wealth of experience was a steady hand during preparations for presentations and conferences. Special thanks to Maarten for your expertise in reconstruction and the many insightful conversations we had. Conferences were always accompanied by dinners and drinks where Ronald was a common accomplice. I enjoyed the beers we shared, though I don't subscribe to your complaints about being 'too old' for it all.

When I circled through our corridors before 9 am, which is rare for a typical physicist working at Nikhef, I always bump into Mieke. Your humor and warm presence made the work environment a lot more pleasant. This is also the case for Ernst-Jan, who took me on a 3 month field trip to TNO in Delft. Playing with lasers in the lab with one thing in mind: an acoustic neutrino telescope. Don't forget to give me a call if you need a physicist. The pack of senior scientists is completed with Daan. We shared an office when you rejoined Nikhef as permanent staff member and my mind was boggled by how you coped with the commute from Groningen, delayed shipments and Italian tenders. Thank you for the hands-on workshop in organisation and project planning.

A new group can be intimidating, but there was Brìan. You were very kind and showed me the ropes from day one. Whether it was presenting at collaboration meetings, attending concerts, and appreciating the swamp water you call Guinness. Even if we overslept on the wrong day (like at my first conference), it was more than worth it. I hand it to you: I am now safely able to walk into an Irish pub somewhere in the world.

Thankfully, I found my like-minded Bèta-gamma student in Rasa. Somebody who beats me in the amount of and time spend on hobbies that have nothing to do with physics. It was a treat to work together on finding neutrinos, but that is obscured by the amount of fun we had while cruising through Italy with an Aperol Spritz in our hand. I cherish our 5 a.m. email exchanges, and your help far beyond just physics.

One of my greatest passions is most fulfilling when shared with others. Thank you, Clara, for going out of your way to indulge in slurping some hand-made pasta, plump and briny oysters or mouth-scorching udon noodles. This was paired with spontaneous beach days, which made my PhD journey much more enjoyable. Just remember, whenever you leave a place: 'oishikatta desu!'

My YouTube career almost restarted thanks to Jordan. I admire your ability to teach and explain things and I thank you for everything that you shared with me. Who knows, maybe one day we'll team up for a YouTube career. Thank you, Bouke, for infusing the workplace with warmth and friendliness. And a special thanks to Jhilik for turning our search for the best food and drinks into a lively competition using Google Maps markers. Then I want to thank Vincent, Victor, Paco, Vikas, Jelmer, Isis, Osama, Rodrigo, Milo, Lodewijk, Karel, Edward and Hans for the friendship that made these years at Nikhef far more enjoyable.

This work was heavily sponsored by two individuals: Alfonso and Valentin. The amount of questions I fired at both of you whether at Nikhef or a place far away is beyond measure. Alfonso, I am still astonished by your knowledge and I want to thank you for the career advice. Valentin, you were an incredible mentor. Though you left too soon, I tried to learn as much as possible from you. Your efficiency and skills are truly something to aspire to.

Although dark matter has yet to be discovered, the group studying this phenomenon was always close. I still can't believe it, Kelly, that you weren't selected for the Lindau Nobel Laureate Meetings. They'll come around eventually. Thank you for all the good times, and I think it's time for us to accept that I might never become a skilled ice skater or pool billiards player like you. I had no idea dark matter came in pairs — enter Maricke. It was a pleasure teaming up for Rasa's defense ceremony and seeing you in action up close. Then there is Auke Pieter. You probably don't know this, but your physics lectures inspired me to study physics from being a doubtful Bèta-gamma student. Your encouragement pushed me to apply for this PhD, and you even convinced me to consider a postdoc: 'We scientists have a lousy, lazy dream job, why not give it a try, right?' I'm still not sure when you're joking, but I'm grateful for your guidance.

Next, I want to mention my friends from the KM3NeT Collaboration. Damien and Giulia, thank you for being outstanding mentors and leaders of the astronomy group. You gave me the freedom to explore, while checking in just enough to keep me on track. A big thank you to Rosa, Carla, Vladimir, Luigi, Katerina, Annarita and Paschal for your support, and to the three Francescos, Anna, Ilaria, Juan, Luc, Godefroy, Agustín, Louis, Vasilis, Walid, Andrey, Dimitris and Rebecca for your support during those late-night bar sessions.

Finally, to my friends and family: thank you for putting up with over 5 years of my endless chatter about neutrinos without showing too much boredom. Explaining the labyrinth of details to Hannah provided a valuable reflection of my own understanding, which often needed improvement. This was balanced by much-needed distractions from a large group of people, including Sien, Arthur and Jesse, helping me clear my head of those relentless neutrinos. The paranymphs, Marius and Sam, may not yet be neutrino experts, but their enthusiasm and creativity in planning the graduation festivities helped carry me through until the end.